

# **Evaluation of the Bajo Blanco sand shoal as a beach nourishment borrow site for eroding beaches at Rincón, Puerto Rico**

By  
Christian Andrés Rojas Vázquez

A thesis submitted in partial fulfillment of the requirements for the degree of  
MASTER IN SCIENCE  
In  
CIVIL ENGINEERING

UNIVERSITY OF PUERTO RICO  
MAYAGÜEZ CAMPUS  
2016

Approved by:

---

Miguel F. Canals Silander, Ph.D.  
President, Graduate Committee

---

Date

---

Raúl E. Zapata López, Ph.D.  
Member, Graduate Committee

---

Date

---

Luis Aponte Bermúdez, Ph.D.  
Member, Graduate Committee

---

Date

---

Sylvia Rodríguez Abudo, Ph.D.  
Member, Graduate Committee

---

Date

---

Kurt A. Grove, Ph.D.  
Representative of Graduate Studies

---

Date

---

Ismael Pagán Trinidad, MSCE.  
Chairperson of the Department

---

Date

## ABSTRACT

The coast of Rincón, Puerto Rico, has been experiencing long-term erosion for the last several decades. The purpose of this research is to evaluate the Bajo Blanco sand shoal, located just offshore of these eroded beaches, as a possible beach nourishment borrow site for these eroding beaches. A sediment compatibility analysis indicates an excavation volume of over 1,000,000  $m^3$  is necessary in order to nourish the beach and the desired 35 meter berm width. To study the response of the wave climate to dredging this amount of sand from Bajo Blanco, two dredging scenarios were simulated using the Coastal Modeling System (CMS) numerical model. Case 1 consists of a single extraction area with a dredge depth of 7 meters beneath the actual seabed, while Case 2 involves two extraction areas, both with a dredge depth of 9 meters. Results indicate that, for both cases, these dredge areas cause a decrease in wave energy shoreward and an increase in wave energy at the edges of the dredge areas. Morphology change simulations suggest that these changes in wave energy in response to dredging could lead, in the long term, to significant sediment erosion and accretion patterns which could impact beach morphology. Further dredging configurations should be evaluated in order to minimize the effects of the dredge area on the nearshore wave climate and sediment transport patterns. One alternative would be to consider a reduction in the berm width, which would significantly reduce the necessary dredge volume. Optimization of the dredging configuration using further numerical simulations is also recommended, with an elongated dredge area seaward of the shoal crest and parallel to the shelf edge being a particularly attractive option.

## RESUMEN

La costa de Rincón, Puerto Rico, ha estado experimentando erosión a largo plazo durante las últimas décadas. El propósito de esta investigación es evaluar el banco de arena de Bajo Blanco, situado cerca de la costa de estas playas erosionadas, como posible área de extracción de sedimento para la regeneración de estas playas. Un análisis de compatibilidad indica que es necesario la excavación de sobre 1,000,000  $m^3$  para el éxito del proyecto de diseño de regeneración de playas y 35 metros de ancho de berma deseados. Para estudiar los efectos sobre el clima de oleaje al extraer esta cantidad de arena de Bajo Blanco, dos escenarios de dragado fueron simulados utilizando el modelo numérico del Sistema de Modelo Costero (CMS). El Caso 1 consiste de una sola área de extracción con una profundidad de dragado de 7 metros por debajo de la superficie actual del fondo del mar, mientras que el Caso 2 envuelve dos áreas de extracción, ambas con una profundidad de dragado de 9 metros. Los resultados indican que, para ambos casos, estas áreas de dragado causan una disminución en la energía de la ola en el lado hacia la costa y un aumento de energía en los bordes del área de dragado. Las simulaciones de cambio morfológico sugieren que estos cambios en energía de la ola en respuesta al dragado pueden llevar, a largo plazo, a un patrón de erosión y acreción significativa de sedimentos que pueden impactar la morfología de la playa. Configuraciones de dragado adicionales se deben evaluar para minimizar los efectos del área de dragado en el clima de olas cerca de la costa y en el patrón del transporte de sedimentos. Una alternativa podría ser considerar una reducción el ancho de berma de diseño, el cual podría significativamente reducir el volumen de dragado necesario. Optimización de las configuraciones de dragado utilizando simulaciones numéricas es también recomendado, siendo una opción particularmente atractiva un área alargada de dragado en el lado hacia el mar de la cresta del banco de arena y paralelo al borde del veril.

© Christian Andrés Rojas Vázquez 2016

...dedicated to my family, especially my lovely mother, Rebecca Vázquez Santiago, who has embraced me with the desire to establish high goals and the determination to achieve them.

## ACKNOWLEDGEMENTS

I would like to thank all those who have carried me emotionally through this hard fought odyssey. My deepest gratitude to my close family, specially my mother and sister for everything they helped me to achieve. Without their love and support over the years none of this would have been possible.

It takes patience and willingness to help others achieve their maximum potential. For that I thank Dr. Miguel Canals-Silander, who I am truly fortunate to have as committee chair through my graduate career in the University of Puerto Rico at Mayagüez. Thank you so much for the knowledge you have passed on and I will always be grateful for having the opportunity to study under you. Without your guidance, patience and help this thesis would not have been possible. In addition, I would like to thank Dr. Luis D. Aponte-Bermúdez for sharing his knowledge and encouraging me to continue my graduate studies in the field of coastal engineering. Also thanks to Dr. Raúl E. Zapata-López for accepting being part of my committee and sharing his expertise and thoughts on what it takes to be an excellent student engineer. He has been a major driving force for many civil engineer students, including myself. His passion and eagerness for them to succeed is something to be valued. Thanks to Dr. Sylvia Rodríguez-Abudo for her motivation and support during these last few years of my Master's degree.

It is important to mention those people who played a role in this study. I express my gratitude to the laboratory technicians, Carlos Ortiz and Luis Rodríguez for their assistance and expertise with field equipment and data acquisition which helped obtain crucial information. Also to field partner graduate student Adail A. Rivera Nieves for sharing his knowledge in hydrography survey and Patricia Chardón for her CMS assistance and previous morphology research study in the coast of Rincón, Puerto Rico and a special thanks to the Coastal Modeling System developing team, especially Lin Lihwa and José E. Sánchez, for their immediate support during the numerical modeling stage. Additional gratitude to my fellow friends and companions from the Marine Technology So-

ciety UPRM Student Section, Ivelisse Rodríguez and many others for their unconditional support and encouragement during this extensive journey.

Last but not least, I would like to extend my gratitude to the Center of Applied Ocean Science and Engineering (CAOSE), the Caribbean Coastal Ocean Observing System (CariCOOS) and the University of Puerto Rico at Mayagüez for their financial support during the completion of this research.

# Contents

<b>1</b>	<b>INTRODUCTION</b>	<b>1</b>
1.1	Coastal processes . . . . .	1
1.2	Study site . . . . .	4
<b>2</b>	<b>OBJECTIVES</b>	<b>10</b>
<b>3</b>	<b>BATHYMETRY PROPERTIES AND SEDIMENT COMPATIBILITY</b>	<b>11</b>
3.1	High-resolution bathymetric survey of the Bajo Blanco sand shoal . . . . .	11
3.1.1	Field measurements . . . . .	13
3.1.2	System error estimation . . . . .	13
3.1.3	Data processing . . . . .	18
3.1.4	Bathymetric survey results . . . . .	21
3.2	Grain size compatibility analysis . . . . .	23
3.2.1	Sieve analysis . . . . .	27
3.2.2	Sieve analysis results . . . . .	30
3.2.3	Compatibility analysis results . . . . .	34
3.3	Concluding remarks . . . . .	39
<b>4</b>	<b>VALIDATION OF HYDRODYNAMIC NUMERICAL MODEL ON NEARSHORE</b>	
	<b>WAVE CLIMATE</b>	<b>41</b>
4.1	Introduction . . . . .	41
4.2	The Coastal Modeling System (CMS) . . . . .	41
4.2.1	CMS-Wave . . . . .	42

4.2.2	CMS-Flow model . . . . .	51
4.3	CMS model set-up . . . . .	52
4.3.1	CMS-Flow set-up . . . . .	53
4.4	CMS validation results . . . . .	59
4.5	Concluding remarks . . . . .	61
<b>5</b>	<b>EFFECT OF SAND MINING ON NEARSHORE WAVE CLIMATE</b>	<b>62</b>
5.1	Case studies . . . . .	63
5.2	Grid development . . . . .	65
5.3	Model results . . . . .	66
5.3.1	Effects on wave climate . . . . .	67
5.3.2	Wave energy flux response . . . . .	72
5.3.3	Current response . . . . .	83
5.3.4	Morphology response . . . . .	89
5.4	Particle Tracking Model (PTM) . . . . .	95
5.4.1	Model overview . . . . .	95
5.4.2	Model set-up . . . . .	96
5.4.3	Model results . . . . .	99
5.5	Concluding remarks . . . . .	104
<b>6</b>	<b>CONCLUSION AND RECOMMENDATIONS</b>	<b>106</b>
	<b>REFERENCES</b>	<b>109</b>
	<b>APPENDICES</b>	<b>114</b>
	<b>Appendix A Sieve results</b>	<b>115</b>

## List of Figures

1.1	Schematic cross-section of a beach system . . . . .	2
1.2	Diagram illustrating the movement of sand and pebbles along the coast, action known as longshore drift. . . . .	2
1.3	Diagram illustrating the technique of beach nourishment . . . . .	4
1.4	Location of relevant areas along the coast of Rincón, including the Tres Palmas Marine Reserve, the Bajo Blanco sand shoal and the extension of coast to be nourished approximately 5 km from Rincón Marina to Córcega beach . . . . .	5
1.5	Wave rose obtained from the CariCOOS Waverider buoy . . . . .	7
1.6	Field conditions during moderate wave event . . . . .	7
1.7	Field conditions during extreme wave event . . . . .	8
3.1	Personal watercraft instrumentation. . . . .	12
3.2	Track-lines for the jetski-based bathymetric survey along the Bajo Blanco sand shoal	14
3.3	Horizontal uncertainty at 95% confidence interval for GPS system offset and roll and pitch angles between 4 and 10 degrees. . . . .	16
3.4	Vertical uncertainty at 95% confidence interval for echosounder system offset, sound speed and roll and pitch angles between 4 and 10 degrees. . . . .	17

3.5	Survey route with the processed track points gathered at the Bajo Blanco sand shoal using the ArcGIS TIN to Raster tool. . . . .	19
3.6	Survey bathymetric contour map with interpolated values using the ArcGIS TIN to Raster tool. Letters A, B and C represent control points for location purposes. . . .	20
3.7	The Bajo Blanco sand shoal bathymetry (3D view). Letters A, B and C represent control points for location purposes. . . . .	21
3.8	Comparison between the 2014 high-resolution bathymetric survey data and the 2007 NGDC DEM bathymetry . . . . .	22
3.9	Observation profiles at Bajo Blanco to compare bathymetry of 2014 with NGDC DEM 2007. . . . .	24
3.10	Transect near the Rincón Marina comparing the NGDC DEM 2007 data (red) and the jetski-based bathymetric survey results of 2014 (blue). The x-coordinate system is positive in the offshore direction. . . . .	24
3.11	Transect located at Rincón public beach comparing the NGDC DEM 2007 data (red) and the jetski-based bathymetric survey results of 2014 (blue). The x-coordinate system is positive in the offshore direction. . . . .	25
3.12	Transect near Los Ramos ravine comparing the NGDC DEM 2007 data (red) and the jetski-based bathymetric survey results of 2014 (blue). The x-coordinate system is positive in the offshore direction. . . . .	25
3.13	Alternative computation of Dean’s overfill factor as a single curve using dimensionless parameters $M'_b$ and $M'_n$ . . . . .	26
3.14	Sieve analysis procedure for fine sediments . . . . .	27

3.15	Location of the 8 samples collected along the coast of Rincón in segments of approximately 400 to 600 meters. . . . .	28
3.16	Location of the 18 samples collected at the Bajo Blanco with an average spacing of 300 meters between samples. . . . .	29
3.17	Percent passing and sieve size logarithmic plot for native sand samples (blue) and borrow site sand samples (red) . . . . .	30
3.18	Mean grain size results for Bajo Blanco and beaches from Rincón Marina to Córcega beach. . . . .	32
3.19	Mean grain size contour color map for Bajo Blanco and beaches from Rincón Marina to Córcega beach. . . . .	33
3.20	Image presenting the location of the core samples at Bajo Blanco . . . . .	34
3.21	Schematic showing existing bathymetry contours (magenta) along with the depth of closure (red) and the calculated beach profiles elevation (yellow) (from Salas, 2014). . . . .	35
3.22	Observation profile showing the existing beach profile (cyan) and the calculated beach profile (blue) (from Salas, 2014). . . . .	36
3.23	Dean’s overfill factor for the mean grain size of Bajo Blanco and the mean grain size from eroded beaches in Rincón. . . . .	38
4.1	CMS-Wave and CMS-Flow coupled numerical model . . . . .	42
4.2	Non-uniform grid for the CMS-Wave model . . . . .	47

4.3	Location of the pressure sensors and current profilers installed at TPMR to measure wave and current data from January 11 <sup>th</sup> , 2013 to February 25 <sup>th</sup> , 2013. . . . .	48
4.4	Time-series comparison between the observed (black) significant wave height at the AWAC and the CMS-Wave results using the TFS (blue), WFS (red) and the CPM (green) spectral descriptions. . . . .	49
4.5	Time-series comparison between the observed (black) significant wave height at pressure sensor II (PS2) and the CMS-Wave results using the TFS (blue), WFS (red) and the CPM (green) spectral descriptions. . . . .	49
4.6	Time-series comparison between the observed (black) significant wave height at pressure sensor I (PS1) wave height and the CMS-Wave results using the TFS (blue), WFS (red) and the CPM (green) spectral descriptions. . . . .	50
4.7	Linear correlation results for the time series comparison between the observed measurements and predicted CMS-Wave results . . . . .	51
4.8	CMS-Flow numerical model parent grid for the current study . . . . .	53
4.9	Telescoping grid for the CMS-Flow model . . . . .	54
4.10	Merged bathymetry used by the CMS numerical model composed of the 2007 NGDC DEM bathymetry and the jetski-based high-resolution bathymetric survey from May, 23 <sup>th</sup> 2014 (modified from Chardón, 2013). . . . .	55
4.11	CMS-Flow telescoping grid ranging from 32 m to 4 m spatial resolution . . . . .	56
4.12	Comparison results between the simulated (blue) wave height and wave period vs observed data at the AWAC sensor (black) . . . . .	60

4.13	Comparison between the numerical simulation results (blue) and field observations (black) of the north-south velocity component ( $V_y$ ) and water surface elevation at the Sentinel ADCP and the Mayagüez mareograph, respectively. . . . .	60
4.14	Illustration of the linear correlation results for the north-south current magnitude and the water surface elevation extracted from the coupled CMS numerical model at the Sentinel ADCP and Mayagüez mareograph, respectively. . . . .	61
5.1	The single dredge area (S1) scenario has an extraction area of 144,000 $m^2$ with a dredge depth of 7 m . . . . .	64
5.2	Multiple dredge areas scenario, M1 and M2, with a total area of 121,000 $m^2$ and dredge depth of 9 m each . . . . .	64
5.3	Pre-dredging CMS numerical model results for significant wave height during the peak hour of January 2 <sup>nd</sup> , 2013. The instantaneous significant wave height (colored contours) is presented for the entire model domain, and vectors represent mean wave direction. . . . .	68
5.4	Pre-dredging CMS numerical model results for wave energy flux during the peak hour of January 2 <sup>nd</sup> , 2013. . . . .	69
5.5	Pre-dredging CMS numerical model results for average wave energy flux during the two months simulation period (January - February 2013). . . . .	70
5.6	Pre-dredging CMS numerical model results for cumulative wave energy flux during the two months simulation period (January - February 2013) . . . . .	71
5.7	Post-dredging CMS numerical model average wave energy flux results for Case 1 during the two month simulation period (January - February 2013) . . . . .	73

5.8	Post-dredging CMS numerical model average wave energy flux results for Case 2 during the two month simulation period (January - February 2013) . . . . .	74
5.9	Post-dredging CMS numerical model cumulative wave energy flux results for Case 1 during the two month simulation period (January - February 2013) . . . . .	75
5.10	Post-dredging CMS numerical model cumulative wave energy flux results for Case 2 during the two month simulation period (January - February 2013) . . . . .	76
5.11	Wave energy flux response (percentage wise) for the peak hour of January 2 <sup>nd</sup> , 2013 for Case 1 . . . . .	77
5.12	Wave energy flux response (percentage wise) for the peak hour of January 2 <sup>nd</sup> , 2013 for Case 2 . . . . .	78
5.13	Wave height response (percentage wise) for the peak hour of January 2 <sup>nd</sup> , 2013 for Case 1 . . . . .	79
5.14	Wave height response (percentage wise) for the peak hour of January 2 <sup>nd</sup> , 2013 for Case 2 . . . . .	80
5.15	Map depicting the alongshore observation profiles for the 2 m depth contour (a and b) and the 5 m depth contour (c and d). . . . .	81
5.16	Wave height response observation profile for Case 1 (blue) and Case 2 (cyan) dredging scenarios during the peak hour of January 2 <sup>nd</sup> , 2013. Transects (a)-(b) and (c)-(d) are the observation profiles along the 2 m and 5 m depth contour, respectively. . . . .	82

5.17 Cumulative wave energy flux response observation profile for single (blue) and multiple (cyan) dredging scenarios during the peak hour of January 2 <sup>nd</sup> , 2013. Transects (a)-(b) and (c)-(d) are the observation profiles along the 2 m and 5 m depth contour, respectively. . . . .	82
5.18 Pre-dredging CMS numerical model current magnitude and direction results for existing conditions on January 2 <sup>nd</sup> , 2013 at 4 AM. . . . .	84
5.19 Post-dredging CMS numerical model current magnitude and direction results for Case 1 on January 2 <sup>nd</sup> , 2013 at 4 AM. . . . .	85
5.20 Post-dredging CMS numerical model current magnitude and direction results for Case 2 on January 2 <sup>nd</sup> , 2013 at 4 AM. . . . .	86
5.21 Post-dredging CMS numerical model current magnitude response for Case 1 during an instant of the simulation on January 2 <sup>nd</sup> , 2013 at 4 AM. . . . .	87
5.22 Post-dredging CMS numerical model current magnitude response for Case 2 during an instant of the simulation on January 2 <sup>nd</sup> , 2013 at 4 AM. . . . .	88
5.23 Simulated cumulative morphological change at Bajo Blanco for existing bathymetry during the months of January and February 2013 . . . . .	90
5.24 Simulated cumulative morphological change at Bajo Blanco for Case 1 during the months of January and February 2013 . . . . .	91
5.25 Simulated cumulative morphological change at Bajo Blanco for Case 2 during the months of January and February 2013 . . . . .	92
5.26 Post-dredging CMS numerical model morphology change response for Case 1 during the months of January and February 2013 . . . . .	93

5.27 Post-dredging CMS numerical model morphology change response for Case 2 for the two month simulation period (January - February 2013) . . . . .	94
5.28 Plots of significant wave height and water surface elevation at the location of the CariCOOS Rincón buoy during the month of January 2013 . . . . .	98
5.29 PTM line source location with respect to the Tres Palmas Marine Reserve. . . . .	99
5.30 Release period during ebb tide and moderate wave forcing . . . . .	100
5.31 Release period during flood tide and low wave forcing . . . . .	101
5.32 Release period during ebb tide and low wave forcing . . . . .	102
5.33 Release period during flood tide and moderate wave forcing . . . . .	103

## List of Tables

4.1	Primary tidal harmonic constituents for Mayagüez, Puerto Rico with their respective amplitude, phase and phase speed (NDBC, 2016). . . . .	58
4.2	Sediment transport model set-up parameters for the CMS Flow numerical model. .	59
5.1	Geometric characteristics of potential borrow site areas. . . . .	65
5.2	PTM model set-up and sediment characteristics used for the simulation period. . . .	97
5.3	Release periods for each of the dredging scenarios, with their corresponding tide and wave forcing characteristics. . . . .	98
A.1	Latitude and longitude for each of the samples collected at the coast of Rincón. . .	116
A.2	Latitude and longitude for each of the samples collected at the Bajo Blanco sand shoal. . . . .	116
A.3	Sieve analysis results for the 8 samples collected at the coast of Rincón, including standard deviation and mean grain size in millimeters and phi units. . . . .	117
A.4	Sieve analysis results for the first 9 samples collected at the Bajo Blanco shoal, including standard deviation and mean grain size in millimeters and phi units. . . .	117
A.5	Sieve analysis results for the last 9 samples collected at the Bajo Blanco shoal, including standard deviation and mean grain size in millimeters and phi units. . . .	117

# Chapter 1

## INTRODUCTION

### 1.1 Coastal processes

Beaches are responsible for the protection of coastal lands against extreme wave events and serve as a recreational resource for tourists and local residents. It is very important to understand the hydrodynamics and coastal processes at each site to be able to provide engineering solutions that protect the environment and infrastructure near vulnerable areas. Figure 1.1 shows a schematic of the beach system, which usually extends from the dunes to the inner edge of the continental shelf, where the swash zone and surf zone are the most dynamic regions (Stanica and Ungureanu, 2010).

The littoral zone is where most of the main coastal processes occur as a result of the action of tides, wind waves, currents, and man-made structures. As wind waves approach the shore, their speed decreases while they squeeze together increasing wave height in a process called shoaling. As water depth decreases, the bottom of the wave slows down to a point where the top of the wave spills forward creating a breaking wave. Waves are primarily responsible for the onshore, offshore, and alongshore movement of sand. Soon after a wave breaks, there is a sudden dissipation of energy that causes great turbulence and stirs up bottom sediments. Figure 1.2 shows how the wind and current patterns influence the movement of sand along the coast contributing to a constantly changing coastline (Jack, 2010). Beach evolution is controlled by a balance in the sediment transport (Inman, 1965). When the supplied sand is greater than the required amount for equilibrium, the coast grows seawards in a process called accretion; while insufficient sand supply provokes the coast to retreat by erosion.

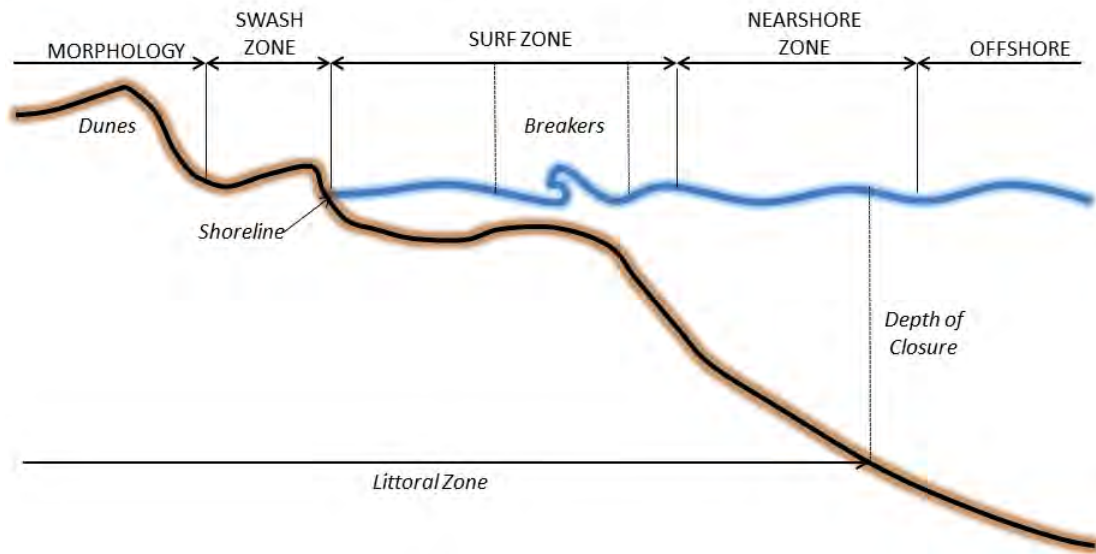


**Figure 1.1:** Schematic cross-section of a beach system. The littoral zone is where most of the coastal processes take place, with the surf zone being the most dynamic region.

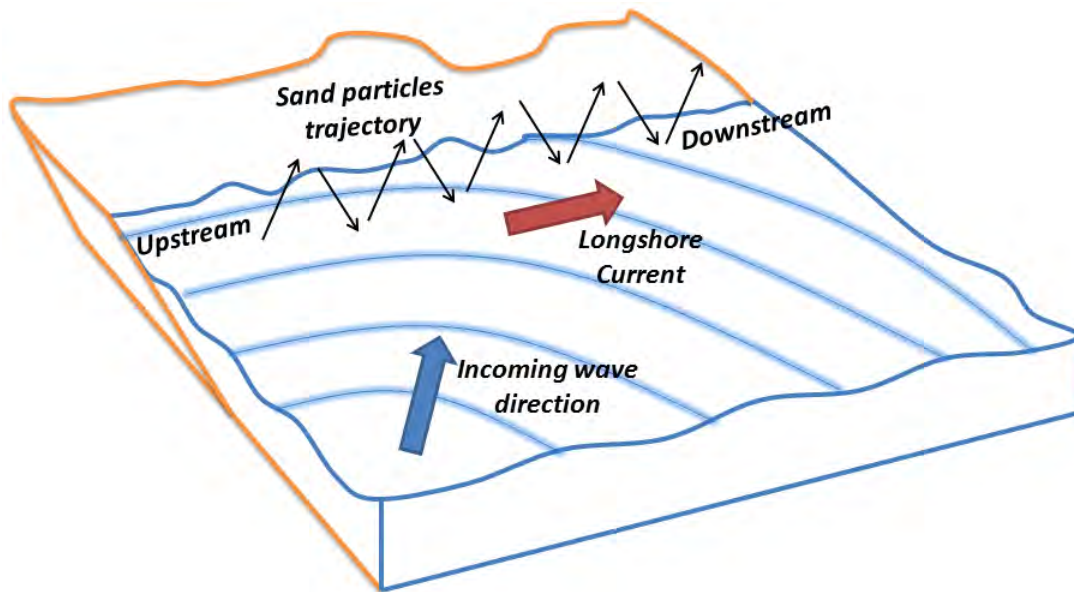


**Figure 1.2:** Diagram illustrating the movement of sand and pebbles along the coast, action known as longshore drift.

There are several ways to protect the coast from coastal erosion and extreme wave events. If designed correctly, hard structures such as breakwaters, groins, and jetties can dissipate wave energy before it reaches the shore, while retaining sand and nourishing the beach in the process. In contrast, these structures can sometimes change the shape of beaches by blocking alongshore sediment transport, which restricts the natural capacity of the beach system to restore itself after a storm event (Conathan et al., 2014).

There are non-structural strategies which can be used to attempt to mitigate beach erosion. A soft measure is the addition of compatible sand to replace the sediment that has been eroded away by waves and currents. This technique is known as beach nourishment (Dean and Dalrymple, 2004), and usually consists of dredging beach grade sand from an offshore or inland source to replenish a beach and combat erosion by increasing beach width. As shown in Figure 1.3, this method widens the beach and protects the coastal infrastructure as long as the added sand remains in the system. In comparison to hard structures, this method does not leave hazards on the beach, like eroded debris from seawalls and groins, and allows the beach to reach an equilibrium through erosion and accretion, although it's success depends strongly on the compatibility of the added sand (Barber, 2015). If sand from borrow site is incompatible, it could erode faster than native sand, and could result in the failure of the project (Dean and Dalrymple, 2004). If compatible sand is readily available, however, beach nourishment is by far the preferred strategy for shore protection today (Barber, 2015).

The present study evaluates the Bajo Blanco sand shoal as a potential beach nourishment borrow site. Located off the coast of Rincón, Puerto Rico, it provides a local source for beaches affected by extreme erosion over the past few decades. This erosion is presumably a consequence of high-energy wave events such as hurricanes, storms, and winter swells combined with shoreline hardening and a shortage of sediment supply (Thieler et al., 2007).

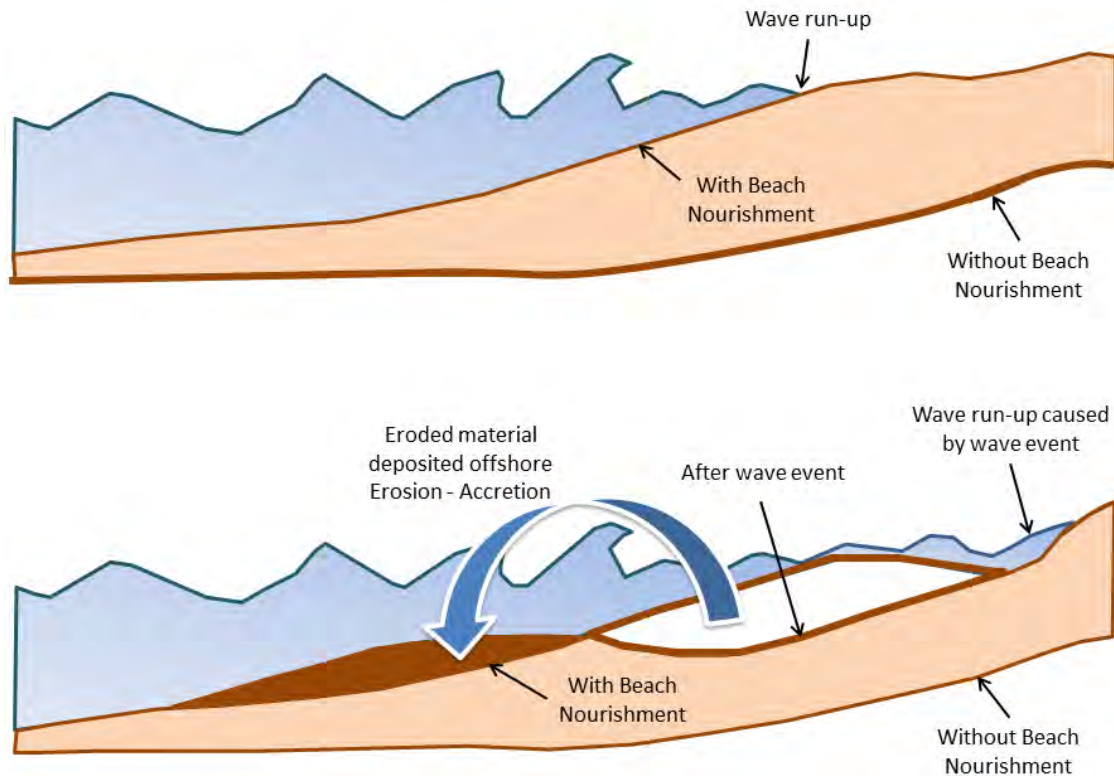


**Figure 1.3:** The technique of beach nourishment requires the addition of sediments (sand) of suitable quality to protect the coast. During the process, the added sediment from the shore erodes and gets deposit offshore helping the system reach equilibrium over time.

## 1.2 Study site

The town of Rincón is located on the northwest corner of Puerto Rico, at a point where the Atlantic Ocean encounters the Caribbean Sea. The coastline is approximately 12 km in length and has a marine ecosystem composed of coral reefs, sandy shores, and artificial structures. The study site (Figure 1.4) shows Rincón, Puerto Rico, nourishment site, and the extent of the Bajo Blanco sand shoal, among other features. A number of useful instrument stations are located nearby such as a Waverider Directional Buoy off the coast of Rincón, Mayagüez and Aguadilla mareographs and Rincón anemometer. These are maintained by the Caribbean Coastal Ocean Observing System (CariCOOS) and the Puerto Rico Seismic Network (PRSN) helping provide accurate boundary conditions for the numerical simulations and field measurements for validation purposes.

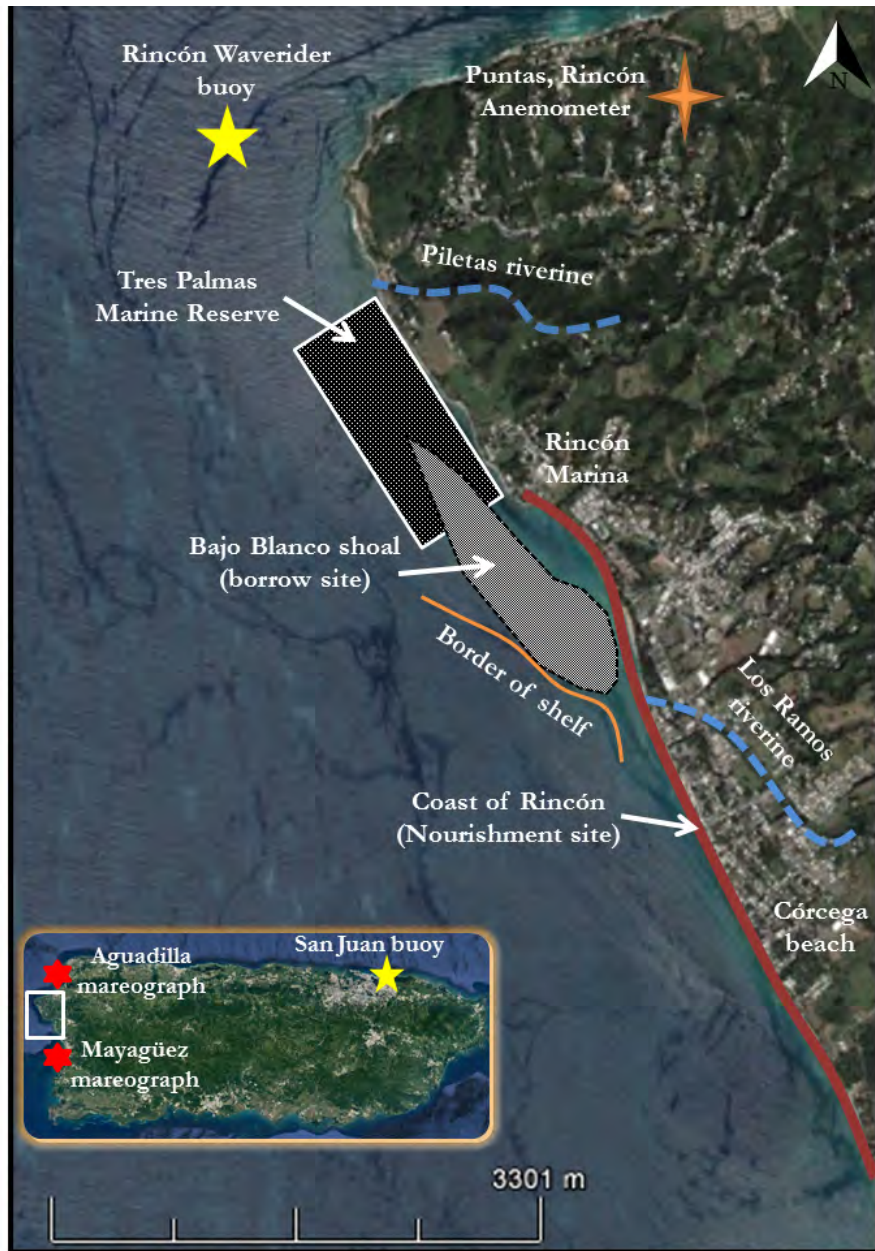


**Figure 1.4:** Location of relevant areas along the coast of Rincón, including the Tres Palmas Marine Reserve, the Bajo Blanco sand shoal and the extension of coast to be nourished approximately 5 km from Rincón Marina to Córcega beach. On the lower left corner, a map of Puerto Rico showing the location of the San Juan directional buoy (yellow star) and the Aguililla (top) and Mayagüez (bottom) mareographs (red stars) used to estimate environmental conditions prior field activity.

The Tres Palmas Marine Reserve (TPMR) is located just north of the Bajo Blanco sand shoal. The TPMR protects multiple coral species including what is considered to be one of the healthiest Elkhorn coral (*Acropora palmata*) populations in the Caribbean (NOAA, 2009). North-facing beaches in Rincón are characterized by strong waves during the months of October to April, while southwest-facing beaches south of the marina are much calmer throughout the year. During 2013, the CariCOOS Waverider Buoy registered a wave climate mostly dominated by north-northeast swells (Figure 1.5). According to the statistical wave rose provided by the Coastal Data Information Program (CDIP, 2016), during 2013 nearly 90% of the waves came from the north-northeast, about 8% from the northwest and the rest from the southwest direction. Coastal waves are wind-generated surface gravity waves, short period waves from local seas and long period swells (Chardón, 2013). Local wind waves have periods between 1-8 seconds. Long-period swells are caused by distant weather systems and can reach periods between 8-22 seconds. Even though the wave climate varies seasonally, a significant mix of wave direction and periods dominate the majority of the time. Local waves are usually from the northeast and dominate, less frequent, between significant wave events.

Beaches in Rincón have been subjected to extreme erosion over the last few decades. Figures 1.6 and 1.7 display conditions before and after a moderate wave event on March 2014 and tropical storm Isaac during the 2012 hurricane season, respectively. Using aerial photography, Thieler et al. (2007) studied historical shoreline changes along the coast of Rincón, Puerto Rico, between Punta Higuera and Punta Cadena, from 1936 to 2006. The coastal reach between the Rincón Public Beach to 500 m south of the mouth of Los Ramos ravine was found to have an average long-term erosion rate of  $1.1 \pm 0.3$  m/yr. It is still not clear what exactly is causing this long term erosion in Rincón. Chardón (2013) studied the impact of extreme wave events on the hydrodynamics and morphologic change between the Tres Palmas Marine Reserve (TPMR) and Villa Cofresí Hotel. Their results suggest that southwesterly wave events, caused by tropical storms and hurricanes passing south of Puerto Rico, cause severe coastal erosion, while long-period wave events from

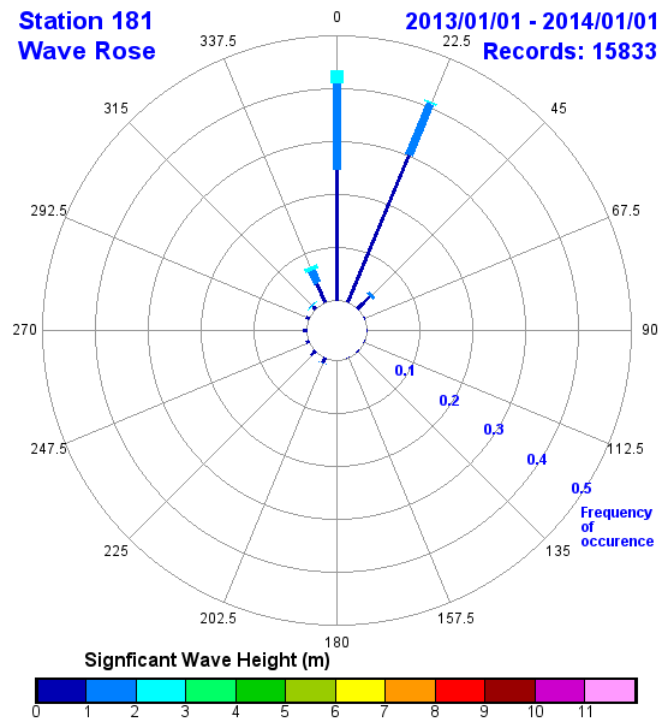


**Figure 1.5:** Wave rose obtained from the CariCOOS Waverider buoy located one mile offshore from Rincón’s lighthouse (CDIP, 2016). The wave climate statistical results corresponds to the year of 2013.



**Figure 1.6:** (a) Conditions at Rincón’s public beach before and after March 28<sup>th</sup> 2014 wave event. (b) During this wave conditions, the San Juan CariCOOS buoy registered waves of up to 4 meters in significant wave height with period of over 15 seconds. (c) Marine ecosystem at Tres Palmas Marine Reserve. (d) Conditions at Hotel Confresí before and after March 2014 moderate wave event.



**Figure 1.7:** Extreme erosion at the coast of Rincón caused by tropical storm Isaac. The photos identified by the same letter represent the same location (from Chardón, 2013).

the northeast did not cause severe erosion and, in some cases, actually helped beaches to recover from previous erosion events. According to the numerical solutions of Chardón (2013), most of the sediment transport occurred in the Bajo Blanco sand shoal, which confirms what was suggested by Thieler et al. (2007) that Bajo Blanco is probably a major factor in the sediment budget of Rincón.

The Bajo Blanco is just one of many sand deposits found around Puerto Rico. Studies by the USGS in Puerto Rico suggest that these types of deposits could serve as new resources of sand and gravel. These deposits would allow beaches to be nourished in order to mitigate coastal erosion (Rodríguez, 2016). USGS scientists have identified several offshore sand and gravel deposits around Puerto Rico including Isabela, Cabo Rojo and Vieques. According to Rafael W. Rodríguez, USGS Caribbean Water Science Center Office Director, sand deposits off Isabela may not be economically viable for extraction due to deep water at the deposit locations. On the other hand, the removal of fine-grained sediments along the Cabo Rojo deposit could endanger nearby coral ecosystems and create a negative impact to the surrounding environment. The largest deposit is “Escollo de Arenas” located northwest of the coast of Vieques. Evidence suggests that sand mining here would not affect nearby beaches since the sand shoal is naturally nourished by coastal

processes. However, the distance between Rincón's eroded beaches and the "Escollo de Arenas" is approximately 300 km, which would lead to very high costs of transportation.

Another important factor to consider when analyzing possible sand borrow sites are the potential effects of sand mining on nearshore processes. Beach nourishment usually requires several hundred thousand and up to several million cubic meters of sand, which can lead to very significant modifications to the seabed. The Minerals Management Service (MMS), a bureau within the U.S. Department of the Interior, examined the shoreline response for dredging areas off southern New Jersey, southeastern Virginia, North Carolina, and Cape Canaveral, Florida (Kelley et al., 2001). The study consisted of evaluating the potential negative impact to the local wave and sediment transport regime as a consequence of dredging a significant quantity of sand from those areas. Field measurements and numerical simulations (ST-WAVE and CMS-Flow) were performed in order to estimate the effect of such actions. The present study will take a similar approach and will evaluate the impact of dredging the nearby the Bajo Blanco sand shoal, located just offshore of these eroded beaches, to evaluate the potential effects on the nearshore hydrodynamics and determine whether this site could be used as a possible beach nourishment borrow site for the eroding beaches in Rincón.

## **Chapter 2**

### **OBJECTIVES**

The present study seeks to evaluate whether the nearby the Bajo Blanco sand shoal, located just offshore of some of the most eroded beaches in Rincón, could be used as a possible beach nourishment borrow site. The specific objectives are as follows:

- Determine whether the sand found at the Bajo Blanco sand shoal is compatible to serve as beach fill material for Rincón beaches.
- Use a jetski-based bathymetric surveying system to collect bathymetry data of the Bajo Blanco sand shoal.
- Implement and validate a coupled wave, current, and sediment transport model, the United States Army Corps of Engineers (USACE) Coastal Modeling System (CMS), in an effort to understand the response of the wave climate, hydrodynamics and nearshore morphology to the potential use of the Bajo Blanco sand shoal as a beach nourishment borrow site.

The completion of these objectives will shed light on the feasibility of using Bajo Blanco as a sand borrow site for a potential beach nourishment project in Rincón.

## Chapter 3

# BATHYMETRY PROPERTIES AND SEDIMENT COMPATIBILITY

This chapter includes a detailed description of the bathymetry of Bajo Blanco and discusses the grain size compatibility between the sand at Bajo Blanco and Rincón's eroded beaches. The bathymetric surveys were performed with assistance from Marine Science graduate student Adail Rivera as well as technical support from personnel from the UPRM Center of Applied Ocean Science and Engineering (CAOSE).

### 3.1 High-resolution bathymetric survey of the Bajo Blanco sand shoal

A modified version of the jetski-based bathymetric surveying system, developed by Chardón (2013) was used to obtain high-resolution depth and position measurements across Bajo Blanco. Figure 3.1 shows the modified version with all the instrumentation used for the data acquisition.

The jetski is a 2011 four-stroke Yamaha VXR WaveRunner with a waterproof 12-volt battery charged by an Epcom 50 Watt solar panel. The survey equipment consists of a Lowrance HDS-7 Gen2 Touchscreen with a StructureScan HD transducer (frequency of 455 kHz and 800 kHz) able to deliver greater resolution and wider range with three dedicated transducer signals (Lowrance, 2012). Lowrance visual features are controlled by an internal Global Positioning System (GPS) updating position at a frequency of 1 Hz. The transducer is installed 0.35 m below the waterline providing depth measurements from sidescan, downscan and the primary transducer at 1 Hz. An additional 200 KHz Sonarmite BT echosounder system is installed alongside the Lowrance trans-



**Figure 3.1:** Personal watercraft instrumentation: (1) Lowrance HDS-7 Gen2 Touchscreen; (2) StructureScan HD Sidescan; (3) Sonarmite BT echosounder system; (4) GPS support pole; (5) solar panel; (6) watertight laptop case; (7) YUAN10 GPS receiver (modified from Chardón, 2013).

ducer, recording depth measurements at 2 Hz with a 7 degree beam sound pulse. The main GPS antenna is mounted at the top of a pole located 1.95 m right above the transducer. The GPS receiver is a YUAN10 from One Talent Global Navigation Satellite System (GNSS) with a rover and base receiver that records its position at 20 Hz and 1 Hz, respectively. The data from the GPS receiver and Sonarmite BT echosounder are streamed in real time to a laptop computer protected with a custom made waterproof case which allows visual access to the operator. The suggested acquisition software to use for the YUAN10 GPS is RTKLIB (Bavaro, 2012). RTKLIB is an open source GNSS program package for precise positioning data processing. For a detailed description of the process please refer to the RTKLIB user manual (Takasu, 2015).

### **3.1.1 Field measurements**

To obtain accurate bathymetric data, suitable field conditions are required to minimize field errors. The speed of the vessel must be 4 knots or less to reduce pitch and roll errors. Excessive wind speed may contribute to the formation of waves which could lead to undesirable vessel motion. Low wind speed, below 8 knots, and small amplitude waves with period not exceeding 5 seconds were the desirable environmental settings to ensure better handling of the vessel and reliable measurements.

The hydrographic survey was performed over Bajo Blanco on May 23<sup>rd</sup> 2014, before the active storm season, between the hours of 6:00 am and 10:00 am. Figure 3.2 displays the planned route, which consisted of 87 survey profiles for a total of 38 km of data. Nearby meteorological stations and two National Oceanic and Atmospheric Administration (NOAA) tide gauges (Aguadilla and Mayagüez) provided sea level conditions during the survey period.

### **3.1.2 System error estimation**

One of the primary concerns with field measurement techniques is the uncertainty of the obtained values. The International Hydrographic Organization (IHO) has a series of standards for

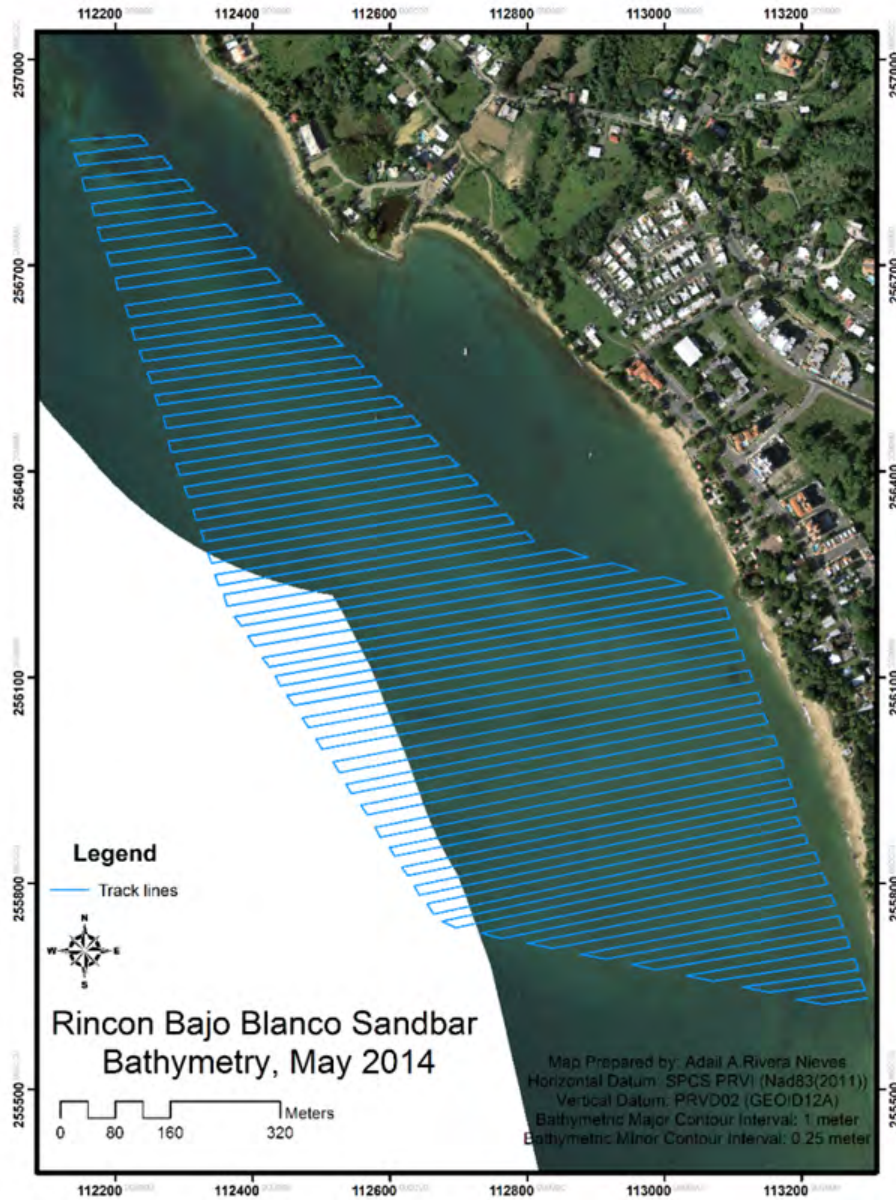


**Figure 3.2:** Track-lines (blue) for the jetski-based bathymetric survey along Bajo Blanco in Rincón, Puerto Rico. Horizontal coordinates are in State Plane Coordinate System (SPCS) - NAD83.

the execution of hydrographic surveys to help collect quality measurements and improve the safety of navigation and protection of the marine environment (IHO, 2009). For the current study, the horizontal positioning is referenced to the Puerto Rico and Virgin Islands (PRVI) State Plane Coordinate System (SPCS), North American Datum 1983 (NAD, 1983), using the MAYZ GPS station of the PR Seismic Network. Vertical positioning is referenced to the Puerto Rico Vertical Datum 2002 (PRVD02) using the GEOID12A of the National Geodetic Survey (NGS, 2016) model. The IHO standards were used to adjust measurements based on the uncertainties related to GPS and echosounder system offsets as well as roll and pitch errors due to vessel motion. Vertical measurements were also modified taking into account the effect of sound speed, which is a function of salinity and temperature.

### ***Horizontal quality control***

The horizontal adjustment includes the systematic uncertainty of the YUAN10 GPS system of  $\pm 0.50$  m. Real Time Kinematics (RTK) reduces position error to just  $\pm 0.015$  m if the right GPS connection requirements are met. Since the survey was made during calm sea state conditions, pitch and roll motion errors are estimated to be less than 10 degrees during the survey. According to MacMahan (2001), an average pitch and roll angle in shallow waters is approximately 5 degrees. The horizontal pitch and roll effect ( $H_{pr}$ ) is estimated using the equation  $d \tan(\phi_{pr} - 0.5\theta_b)$ . Pitch and roll errors are a function of depth,  $d$ , roll and pitch angles,  $\phi_{pr}$ , and the beam width of the emitted echosounder pulse,  $\theta_b$ . Pitch and roll angles equal to or less than half of the echosounder's beam width does not cause any effect on the horizontal positioning due to the motion of the vessel (IHO, 2015). The sum of horizontal uncertainties is shown in Figure 3.3 for pitch and roll angles of 4, 6, 8 and 10. The maximum horizontal uncertainty to achieve an IHO 1B standard is 5 m + 5% of depth. The red line represents the minimum horizontal accuracy requirements for order 1B. Values below the red line are acceptable measurements according to the IHO taking into account the vessel's movements and GPS uncertainty along the survey.

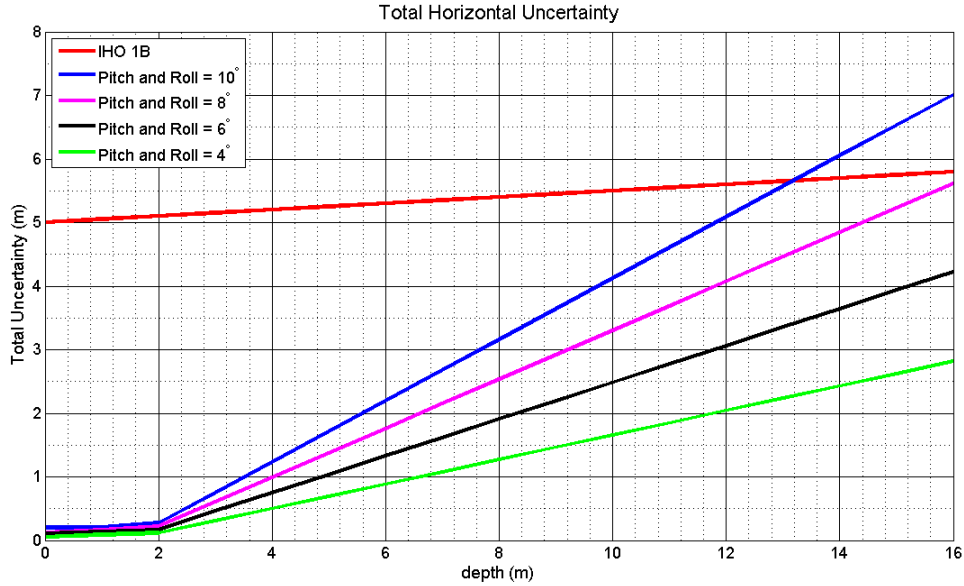


**Figure 3.3:** Horizontal uncertainty at 95% confidence interval for GPS system offset and roll and pitch angles between 4 and 10 degrees.

From Figure 3.3, it can be observed that for calm conditions, having pitch and roll angles equal or less than 8 degrees, the system complies with the IHO 1B standard for depths up to 13 meters.

### ***Vertical quality control***

The vertical adjustment accounts for the SonarmiteBT echosounder system uncertainty, the vessel's motion and the effect of the change in salinity and temperature. The echosounder uncertainty is 0.01 m + 0.1% (SeaFloorSystems, 2015). The vertical pitch and roll effect ( $V_{pr}$ ) is estimated using equation 3.1. As previously mentioned, pitch and roll angles less than 4 degrees will have little to no effect on vertical measurements.

$$V_{pr} = \frac{d}{\cos(\phi_{pr} - 0.5\theta_b)} - d. \quad (3.1)$$

The speed of sound is not always constant and varies by a small amount as a function of water depth. Sound travels at approximately 1500 m/s in the ocean. Parameters such as salinity ( $S_a$ ),

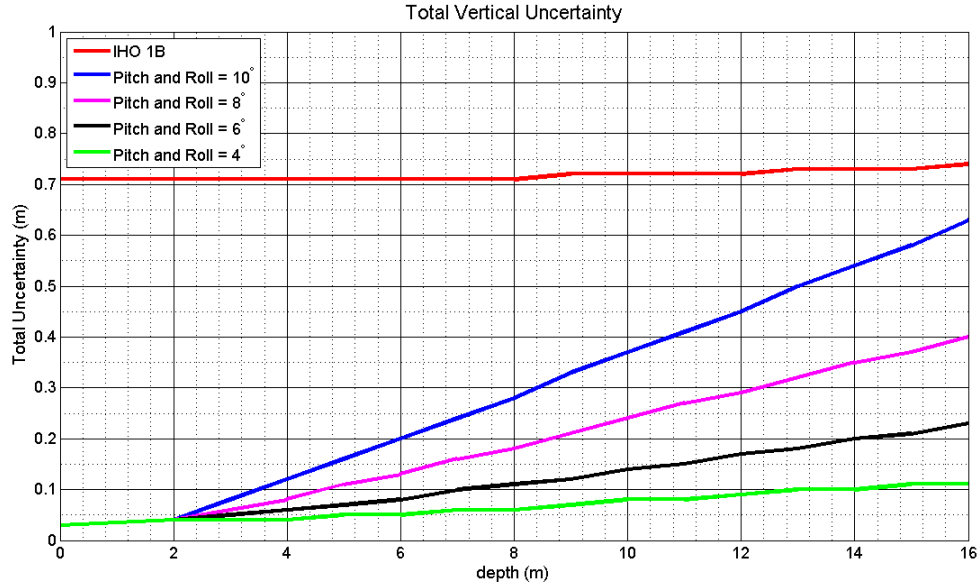


**Figure 3.4:** Vertical uncertainty at 95% confidence interval for echosounder system offset, sound speed and roll and pitch angles between 4 and 10 degrees.

temperature ( $T$ ) and pressure can affect the speed at which the sound travels. To approximate an average speed of sound,  $C_s$ , during the survey, the Mackenzie (1981) equation was used:

$$C_s = 1448.96 + 4.591T - 5.304 \times 10^{-2}T^2 + 2.374 \times 10^{-4}T^3 + 1.340(S_a - 35) + 1.630 \times 10^{-2}d + 1.675 \times 10^{-7}d^2 - 1.025 \times 10^{-2}T(S_a - 35) - 7.139 \times 10^{13}T. \quad (3.2)$$

Average values of 35 ppt, 30.49 °C and 3.66 m were estimated for salinity, temperature and average depth, respectively, given the historical conditions of the site. A final sound speed of 1,546 m/s was used to adjust the depth measurements. The maximum vertical uncertainty ( $1B_{error}$ ) to achieve an IHO 1B standard is given by:

$$1B_{error} = \sqrt{0.5^2 + (0.013d)^2}. \quad (3.3)$$

From Figure 3.4, it can be observed that for calm conditions, having pitch and roll angles equal

or less than 10 degrees, the system complies with the IHO 1B standard for depths under 16 meters.

### 3.1.3 Data processing

The acquisition software RTKLIB is able to do network RTK with the YUAN10 GPS and a mobile internet modem connected to one of the GPS stations operated by the Puerto Rico Seismic Network. The software combines the data streamed from the GPS and Sonarmite BT echosounder into a single raw data file. Depth measurements with their respective time stamp are combined with NMEA 0183 output files from RTKLIB. Using MATLAB code the NMEA 0183 sentences are then interpreted to obtain horizontal positioning, height above ellipsoid, Horizontal Dilution Of Precision (HDOP), platform speed, and the number of satellites. Values recorded from less than 5 satellites, HDOP greater than 3 and vessel speed greater than 5 knots were considered unreliable. Due to the effect of the speed of sound, new depth measurements ( $D_c$ ) were obtained using the following equation (IHO, 2015):

$$D_c = d * \frac{C_s}{1500} + 1.95. \quad (3.4)$$

The final RTKLIB output results are three dimensional coordinates based on the World Geodetic System 1984 (WGS, 1984) datum, which are then transformed to the SPCS-PRVI with a vertical projection using the PRVD02 datum. A final grid-node spacing of 1 m was used after processing the survey track-lines using the ArcGIS TIN to Raster tool (ArcGIS, 2016). Depth contours were then generated from the grid at 0.25 m interval spacing. Figures 3.5 and 3.6 display a top view of the final bathymetric results for Bajo Blanco. Figure 3.7 shows a three-dimensional view of Bajo Blanco illustrating the relative shallow bathymetry of the sand shoal and a sudden increase in depth approximately 1 km from the coast.

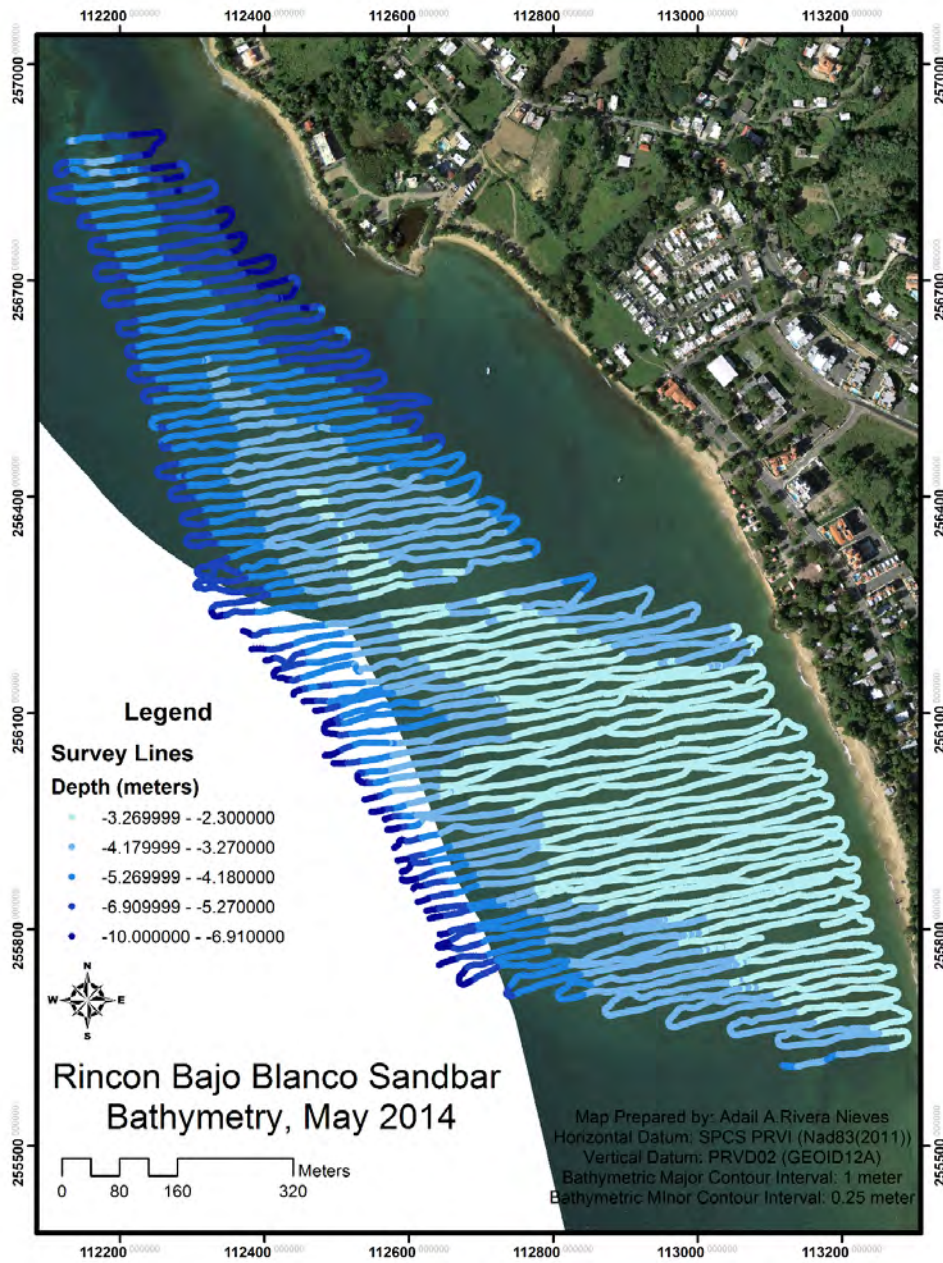


**Figure 3.5:** Survey route with the processed track points gathered at the Bajo Blanco sand shoal using the ArcGIS TIN to Raster tool.

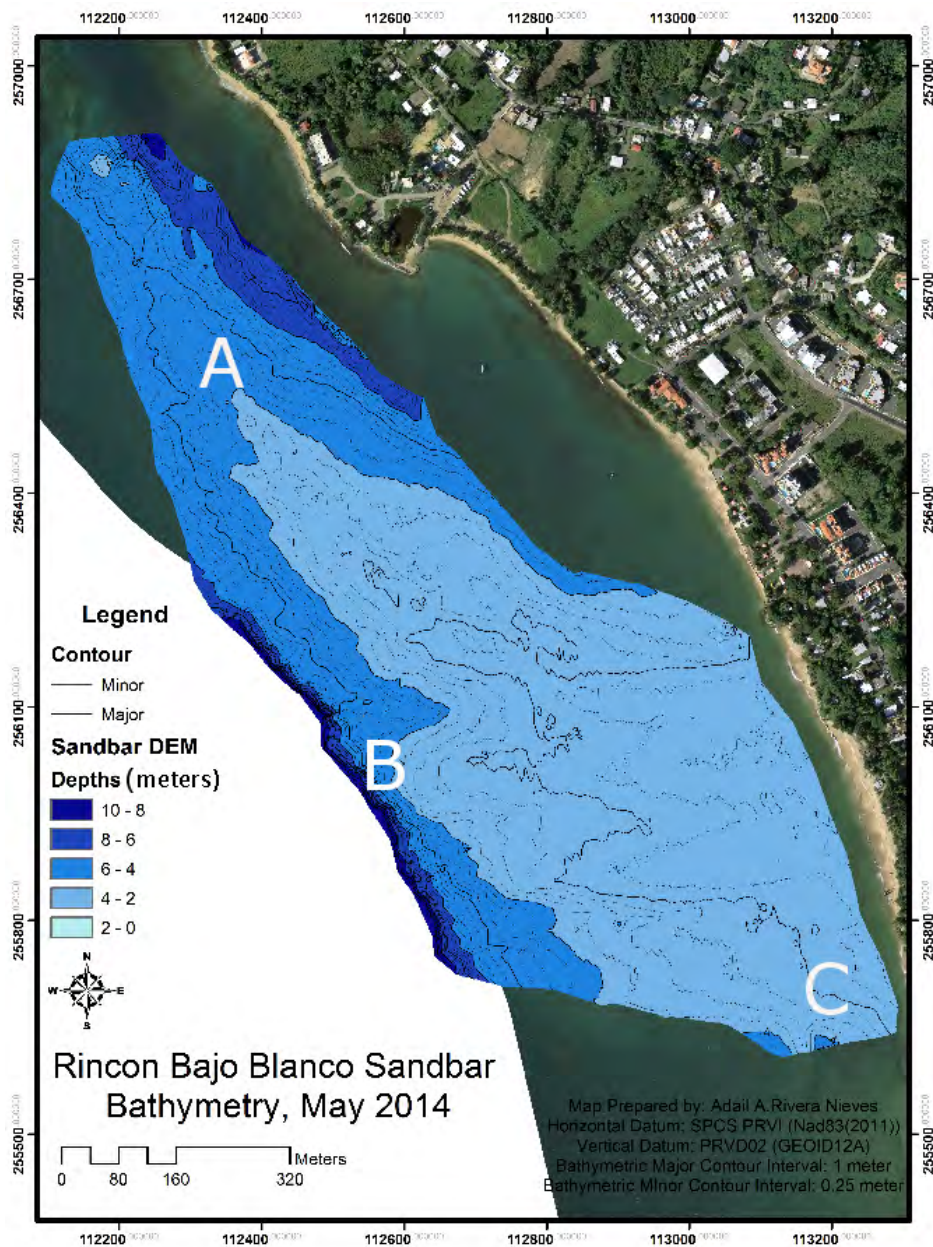


**Figure 3.6:** Survey bathymetric contour map with interpolated values using the ArcGIS TIN to Raster tool. Letters A, B and C represent control points for location purposes.

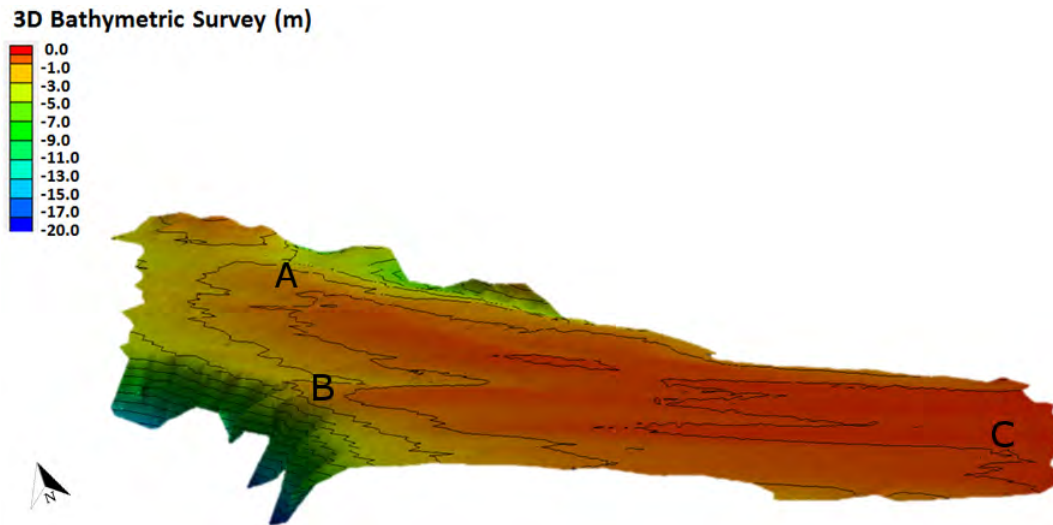


**Figure 3.7:** The Bajo Blanco sand shoal bathymetry (3D view). Letters A, B and C represent control points for location purposes.

### 3.1.4 Bathymetric survey results

The processed bathymetric data of May 23<sup>rd</sup>, 2014 was compared with the existing 10-meter resolution 2007 National Geophysical Data Center (NGDC, 2016) Digital Elevation Model (DEM) to determine bathymetric changes at the Bajo Blanco between 2007 and 2014. The objective is to compare the measured survey values from the present study with interpolated values from the 2007 NGDC DEM. The results of the comparison are shown in Figure 3.8, with color-coding indicating the differences in bathymetry caused by morphology change. The reddish colors represent sand deposition while the blueish colors represent erosion (sediment loss). The results suggest significant sediment transport and morphology change between 2007 and 2014. Given the fact that there is such a large time period between the measurements and that they were taken at different seasons of the year, it is difficult to draw clear conclusions regarding the causes for the morphology change. However, it is clear that the Bajo Blanco region is very dynamic from a morphological perspective. The banded patterns may suggest some sort of sand waves propagating over the sand shoal. The accretion region located southeast of the sand shoal may be a consequence of sediment discharge from Los Ramos ravine.

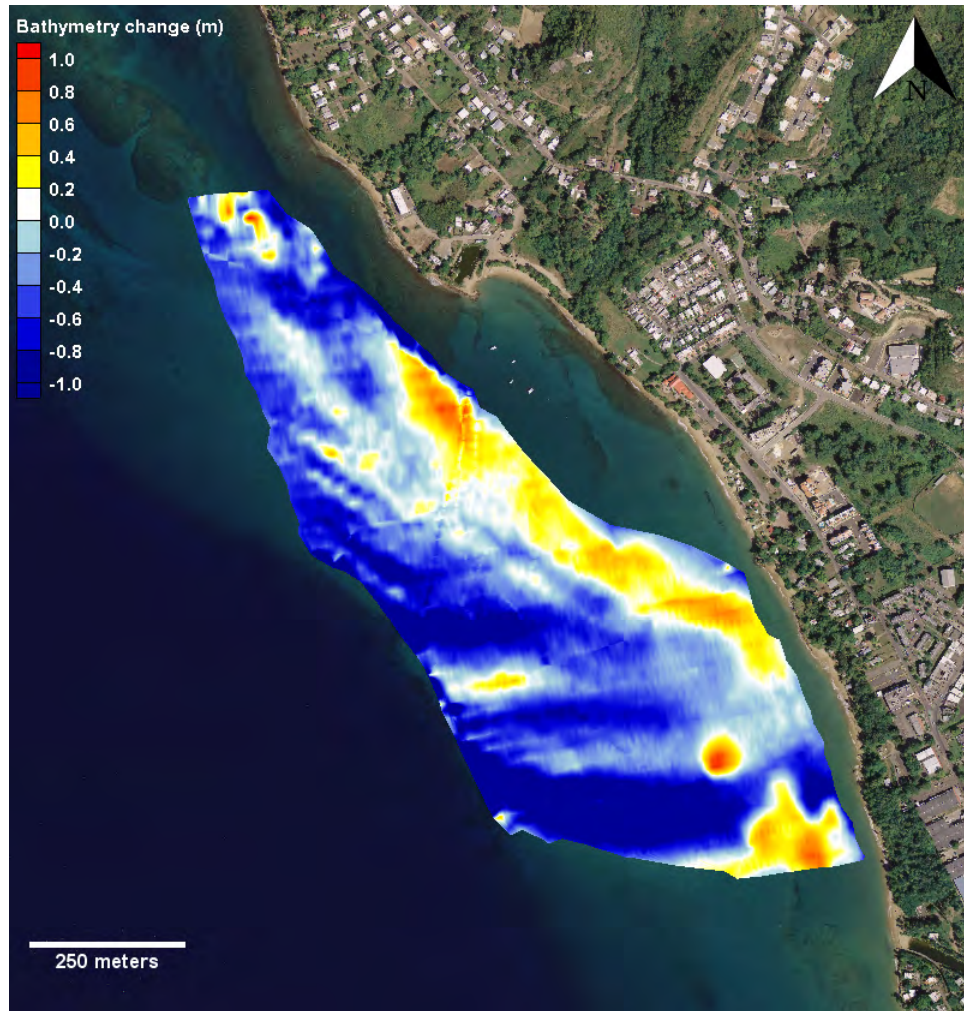


**Figure 3.8:** Comparison between the 2014 bathymetric data with the 2007 NGDC DEM bathymetry. The blueish and reddish color areas represent erosion and accretion, respectively.

Several observation profiles, as seen Figure 3.9, were extracted to compare the changes in water depth between both datasets. Results for transect 1, 2 and 3 are presented in Figures 3.10, 3.11 and 3.12, respectively. Cross sections 1 and 2 display significant changes between the datasets at both ends of the sand shoal. At the shallower region (center of the sand shoal), water depth appears similar between both datasets. Transect 3 has a smoother behavior when comparing both the baseline bathymetry and the NGDC DEM. For the three transects, the 2014 baseline bathymetry reflects deeper values offshore and shallower depths towards the coast when compared to the 2007 NGDC DEM data. Again, while it is difficult to draw conclusions regarding the mechanisms for the observed changes, the results suggest either a landward migration of the sand shoal as a whole, or sediment loss in deeper waters and sediment gain in nearshore waters. It is impossible to determine at the moment whether these changes are normal seasonal changes or a long-term trend, given the lack of data between 2007 and 2014.

### **3.2 Grain size compatibility analysis**

To properly determine potential borrow sites for eroded beaches it is important to understand the sediment composition and grain size characteristics of the study site. The quality and quantity of sand represents an important factor for evaluating the performance of a potential beach nourishment project. The quantity depends on the quality of the sand, which is related to the grain size parameter that determines the compatibility of the source. An analysis of sand compatibility is used to evaluate the similarity between the borrow site and area to be nourished.

An overfill factor (or overfill ratio) is used to describe the volume of sediment needed from the borrow site area including natural losses of borrow site sediments finer than the native beach sand (Dean, 1974). For instance, an overfill ratio,  $K$ , of 1.07 between the borrow area and the native sediment means that 93% of the dredge volume will remain in place after sediment sorting losses.

However, Dean's overfill factor method tends to be conservative resulting in small values of  $K$  (Bodge, 2006). Hence, the methodology used for the computation of the overfill factor is an

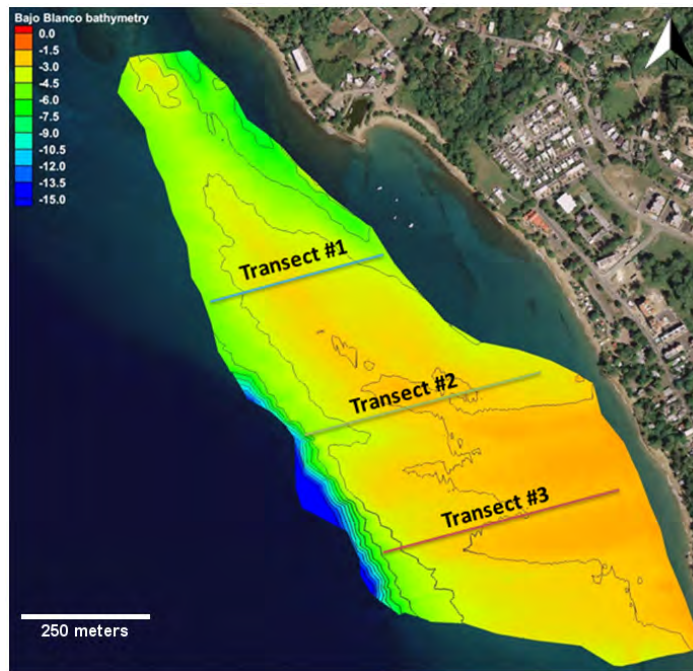


**Figure 3.9:** Observation profiles at Bajo Blanco to compare bathymetry of 2014 with NGDC DEM 2007.

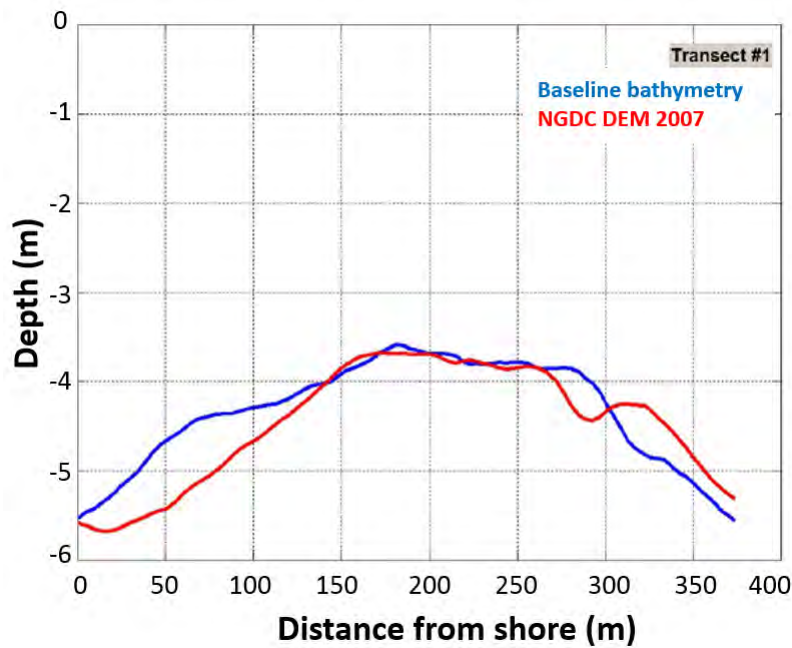


**Figure 3.10:** Transect near the Rincón Marina comparing the NGDC DEM 2007 data (red) and the jetski-based bathymetric survey results of 2014 (blue). The x-coordinate system is positive in the offshore direction.

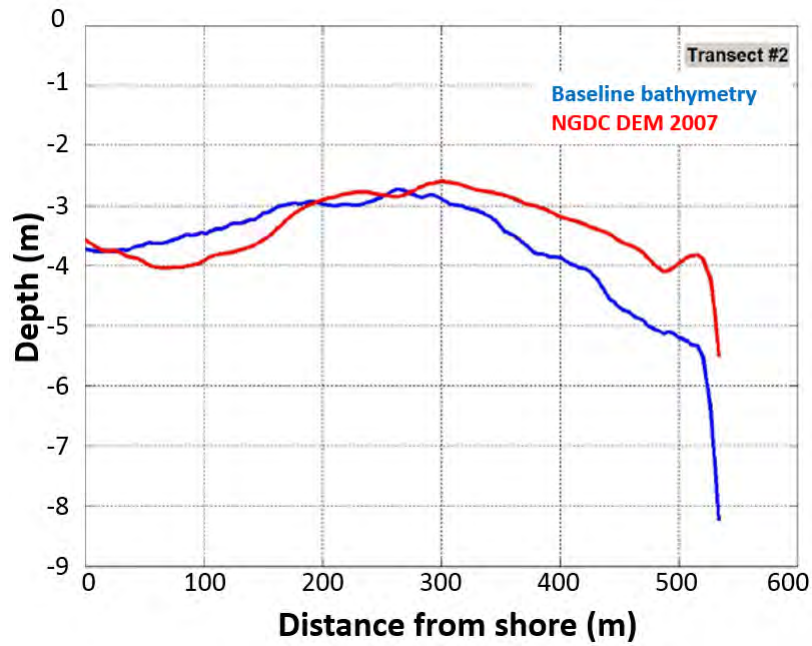


**Figure 3.11:** Transect located at Rincón public beach comparing the NGDC DEM 2007 data (red) and the jetski-based bathymetric survey results of 2014 (blue). The x-coordinate system is positive in the offshore direction.

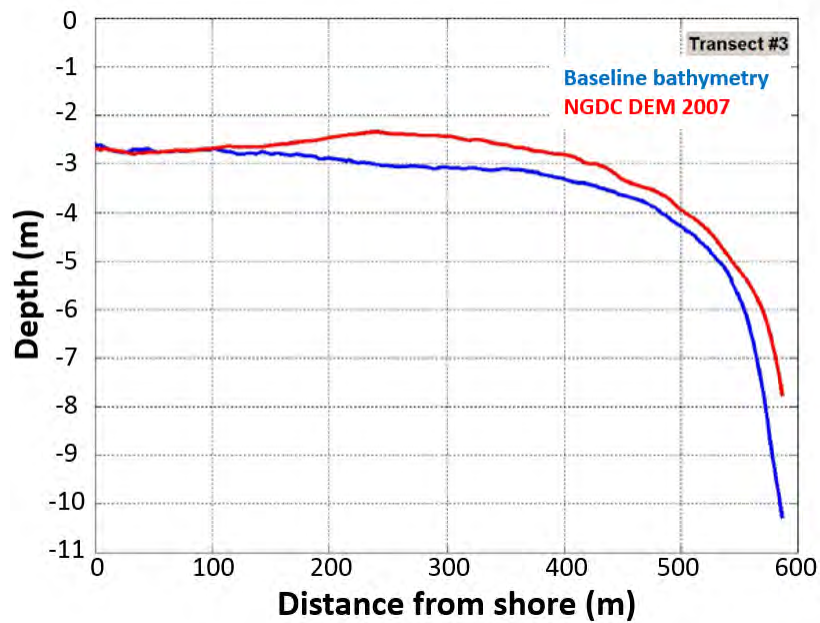


**Figure 3.12:** Transect near Los Ramos ravine comparing the NGDC DEM 2007 data (red) and the jetski-based bathymetric survey results of 2014 (blue). The x-coordinate system is positive in the offshore direction.

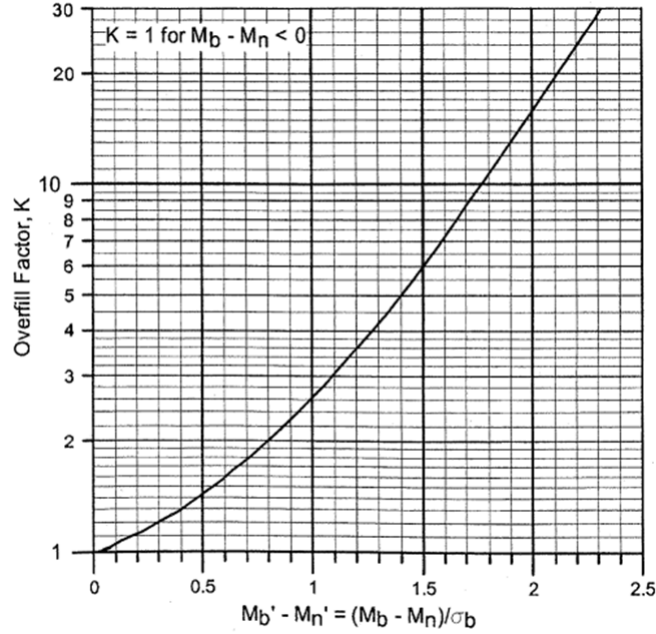


**Figure 3.13:** Alternative computation of Dean’s overfill factor as a single curve using dimensionless parameters  $M'_b$  and  $M'_n$  (Bodge, 2006).

alternative computation of Dean’s overfill ratio derived by Bodge (2006). This method yields the same numeric results as the original Dean curves, but uses a single curve for multiple sediment size cases. Dean’s overfill factor can be calculated by an iterative solution of two coupled equations, or it can be obtained graphically using the overfill ratio curves shown in Figure 3.13. The graphical method relies on dimensionless parameter  $M'$  defined by Dean (1974), using equation 3.5 for the respective grain size data of the native sand,  $M'_n$ , and borrow sand,  $M'_b$ .

$$M' = \frac{M}{\sigma_b}. \quad (3.5)$$

The parameter  $M$  is the mean grain size obtained using the following equation:

$$M = \frac{\phi_{16} + \phi_{50} + \phi_{84}}{3}. \quad (3.6)$$

The standard deviation, or sorting parameter  $\sigma$ , for the borrow site ( $\sigma_b$ ) is calculated as follows:

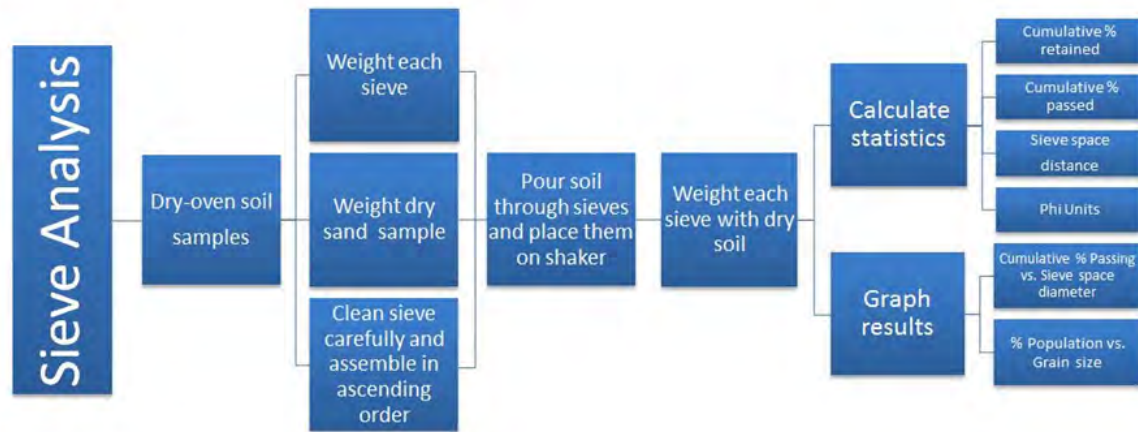


**Figure 3.14:** Sieve analysis procedure for fine sediments (Huyke, 2010).

$$\sigma_b = \frac{(\phi_{84} - \phi_{16})_b}{4} + \frac{(\phi_{84} - \phi_5)_b}{6}. \quad (3.7)$$

The grain size data can also be given in phi units to simplify statistical computations and graphical representations (Dean, 1974). The  $\phi_y$  refers to the grain size in the negative base-2 logarithmic form, for which  $y$  percent of the sediments is coarser. Equation 3.8 is used to change from millimeters to phi units, where  $m$  is the sediment grain size in millimeters (Bodge, 2006).

$$\phi = -3.322 \log m. \quad (3.8)$$

### 3.2.1 Sieve analysis

Generally, sediment grain size is characterized by sieving. The procedure is fast and accurate enough for most purposes, and is conducted following the diagram shown in Figure 3.14. Through statistical methods, the sieve data can be graphed to obtain useful information such as the median and mean grain size, significant percentage of coarse and fine particles, as well as sorting class

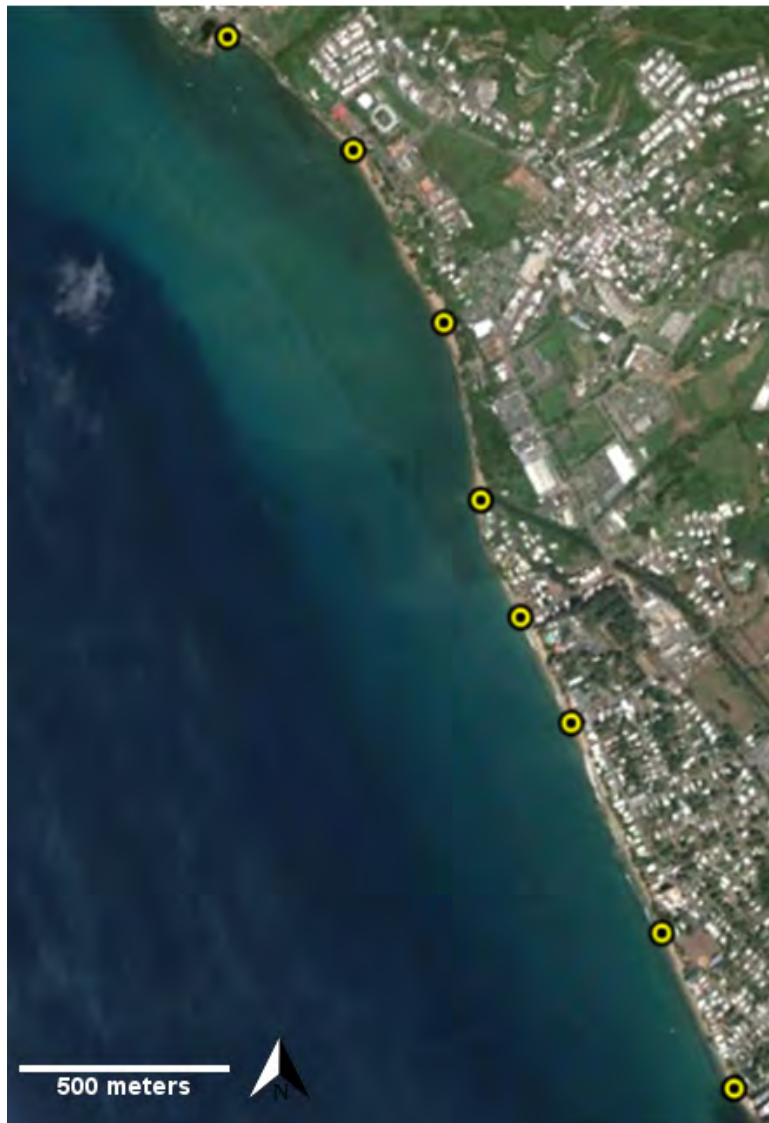


**Figure 3.15:** Location of the 8 samples collected along the coast of Rincón in segments of approximately 400 to 600 meters.



**Figure 3.16:** Location of the 18 samples collected at the Bajo Blanco with an average spacing of 300 meters between samples.

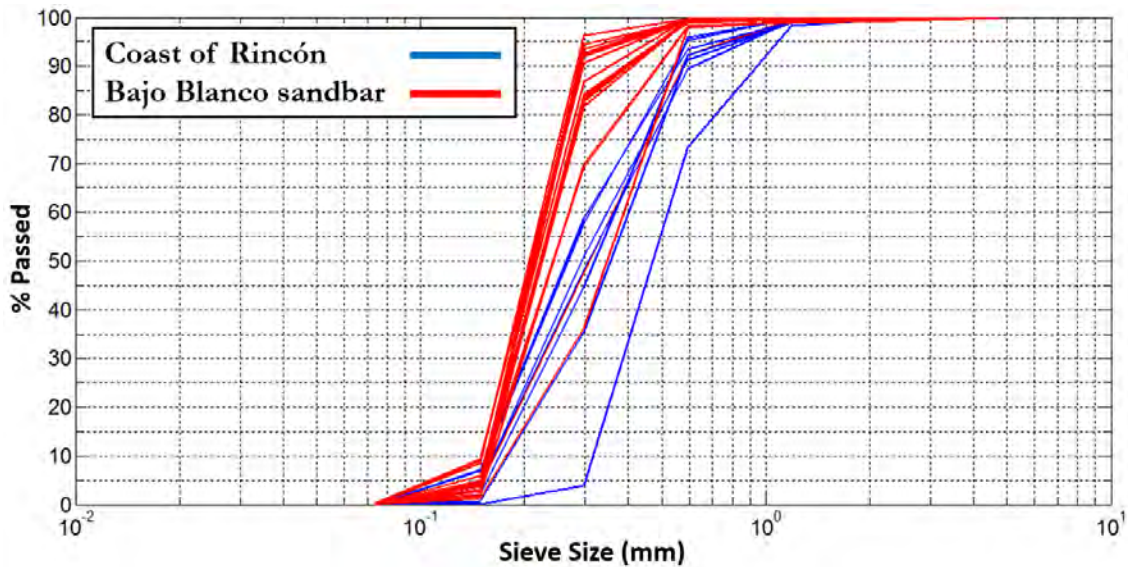


**Figure 3.17:** Percent passing and sieve size logarithmic plot for native sand samples (blue) and borrow site sand samples (red). Sorting properties are similar between both sites, displaying characteristics of well-sorted grain size samples.

(Huyke, 2010). Sorting is the tendency for the grains to be in the same class of grain size. A well sorted particle sample means the grains are all nearly the same size. Cumulative curves are useful to determine such characteristics using the percentage of sediment passing through each sieve and the space diameter of the sieve.

### 3.2.2 Sieve analysis results

On November of 2013, a total of eight (8) native sediment samples were collected along the coast of Rincón over a distance of approximately 3.2 km, from the Rincón Marina to Córcega Beach. Three months later, on February 2014, a total of eighteen (18) sand samples were collected from the seabed at the Bajo Blanco sand shoal. Figures 3.15 and 3.16 show the location of the samples at the coast of Rincón and Bajo Blanco, respectively. For all samples approximately 1600  $cm^3$  of sand was collected and at least 500 grams was used for the sieve and compatibility analysis. The samples were oven-dried and subjected to sieve analysis. The sieves ranged from sizes #4 to #200, equivalent to 4.76 mm and 0.074 mm respectively. After each test, the sieves were cleaned

thoroughly such that no particles from the previous test were present in the mesh holes. The sieve shaker was left ON for approximately 1 minute. Particles that were trapped in-between the holes of the sieve mesh were re-examined to determine whether they passed through or not. Calculations were made for weight retained (%), weight passing (%) and their respective cumulative weights (%). Figure 3.17 presents the results for percent passing (%) vs. sieve size for the native (blue) and borrow (red) sand samples. The plot was used to compare sorting properties and grain size compatibility. Results show how the borrow site sediments have smaller grain size values when compared with the sand samples from the coast of Rincón. This suggest that Bajo Blanco has finer sediment particles and that a volume higher than the estimated would be needed for the success of the beach nourishment design. Figures 3.18 and 3.19 display the mean grain size results for the native and borrow site sediments at each sample's location and as a contour color map, respectively.

Results show a consistent mean grain size value at Bajo Blanco, ranging from 0.22 mm – 0.25 mm. Near the Rincón Marina entrance and Los Ramos ravine, sediment grain size samples were coarser and darker due to mineral fragments and shells, possibly due to terrigenous sources. Along the eroded beaches, sediment grain size varies from 0.27 mm - 0.50 mm. The lowest mean grain size value was found at Rincón's public beach and Córcega beach, two recreational beaches with major tourist activity and with very severe erosion issues (see Appendix A).

The relatively homogeneous grain size distribution at the seabed of the Bajo Blanco sand shoal brings about the issue of whether the same homogeneity exists beneath the seafloor. To analyze this in more detail, four sediment cores of approximately 2 feet deep were collected at the Bajo Blanco sand shoal. The location and sand samples collected are shown in Figure 3.20. The cores were made by divers using PVC tubes. After a grain size analysis following the procedures described in the preceding pages, a comparison with surface samples showed there was no variation between the seafloor and the sediment collected from the cores along Bajo Blanco. This suggests that there is significant sediment suspension and transport during wave events, which forms a very homogeneous sediment distribution in the horizontal and vertical directions at the sand shoal.

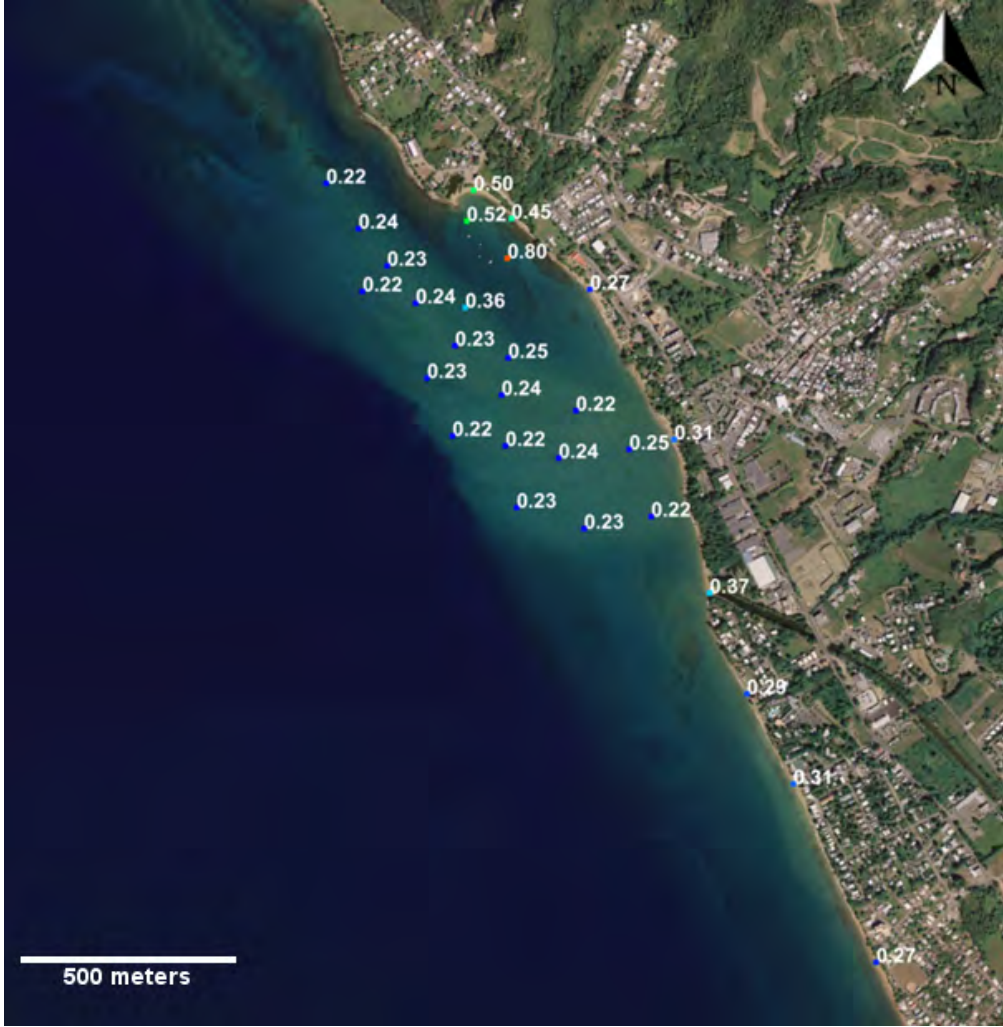


Figure 3.18: Mean grain size results for Bajo Blanco and beaches from Rincón Marina to Córcega beach.

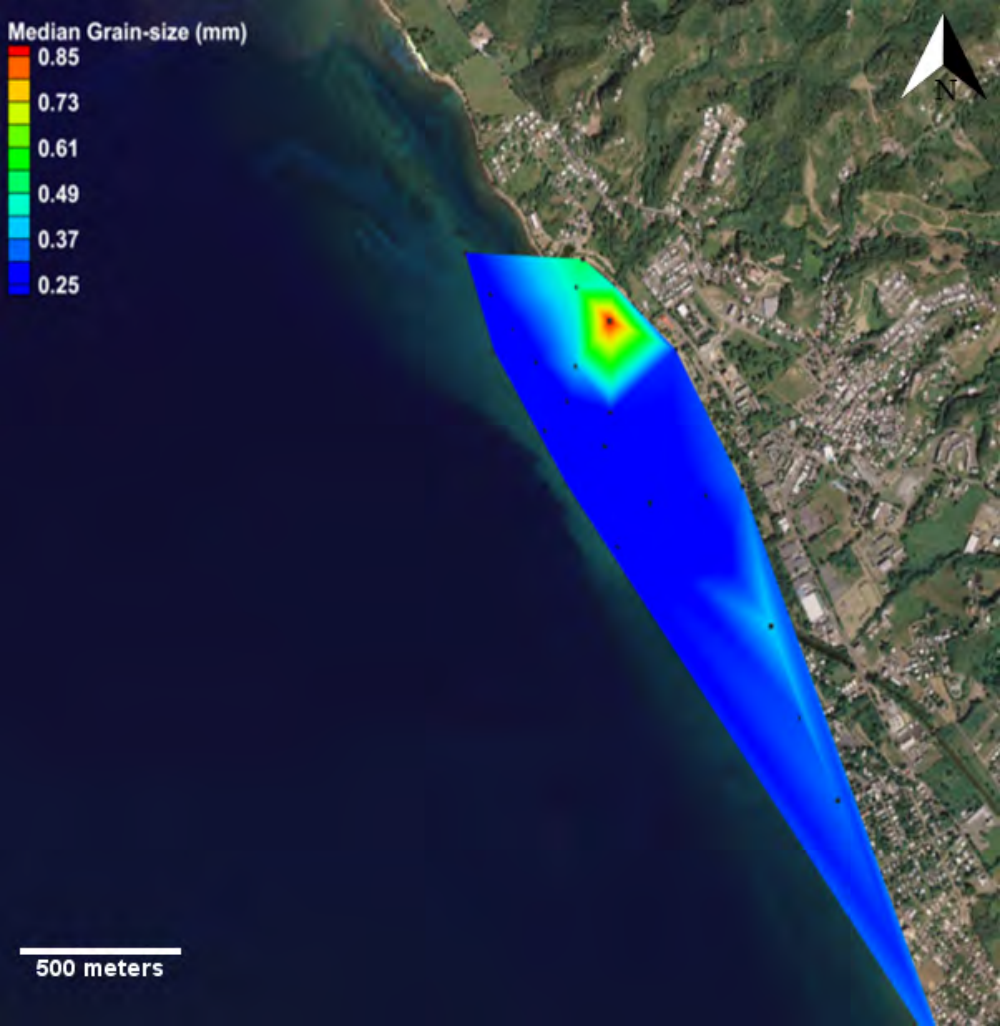


Figure 3.19: Mean grain size contour color map for Bajo Blanco and beaches from Rincón Marina to Córcega beach.



Samples from the of Rincón.



Samples from the Bajo Blanco sand shoal.

**Figure 3.20:** Image presenting the location of the core samples at the Bajo Blanco sand shoal. The collected samples showed no variation in sediment grain size less than 2 feet from the seafloor.

### 3.2.3 Compatibility analysis results

After nourishing and widening a beach, sand from the borrow site may erode faster than the native sand if full compatibility is not possible. In theory, the borrow sand should be slightly coarser or identical to the native sand to achieve beach stability. The coarser the grain size, the less likely it is to be eroded by nearshore currents and waves (Dean and Dalrymple, 2004). According to Dean (1991), grain size also influences the slope of the nearshore, and mild slopes are usually associated with finer grain sizes. Using beach profiles, Salas (2014) estimated the required sand volume for a design beach profile along a stretch of the coast of Rincón, as presented in Figures 3.21 and 3.22. Rincón’s most eroded beaches are on a long, straight stretch of coast. As a result, any beach nourishment project should include nourishing along the entire stretch of coast from Rincón Public Beach to Córcega rather than at individual locations, since introducing any significant alongshore



**Figure 3.21:** Schematic showing existing bathymetry contours (magenta) along with the depth of closure (red) and the calculated beach profiles elevation (yellow) (from Salas, 2014).

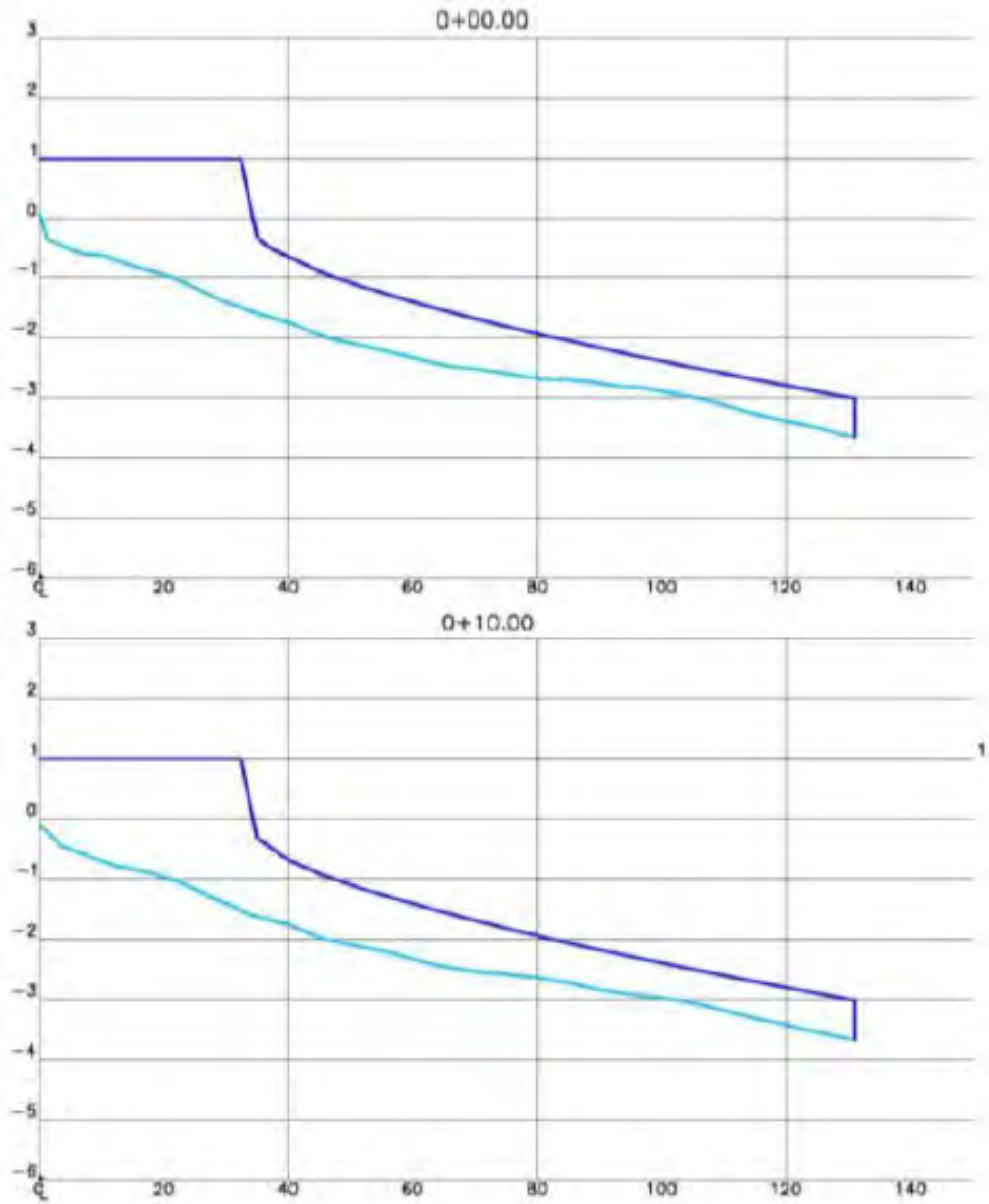


**Figure 3.22:** Observation profile showing the existing beach profile (cyan) and the calculated beach profile (blue) (from Salas, 2014).

heterogeneity could alter alongshore sediment transport dynamics, leading to unintended consequences for nearby beaches. According to Salas (2014), the final beach nourishment design for a 35 m berm width extends 300 m from the shoreline to a depth of 6 meters. If this same design profile is extended from the Rincón Marina to Córcega beach, an estimated volume of  $675,736 m^3$  of sand would be needed to nourish the area of interest. While this is a preliminary estimate, it is a useful starting point and provides a first estimate of the volume of sand necessary for a beach nourishment project in Rincón.

For the current analysis, the alternative computation of Dean's overfill ratio (Bodge, 2006) was used to study the compatibility between the sites. Figure 3.23 provides the results of the analysis if the mean grain size from the recreational beaches of the coast of Rincón (0.27 mm) is compared with each of the sand samples along Bajo Blanco. From the results, it is evident that the sand shoal region closer to the shore is more compatible than the leeward side of the sand shoal. These overfill values suggest that approximately between 50 - 70 percent more sand would be needed to successfully complete the final beach nourishment design. Although there is considerable uncertainty regarding the exact volume of extraction, preliminary computations suggest an amount on the order of  $1 \times 10^6 m^3$ .

An interesting problem is the location of the Bajo Blanco sand shoal. Typically, beach nourishment procedures require extracting sand from an offshore location to avoid interfering with nearshore sediment transport processes and the local sand budget. Bajo Blanco serves as a protective barrier for Rincón against wave events, and sand extraction from this region could lead to unintended consequences. Nevertheless, the short distance to the proposed nourishment area would significantly reduce the transportation costs of the extracted material. Bajo Blanco has a very complex morphodynamic system as already seen in Figure 3.8. The following chapters will address the potential impact of nearshore sand extraction on the wave climate and nearshore hydrodynamics using a numerical wave/current model.



**Figure 3.23:** Dean's overfill factor for the mean grain size of Bajo Blanco and the mean grain size from eroded beaches in Rincón.

### 3.3 Concluding remarks

In this chapter, a jetski-based bathymetric survey along the Bajo Blanco sand shoal was performed to measure the baseline bathymetry for the numerical model. The survey results were compared with the NGDC DEM from 2007. Significant differences in water depth between both datasets confirms that the Bajo Blanco sand shoal is a highly complex morphodynamic system, with the 2014 bathymetry showing larger depths in the offshore part of the sand shoal when compared to the NGDC DEM data.

Sand samples were collected at 18 sites in the Bajo Blanco sand shoal and at 8 locations along the most eroded beaches in Rincón. An average sediment grain size between 0.27 mm and 0.50 mm was observed at the beach locations. Finer grain sizes were found at Córcega and Rincón's public beach, whereas coarser sediments dominated the Rincón Marina beach and the Los Ramos ravine outlet. Bajo Blanco sample results were very homogeneous, with grain sizes ranging between 0.22 mm and 0.25 mm. Sediment cores at Bajo Blanco reflected similar properties to those at the seabed surface, indicating vertical homogeneity. It is evident that Bajo Blanco is composed of finer sediment particles when compared with sediments from Rincón's most eroded beaches. This raises questions regarding the origin of this sand (at Bajo Blanco) and whether it is partially composed of sediment discharges from nearby ravines or transported from remote sources by wave-induced currents during large wave events.

The beach nourishment design suggested by Salas (2014) was extended from the Rincón Marina to Córcega beach, yielding an estimate of approximately  $675,736 m^3$  of sand necessary for a beach nourishment project. An analysis using Dean's overfill factor suggests that an additional 50 - 70% of sand would be needed for the success of the design beach profile. Although there is considerable uncertainty regarding the exact volume of extraction, preliminary computations suggest an amount on the order of  $1 \times 10^6 m^3$ . Due to the complex morphodynamic behavior of the Bajo Blanco sand shoal and its effect on the wave climate and nearshore processes, the potential effects

of sand mining such a volume of sand from Bajo Blanco will be evaluated in the next chapter using the USACE Coastal Modeling System numerical model.

## Chapter 4

# VALIDATION OF HYDRODYNAMIC NUMERICAL MODEL ON NEARSHORE WAVE CLIMATE

### 4.1 Introduction

The current chapter is concerned with the validation of a coupled wave, circulation and sediment transport model that will be used in Chapter 5 to evaluate the potential effects of sand mining the Bajo Blanco sand shoal on the nearshore hydrodynamics of Rincón. In order to quantify model performance, field measurements of waves and currents are compared to the results from the coupled CMS-Wave and CMS-Flow numerical models.

### 4.2 The Coastal Modeling System (CMS)

The Coastal Modeling System (CMS), developed by the U.S. Army Corps of Engineers (USACE), is a coupled two-dimensional (depth-averaged) wave-current-sediment transport numerical model used to simulate waves, hydrodynamics, sediment transport, morphology change, and salinity (Sánchez et al., 2012). It provides the tools to properly model nearshore coastal processes in navigational channels, ports, harbors, and coastal inlets. As shown in Figure 4.1, the CMS-Wave and CMS-Flow models exchange wave, current, and water level information as well as bathymetry changes due to the morphological response of the seabed. The current chapter evaluates the performance of these models in simulating the wave climate and hydrodynamics for the coast of Rincón during the early 2013 period.

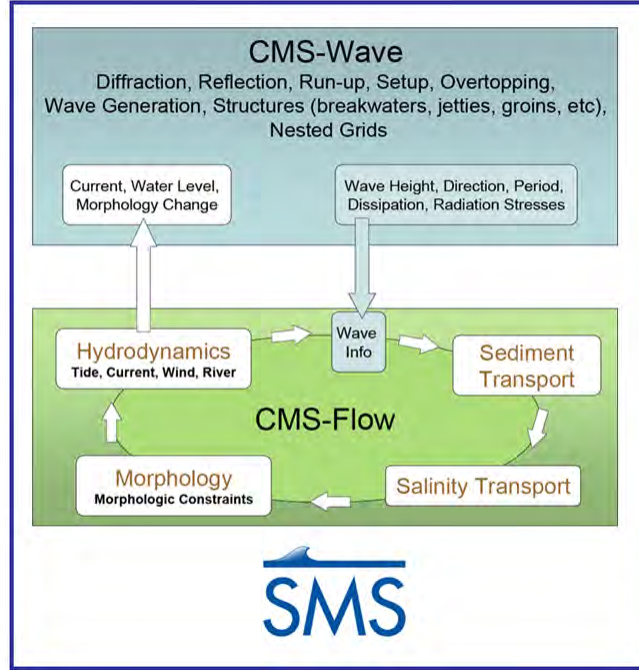


**Figure 4.1:** The Coastal Modeling System (CMS) integrates CMS-Wave and CMS-Flow into a coupled numerical model, allowing the sharing information between each model (Sánchez et al., 2012).

#### 4.2.1 CMS-Wave

CMS-Wave is a spectral wave transformation (phase-averaged) model solving the wave-action balance equation for most of the significant shallow water processes including refraction, shoaling, wave-current interactions, wind wave growth, depth-induced breaking, and bottom friction (Lin and Demirbilek, 2012). Being a phase-averaged model, it does not resolve changes in the wave phase during the calculation of nearshore processes, but it only considers the changes that occur in the wave energy density. The model solves the two-dimensional variation of spectral wave energy density in space and time using the following equation:

$$\frac{\partial N}{\partial t} + \frac{\partial C_{gx}N}{\partial x} + \frac{\partial C_{gy}N}{\partial y} + \frac{\partial C_{g\theta}N}{\partial \theta} = \frac{\varepsilon}{\omega} \left( \frac{\partial}{\partial x} (C_g \frac{\partial N}{\partial x}) + \frac{\partial}{\partial y} (C C_g \frac{\partial N}{\partial y}) + C C_g \frac{\partial^2 N}{\partial \theta^2} \right) + S \quad (4.1)$$

where  $C$  and  $C_g$  are wave celerity and group celerity, respectively;  $C_{gx}$ ,  $C_{gy}$ , and  $C_{g\theta}$  are the characteristic wave velocities with respect to  $x$ ,  $y$ , and  $\theta$  directions;  $\omega'$  is the wave relative frequency;  $\theta$  is wave direction;  $k$  is the wave number;  $S$  denotes the sources and sinks of energy;  $\varepsilon$  is the coefficient of directional diffusion of wave energy on the order of  $10^{-4}$  values, while  $N$  is the wave-action density, defined as  $N = E / \omega'$ , where  $E$  is the wave energy as a function of frequency and direction (Sánchez et al., 2012).

The CMS-Wave model only operates with uniform or nonuniform grids and does not allow for the use of a telescoping grid (as opposed to CMS-Flow). It provides a user-friendly graphical interface to adjust model parameters such as spectral source, bed friction, wind magnitude, current magnitude, and water level input forcing. It simulates wave propagation in a directional half-plane corresponding to the seaward boundary of the model grid. The output results from the numerical model include significant wave height, wave period, wave direction and wave energy dissipation. This data is passed as input, as wave forcing stresses, to the CMS-Flow circulation model.

The spectral wave boundary conditions for CMS-Wave are obtained from directional spectra measured by the CariCOOS Rincón wave buoy, as explained in the next section.

### ***Spectral development from wave buoy data***

The CariCOOS Waverider buoy located in Rincón registers horizontal and vertical displacements using accelerometers which adjusts the wave direction through pitch and roll sensors. Spectral data is provided as Fourier coefficients  $a_1$ ,  $a_2$ ,  $b_1$  and  $b_2$  which are used as components for the development of wave energy spectra representative of the wave climate conditions near coastal regions.

A two-dimensional wave energy spectrum  $S(f, \theta)$  describes the distribution of wave energy density as a function of wave direction ( $\theta$ ) and wave frequency ( $f$ ), and can be expressed as follows:

$$S(f, \theta) = E(f)D(f, \theta) \tag{4.2}$$

where the parameter  $E(f)$  is the non-directional spectral density, a function of frequency only; and  $D(f, \theta)$  is the directional spreading function (DSF), a function of frequency and direction. The DSF is defined as the angular distribution of energy and satisfies equation 4.2 as follows:

$$\int_{-\pi}^{\pi} D(f, \theta) d\theta = 1 \quad (4.3)$$

Longuet-Higgins et al. (1963) developed a directional Fourier series approach using Fourier parameters  $r_1, r_2, \theta_1,$  and  $\theta_2$ . These parameters were obtained from Fourier coefficients ( $a_1, a_2, b_1$  and  $b_2$ ) collected by a directional wave buoy. The DSF corresponding to the Fourier series can be written as:

$$D(f, \theta) = \frac{\frac{1}{2} + r_1 \cos \theta - \theta_1 + r_2 \cos 2(\theta - \theta_2)}{\pi} \quad (4.4)$$

where  $r_1$  and  $r_2$  are the first and second normalized directional Fourier parameters, respectively, calculated as:

$$r_1 = \sqrt{a_1^2 + b_1^2} \quad r_2 = \sqrt{a_2^2 + b_2^2} \quad (4.5)$$

The parameters  $\theta_1$  and  $\theta_2$  are the mean and principal wave direction, respectively, computed using the following equations:

$$\theta_1 = \tan^{-1} \frac{b_1}{a_1} \quad \theta_2 = \frac{1}{2} \tan^{-1} \frac{b_2}{a_2} \quad (4.6)$$

Applying equation 4.2 with the DSF of the directional Fourier series, we can determine a directional wave energy spectrum as follows:

$$S(f, \theta) = \frac{E}{2} + a_1 \cos \theta + b_1 \sin \theta + a_2 \cos 2\theta + b_2 \sin 2\theta \quad (4.7)$$

This technique proposed by Longuet-Higgins et al. (1963) is known as the Truncated Fourier Series decomposition method (TSF). Although it is a relatively easy and efficient approach, it may occasionally produce negative values, which is not acceptable for a DSF (Benoit et al., 1997). Longuet-Higgins et al. (1963) introduced a modified version of this approach known as the Weighted Fourier Series decomposition method (WFS), adding weighting values to compensate for the negative energy obtained from the TFS. The DSF and directional wave energy spectrum for this approach are shown in equation 4.8 and 4.9, respectively. However, this approach is less reliable since it increases the half-power width to 130 degrees (Earle, 1996).

$$D(f, \theta) = \frac{\frac{1}{2} + \frac{2}{3}r_1 \cos \theta - \theta_1 + \frac{1}{6}r_2 \cos 2(\theta - \theta_2)}{\pi} \quad (4.8)$$

$$S(f, \theta) = \frac{E}{2} + \frac{2}{3}a_1 \cos \theta + b_1 \sin \theta + \frac{1}{6}a_2 \cos 2\theta + b_2 \sin 2\theta \quad (4.9)$$

Longuet-Higgins et al. (1963) proposed another spreading function later modified by Mitsuyasu et al. (1975) based on deep water field measurements, wind speed, and peak spectral frequency. The approach is known as the Cosine Power '2s' directional spreading model (CPM) and can be calculated using the following equation:

$$D(f, \theta) = \Delta(s) \cos^{2s} \frac{\theta - \theta_{1,2}}{2}. \quad (4.10)$$

The normalization coefficient ( $\Delta s$ ) is derived from the condition of equation 4.3 and is written as:

$$\Delta(s) = \frac{2^{2s-1} \Gamma(s+1)^2}{\pi \Gamma(2s+1)} \quad (4.11)$$

where  $\Gamma(s)$  is the gamma function and  $s$  is the directional spreading factor calculated with equation 4.12 for rank 1 and 2, respectively (Lin, 2008).

$$s_1 = \frac{r_1}{1 - r_2} \quad s_2 = \frac{1 + 3r_2 + \sqrt{r_2^2 + 14r_2 + 1}}{2(1 - r_2)}. \quad (4.12)$$

All three methods mentioned above treat the wave energy directional distribution as an unimodal function since this type of distribution has been assumed in all wave models for scientific and engineering applications (Hwang, 2012). In order to determine which directional spreading function best-fit the wave climate conditions and bathymetric settings of Rincón, Puerto Rico, CMS-Wave was used to simulate halfplane directional wave spectra developed from the TFS, WFS and CPM. Results are compared with observing assets within TPMR.

### ***Grid development***

A non-uniform grid was generated with the adequate resolution to account for relevant nearshore physical processes, particularly in the surf zone. Grid cells are either squares or rectangles, as shown in Figure 4.2, with larger cells of 16 m x 16 m in the offshore region, and 4 m x 4 m cells in the nearshore and sand shoal areas. The computational domain of the grid extends 6.8 km x 4 km and was chosen based on the location of the CariCOOS waverider buoy, one mile off the Punta Higuero lighthouse coast in Rincón. The grid orientation points zero degrees (north) to properly capture the half-plane orientation of the shoreline in the modeled area.

The simulation period covers the months of January and February 2013, with a time step of 1 hour for a total of 1,416 hours. To describe bottom friction, a Manning's coefficient of  $n = 0.025$  was used for the numerical model as suggested by Zheng et al. (2013). The CMS-Wave model results for the TFS, WFS and CPM input wave forcing spectra are now compared wave data from pressure sensors and acoustic profilers discussed in the next section.

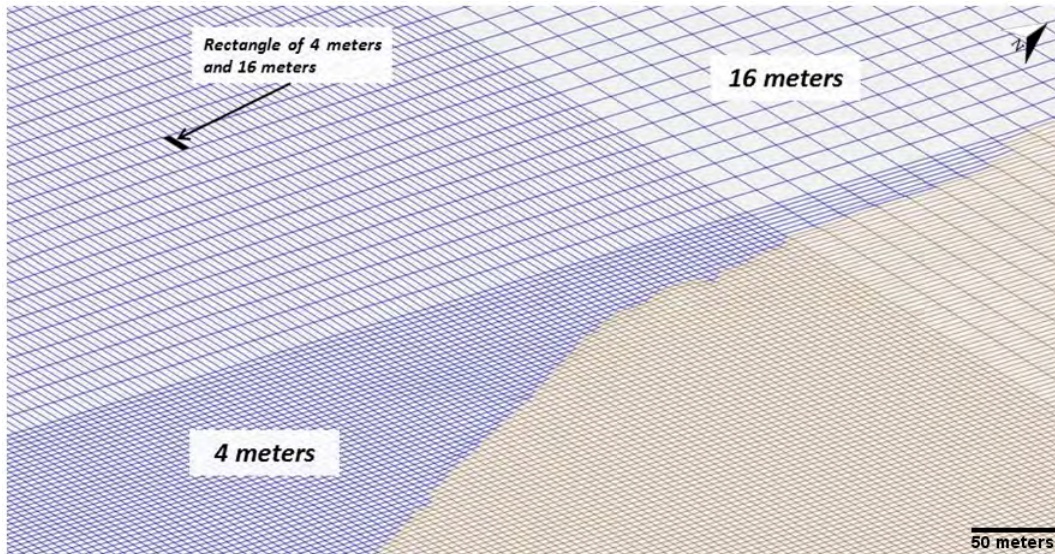


**Figure 4.2:** Non-uniform grid for the CMS-Wave model. This grid consists of 1126 x 687 cells with a maximum spatial resolution of 4 m in the nearshore region.

### *CMS-Wave validation results*

During the period between January 11<sup>th</sup> and February 25<sup>th</sup>, 2013, a field experiment was conducted to acquire wave and current data near the TPMR in Rincón, Puerto Rico. Figure 4.3 shows the location of two pressure sensors (PS2 and PS1) and an Acoustic Wave and Current Profiler (AWAC) used to measure the propagation and transformation of winter swell waves across the Tres Palmas reef, at a depth of 3.33 m, 6.54 m and 18 m, respectively. An additional Acoustic Doppler Current Profiler (ADCP) measured currents at a depth of 10 meters and closer to shore.

Through MATLAB routines, deep water wave conditions registered by the Waverider buoy were transformed into a set of two-dimensional wave energy spectra using the TFS, WFS and the CPM directional spreading functions. The CMS-Wave model simulated each half-plane wave energy spectrum and the model output was compared with field measurements from the two pressure sensors and the AWAC. Figure 4.4 – 4.6 provide a graphical comparison between the observing assets and the CMS-Wave results using the TFS (blue), WFS (red) and the CPM (green) spectral descriptions.

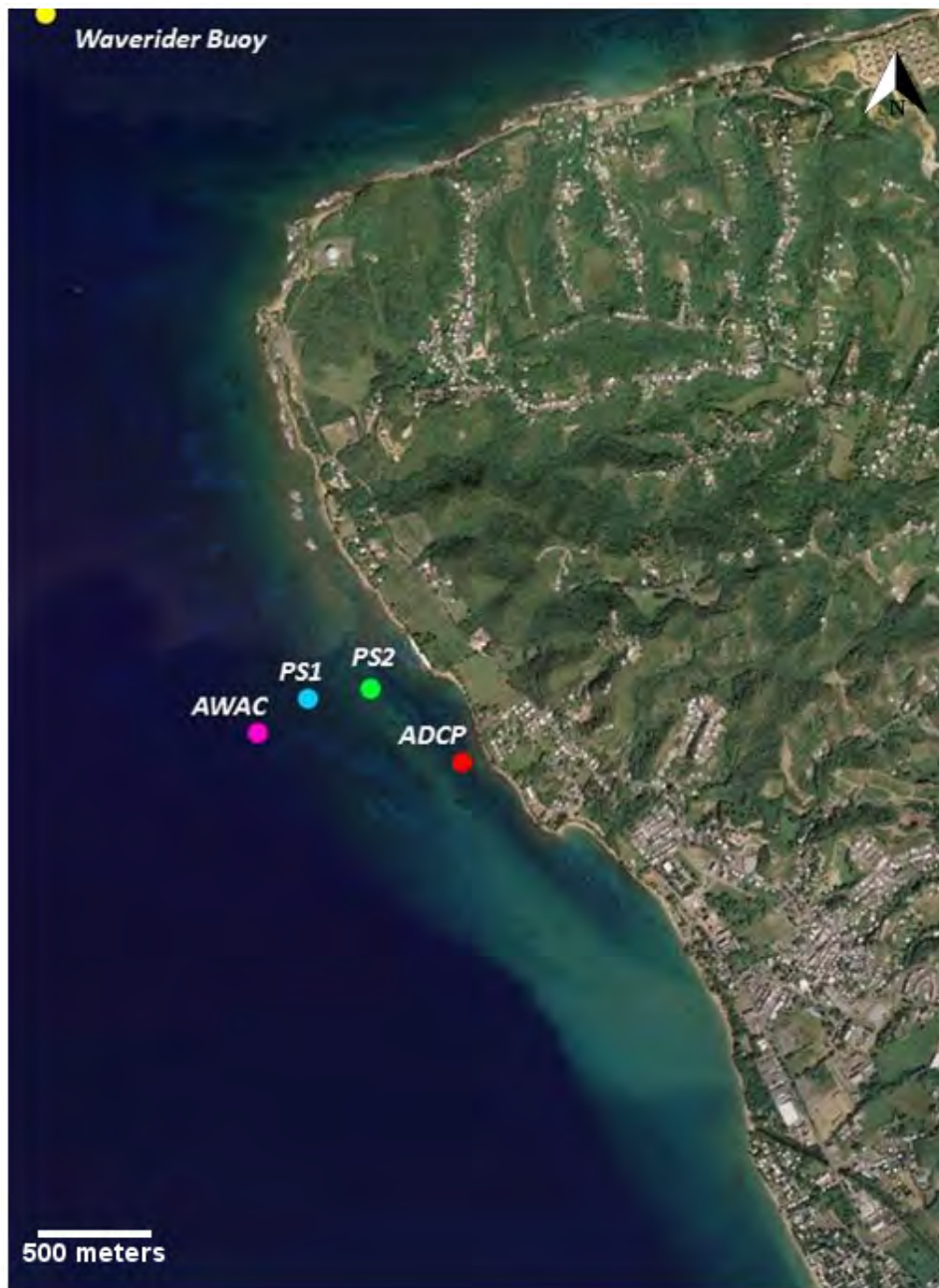


**Figure 4.3:** Location of the pressure sensors and current profilers installed at TPMPR to measure wave and current data from January 11<sup>th</sup>, 2013 to February 25<sup>th</sup>, 2013.

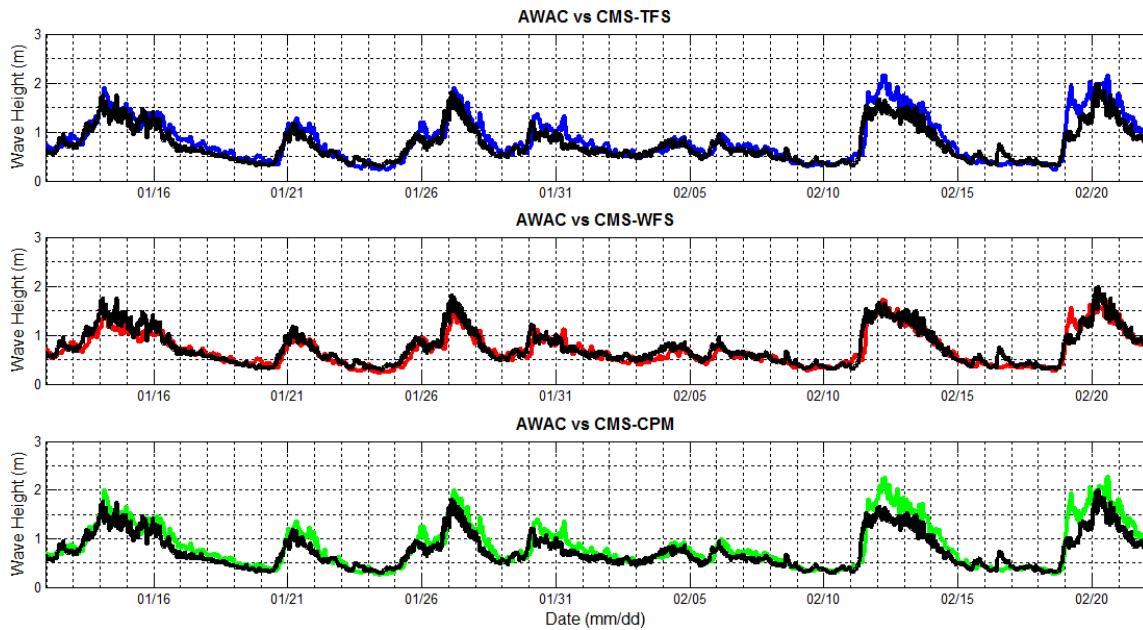


**Figure 4.4:** Time-series comparison between the observed (black) significant wave height at the AWAC and the CMS-Wave results using the TFS (blue), WFS (red) and the CPM (green) spectral descriptions.

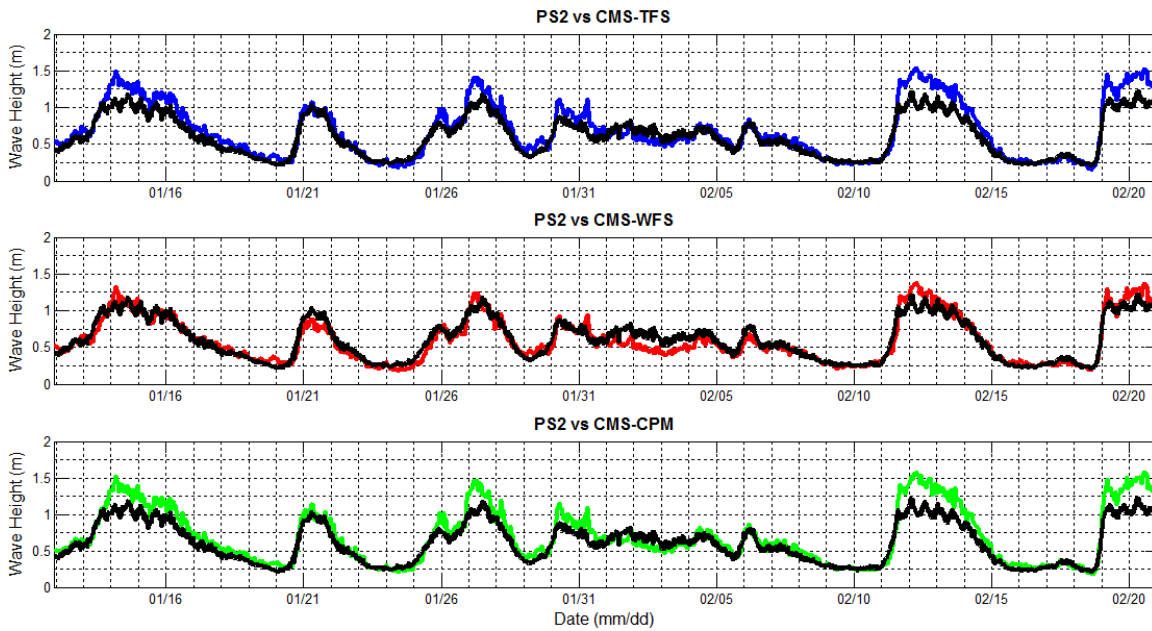


**Figure 4.5:** Time-series comparison between the observed (black) significant wave height at pressure sensor II (PS2) and the CMS-Wave results using the TFS (blue), WFS (red) and the CPM (green) spectral descriptions.

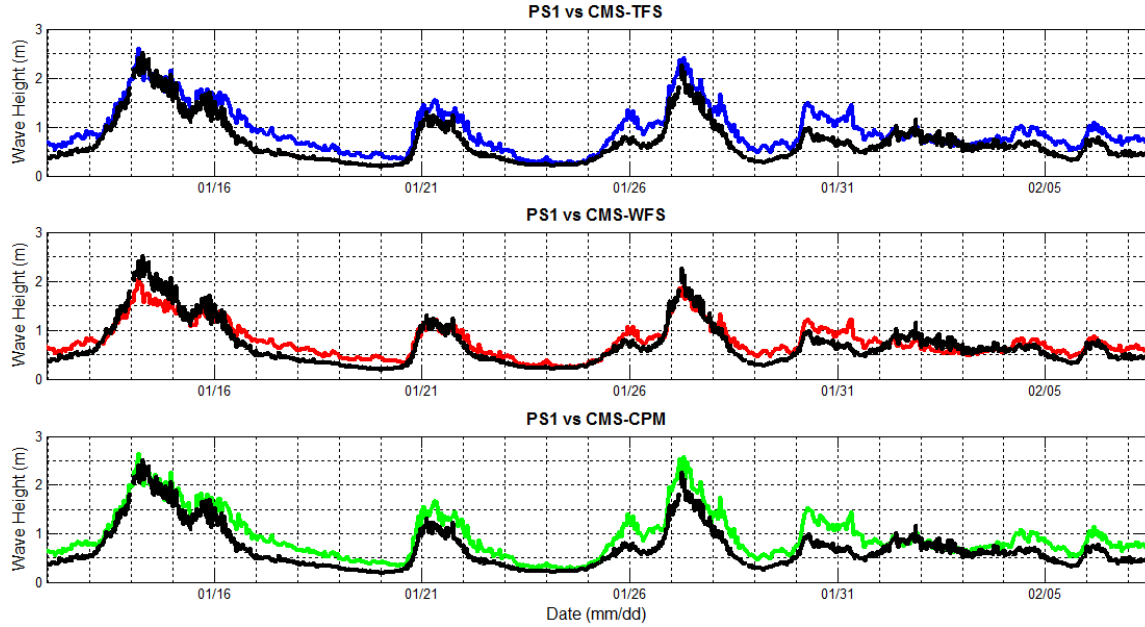


**Figure 4.6:** Time-series comparison between the observed (black) significant wave height at pressure sensor I (PS1) wave height and the CMS-Wave results using the TFS (blue), WFS (red) and the CPM (green) spectral descriptions.

CMS-Wave predictions show very good agreement with the observed (black) wave heights at all three locations, demonstrating satisfactory performance in propagating offshore waves captured by the buoy. Large wave height differences are seen throughout the time series comparison of PS2. This is due to the fact that PS2 was located inside the surf zone during large wave events, where it is difficult for a phase-averaged model to simulate wave energy dissipation due to breaking. As a result, CMS-Wave may tend to overestimate the wave height inside the surf zone as a consequence of inaccurately resolving breaking-induced dissipation.

Additionally, a linear correlation for the three wave energy spectra equations was performed resulting in nine graphical outputs shown in Figure 4.7. The correlation coefficient ( $R(i, j)$ ) was computed using the following formula:

$$R(i, j) = \frac{Q(i, j)}{\sqrt{Q(i, i)Q(j, j)}} \quad (4.13)$$

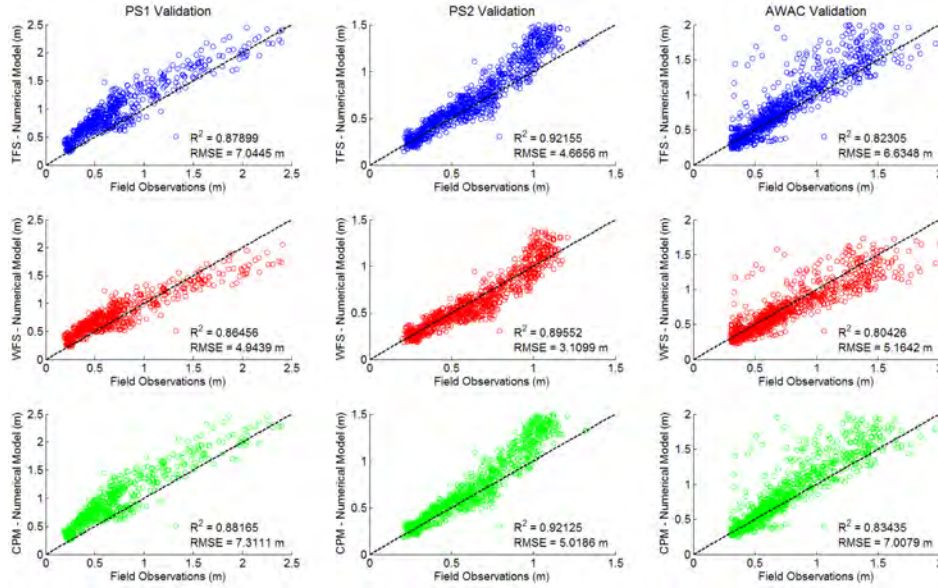


**Figure 4.7:** Linear correlation results for the time series comparison between the observed measurements and predicted CMS-Wave results. The Weighted Fourier Series (WFS) approach seems to have better prediction of both small and large magnitude wave events during the validation period.

where  $Q(i, j)$  corresponds to the numerical value of row  $i$  and column  $j$ . According to the results, the WFS provides more accurate wave height values compared with the field measurements from the three sensors with a maximum linear correlation of 89.6%. Although the TFS and the CPM provided better correlation results (92.1% each), they tend to overestimate high-energy wave events, as seen by the top scatter values above the 45 degree dotted line. The WFS provided the best approximation of wave propagation giving the Waverider buoy parameters and the merged bathymetry from both the NGDC DEM 2007 and the jetski-based bathymetric survey. USACE provides an executable to propagate the buoy wave parameters into the boundary's depth, but it also proved to be less accurate than the WFS decomposition method.

## 4.2.2 CMS-Flow model

CMS-Flow is a finite-volume numerical model which includes the capabilities to compute hydrodynamics (water levels and current flow values under any combination of tide, wind, surge, and waves), sediment transport (as bedload, suspended load, and total load) and morphology change

(Sánchez et al., 2012). It uses the two-dimensional depth-averaged continuity and momentum equations (equations 4.14 and equation 4.15 respectively) as follows:

$$\frac{\partial h}{\partial t} + \frac{\partial(hV_j)}{\partial x_j} = 0 \quad (4.14)$$

$$\begin{aligned} \frac{\partial(hV_i)}{\partial t} + \frac{\partial(hV_iV_j)}{\partial x_j} = & -gh\frac{\partial\eta}{\partial x_i} - \frac{h}{\rho}\frac{\partial p_a}{\partial x_i} + \varepsilon_{ij}f_c hU_j + \\ & \frac{\partial}{\partial x_j}(v_i h \frac{\partial(V_i)}{\partial x_j}) - \frac{1}{\rho}\frac{\partial}{\partial x_j}(S_{wij} + R_{sij} - \rho hU_{wi}U_{wj}) + \tau_{si} - \tau_{bi} \end{aligned} \quad (4.15)$$

where  $t$  is time;  $x_i$  and  $x_j$  are cartesian coordinates in the  $i^{th}$  and  $j^{th}$  direction, respectively;  $f_c$  is the Coriolis parameter;  $h = \zeta + \eta$  is the total water depth;  $V_i = U_i + U_{wi}$  is the total flux velocity;  $U_i$  is the phase and depth-averaged current velocity;  $U_{wi}$  is the mean wave mass flux velocity;  $g$  is the gravitational constant;  $p_a$  is the atmospheric pressure;  $\rho$  the water density;  $v_t$  is the turbulent eddy viscosity;  $\tau_{si}$  is the surface wind stress;  $\tau_{bi}$  is the combined wave-current mean bed shear stress;  $S_{wij}$  is the wave radiation stress;  $\varepsilon_{ij}$  is the permutation parameter and  $R_{sij} = 2E_r w_i u_j$  is the surface roller stress, where  $E_r$  is the surface roller energy (Sánchez et al., 2012). CMS-Flow has the flexibility to use either rectangular, non-rectangular or telescoping grid. The state-of-the-art telescoping grid provides the ability to refine the grid cell size in areas of interest.

### 4.3 CMS model set-up

The CMS model set-up discusses the input information for the CMS-Wave and CMS-Flow models. Using the inline steering module, the models exchange results in a way known as two-way coupling, where CMS-Wave provides radiation stresses to CMS-Flow, and receives water level and flow field input data from CMS-Flow. For both models, the simulation period is 1,416 hours from January 1<sup>st</sup> to February 28<sup>th</sup>, 2013. The 2007 NGDC bathymetry and the baseline

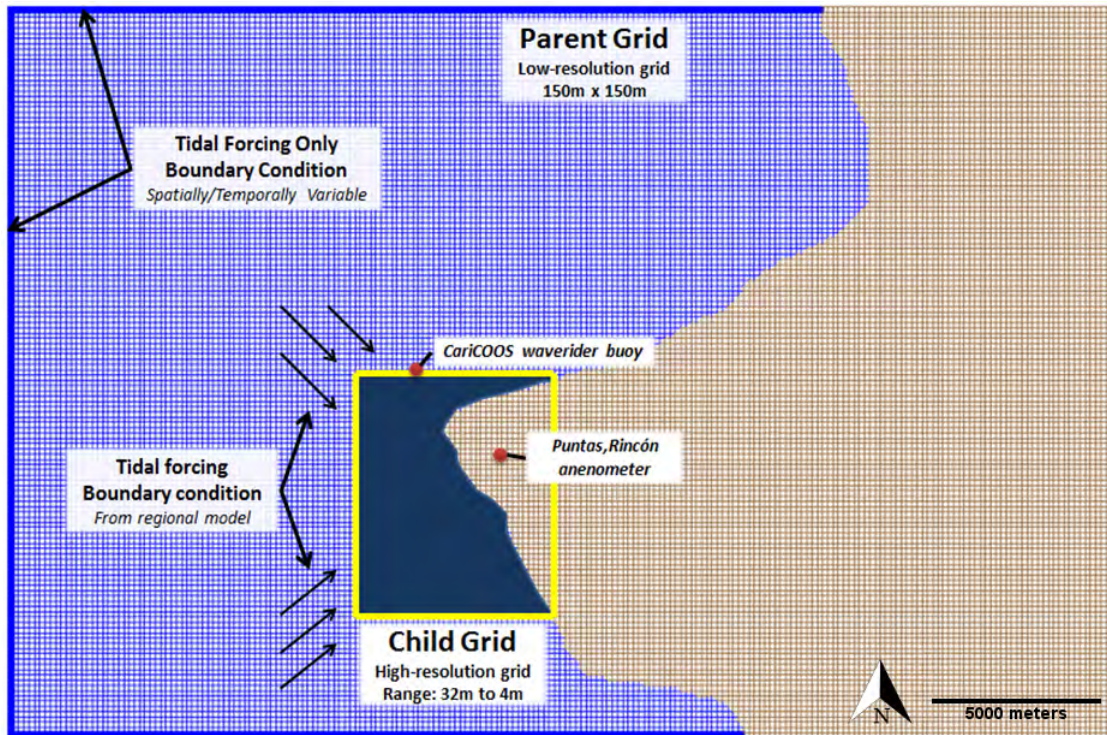


**Figure 4.8:** CMS-Flow parent grid with a total of 29,329 cells of 150 m x 150 m. The resultant tidal forcing from the parent grid is used as input tidal forcing for the high-resolution child grid (modified from Chardón, 2013).

bathymetry obtained from the jetski-based surveying system were merged in order to define the continuous grid bathymetry for the simulations and computational domain.

#### 4.3.1 CMS-Flow set-up

For the CMS numerical model, a nested approach with tidal boundary conditions was applied, since it is difficult to obtain good results of tidal flows and tidal elevation in grids with a small spatial extent (Sánchez et al., 2012). The nested approach minimizes the computational time and maximizes wave modeling accuracy (Smith and Smith, 2002). The coarse grid (parent grid) provides tidal boundary conditions to a finer grid (child grid) with higher resolution. A sketch of the nested grid is shown in Figure 4.8. The rectangular parent grid domain extends approximately 31 km x 21 km with a cell size of 150 m x 150 m directed north (zero degrees), for a total of 29,329 active cells. Figure 4.9 displays the high-resolution CMS-Flow domain which extends ap-

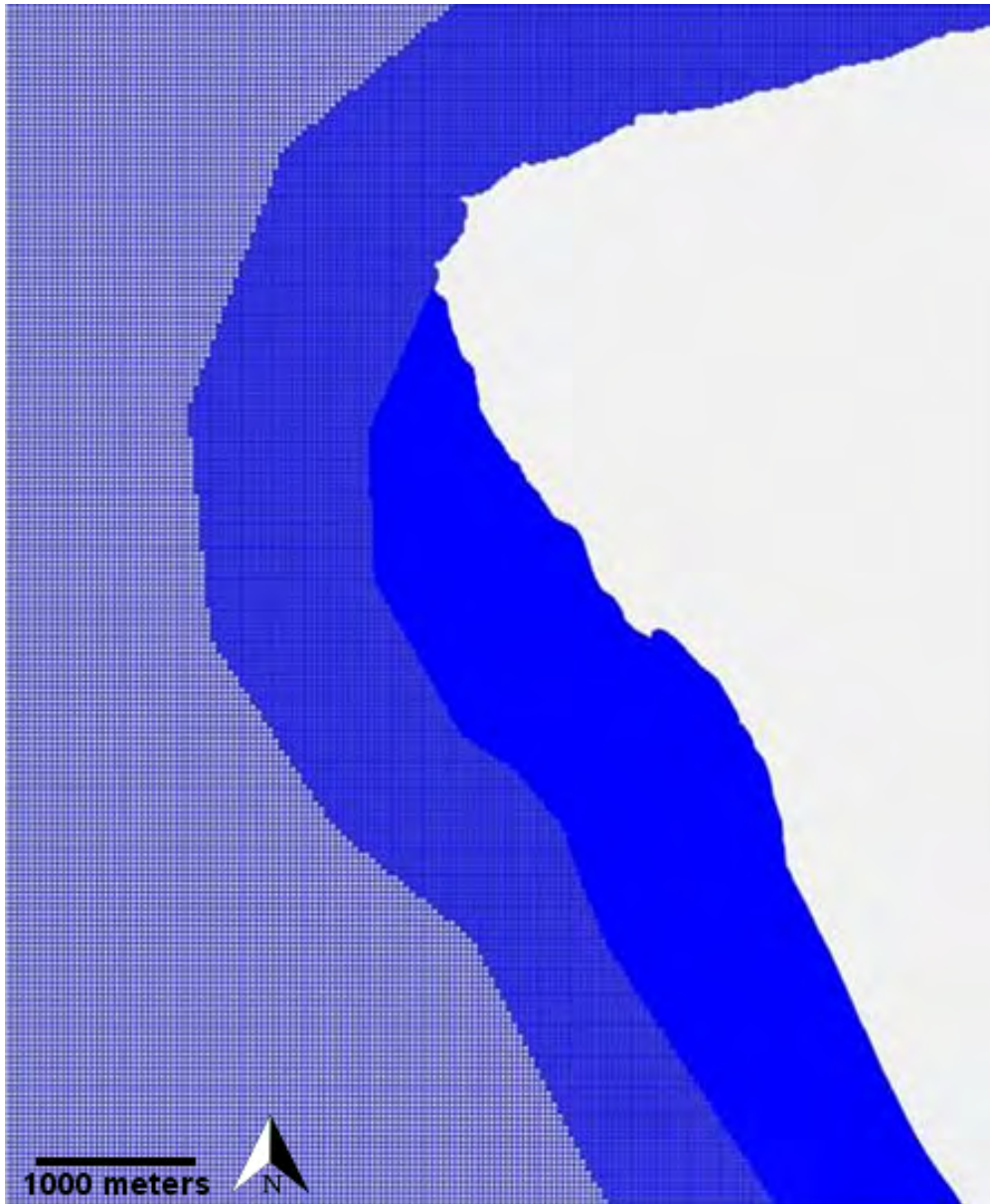


**Figure 4.9:** Telescoping grid for the CMS-Flow model. The grid has a spatial resolution ranging from 32 m offshore to a maximum of 4 m in the nearshore region. This allows the model to resolve very high-resolution circulation features in the nearshore region, while optimizing computational effort by reducing grid cells in areas in which very high spatial resolution is not necessary, such as in the open ocean (modified from Chardón, 2013).

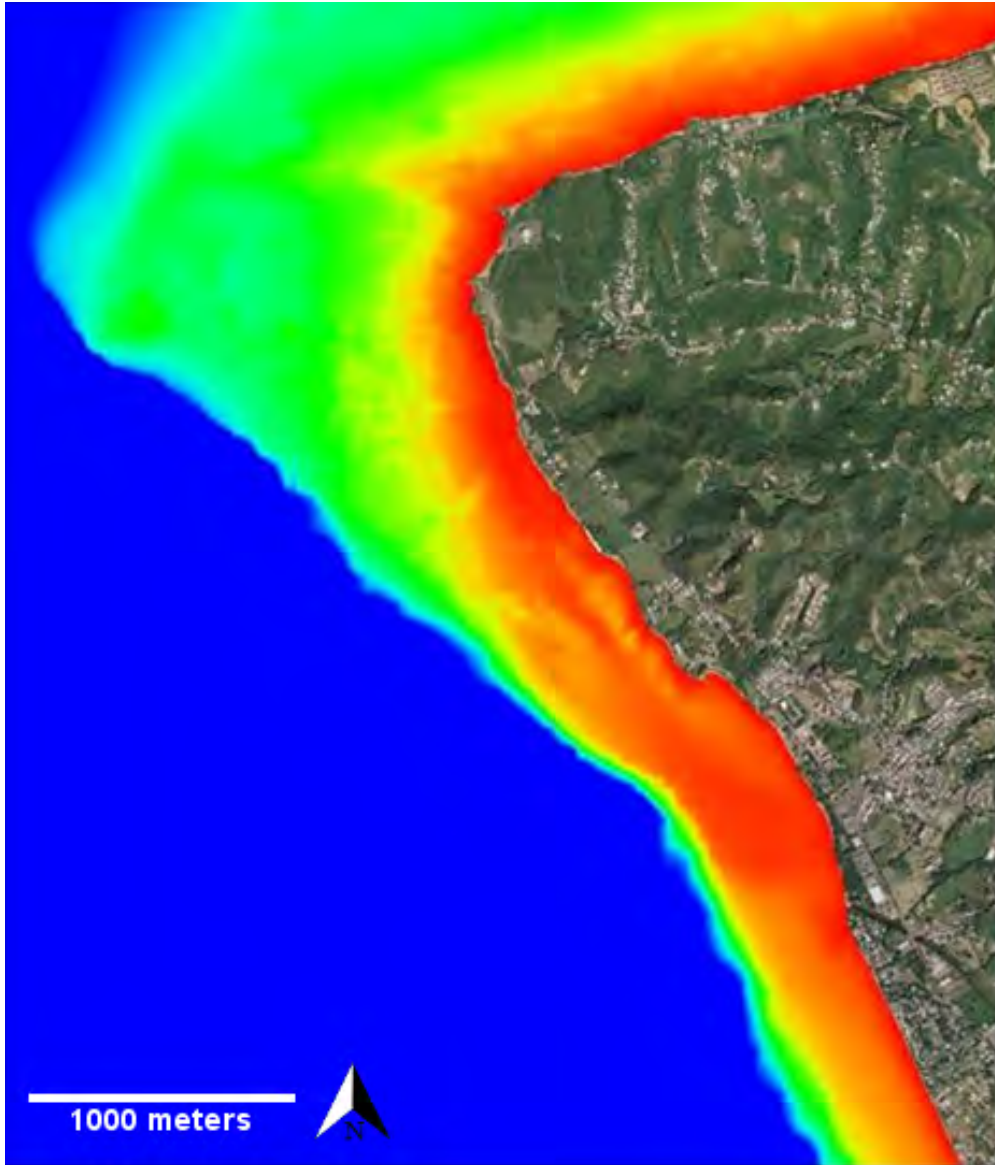


**Figure 4.10:** Merged bathymetry used by the CMS numerical model composed of the 2007 NGDC DEM bathymetry and the jetski-based high-resolution bathymetric survey from May, 23<sup>th</sup> 2014 (modified from Chardón, 2013).

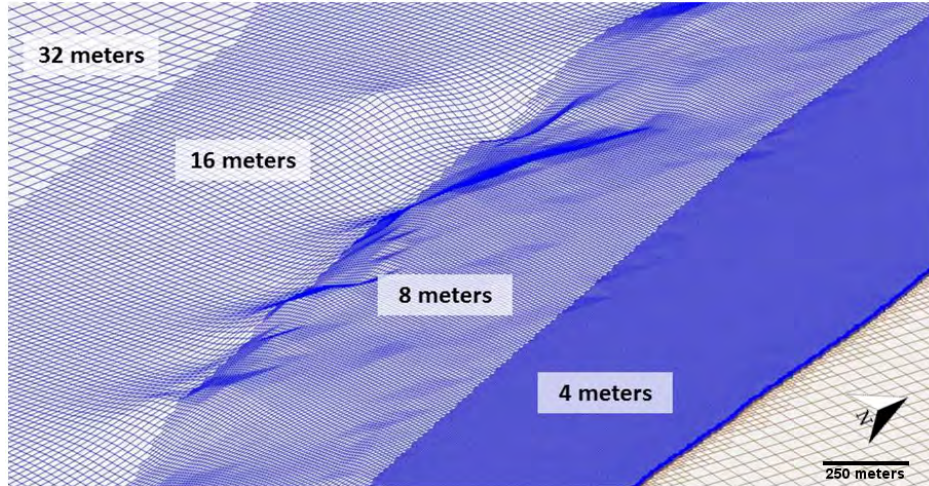


**Figure 4.11:** CMS-Flow telescoping grid ranging from 32 m to 4 m spatial resolution. The resultant tidal forcing from the parent grid is used as input tidal forcing for the high-resolution child grid (modified from Chardón, 2013).

proximately 6.8 km alongshore and 4.0 km offshore for a total of 265,391 active cells. Figure 4.10 shows the merged bathymetry used as baseline for the numerical model. This child grid is the main grid for modeling the effects of sand mining Bajo Blanco and consists of a telescoping grid with minimum and maximum spatial resolution of 32 m offshore and 4 m nearshore, respectively, as seen in Figure 4.11. The origin, corresponding to the local grid  $x$  and  $y$  axis triads, is located at the lower left corner of the domain. In addition to offshore tidal forcing, wind and wave parameters were included in the high-resolution model, since they constitute an essential part of the driving forces controlling coastal processes of the Rincón coastal system.

### ***Bed friction coefficient***

The bottom roughness specified for the CMS numerical model was the Manning coefficient,  $n$ , with a constant value of 0.025. This roughness coefficient is implemented in the model through the combined wave-current mean bed shear stress,  $\tau_{bi}$ , using the following equation (Sánchez et al., 2012):

$$\tau_{bi} = \rho m_b \lambda_{wc} c_b U U_i \quad (4.16)$$

where  $c_b$  is the bed friction coefficient;  $m_b$  is the bed slope coefficient;  $\lambda_{wc}$  is the nonlinear bottom friction enhancement factor; and  $U$  is the current magnitude. The bed friction coefficient and Manning's roughness coefficient are related by:

$$c_b = gn^2 d^{-1/3}. \quad (4.17)$$

Recent CMS numerical models have the capability of allowing an heterogeneous seabed with spatially variable bed roughness to improve energy dissipation processes. However for the present study, the CMS version used only allowed for a spatially and temporally constant bottom friction to study the effects of sand mining Bajo Blanco.

### ***Tidal boundary condition***

The parent grid boundary conditions are spatially and temporally variable offshore tidal forces extracted from the ESR-TMD. The ESR, alongside the Oregon State University (OSU), provides a MATLAB software package to access the tidal harmonic constituents and make predictions of tide height and currents (Padman, 2005). WSE conditions were used as input data for the north, west and south boundaries for eight tidal constituents: P1, O1, Q1, K1, K2, N2, S2, and M2. Table 4.1 presents the constituents with their proper description. The tidal amplitude results from the numerical model served as tidal forcing boundary condition for the child grid shown in Figure 4.8.

### ***Wind forcing***

The wind forcing time-series was extracted from the CariCOOS Rincón anemometer, station PTRP4, located in Barrio Puntas at a height of 15 m above land elevation. The CMS model automatically adjusts the wind speed to the 10 m height, where most near-surface ocean wind measurements are referenced. The wind magnitude and direction is assumed to be spatially constant, but variable in time.

**Table 4.1:** Primary tidal harmonic constituents for Mayagüez, Puerto Rico with their respective amplitude, phase and phase speed (NDBC, 2016).

Constituent	Amplitude	Phase	Speed	Description
	<i>m</i>	<i>deg</i>	<i>deg/hr</i>	
<b>P1</b>	0.018	157.70	14.96	Solar diurnal
<b>O1</b>	0.047	155.00	13.94	Lunar diurnal
<b>Q1</b>	0.009	140.70	13.40	Larger lunar elliptic diurnal
<b>K1</b>	0.059	153.50	15.04	Lunar diurnal
<b>K2</b>	0.006	279.10	30.08	Lunisolar semidiurnal
<b>N2</b>	0.035	236.90	28.44	Larger lunar elliptic semidiurnal
<b>S2</b>	0.022	281.00	30.00	Principal solar semidiurnal
<b>M2</b>	0.145	258.50	28.98	Principal lunar semidiurnal

### *Sediment model set-up*

Table 4.2 provides the sediment transport parameters available in CMS-Flow. Chardón (2013) used these same parameters to study the morphology change along the coast of Rincón as a result of Hurricane Sandy and Tropical Storm Isaac. Most of the parameters were assigned default values with a sediment density of  $2650 \text{ kg/m}^3$  and average mean grain size of 0.25 mm, according to the sand shoal sieve analysis presented in the previous chapter.

The sediment transport formula used for the numerical model was the Lund-Cirp formulation (Carmenen and Larson, 2007), which computes bed and suspended load under combined waves and currents using the following formula:

$$\frac{q_b}{\sqrt{(s-1)gM^3}} = a_c \sqrt{\theta_c} \theta_{cw,m} \exp\left(-b_c \frac{\theta_{cr}}{\theta_{cw}}\right) \quad (4.18)$$

where  $q_b$  is in  $m^2/s$ ,  $M$  is the mean grain size,  $s$  is the sediment specific gravity or relative density,  $g$  is gravitational constant,  $\theta_{cw,m}$  and  $\theta_{cw}$  are the mean and maximum Shields parameters due to waves and currents respectively,  $\theta_c$ ,  $\theta_{cr}$  is the critical Shields parameter due to currents and  $a_c$  and  $b_c$  are empirical coefficients (Sánchez et al., 2012). For more information regarding the sediment model parameters please refer to the CMS Manual 2012.

**Table 4.2:** Sediment transport model set-up parameters for the CMS Flow numerical model.

Sediment transport parameters		
Formulation	Advection-Diffusion	
Sediment transport formula	Lund-CIRP	
Total load adaptation length method	Constant	
Sediment density	2650	kg m-3
Transport grain size, d50	0.25	mm
Total load adaptation length	10.0	m
Bed load scaling factor	1.0	default
Suspended load scaling factor	1.0	default
Morphologic acceleration factor	1.0	default
Bed slope coefficient	1.0	default
Sediment porosity	0.4	default

#### 4.4 CMS validation results

The CMS-Wave and current model results for the WFS half-plane directional spectra were compared with wave parameters from the AWAC and north-south ( $V_y$ ) current component from the ADCP located at the study area (see Figure 4.3). The top illustration in Figure 4.12 displays the time series comparison between the observed (black) and the model-predicted (blue) significant wave height, while the lower illustration provides the wave period comparison. The numerical model produced an excellent approximation of the observed results during the two-month time span, which would allow the model to properly predict the wave climate response associated with sand mining at the Bajo Blanco sand shoal. Figure 4.13 displays the north-south current velocity and the WSE output comparison with the ADCP observed data and the Mayagüez mareograph base station, respectively. WSE prediction results were extracted from the ADCP location, 12 km apart from the Mayagüez mareograph position. However, comparison between both datasets demonstrated acceptable agreement with maximum WSE difference of less than 10 cm. The correlation analysis presented in Figure 4.14 reveals a strong uphill linear relationship between both datasets, resulting in reliable outputs from the CMS model.

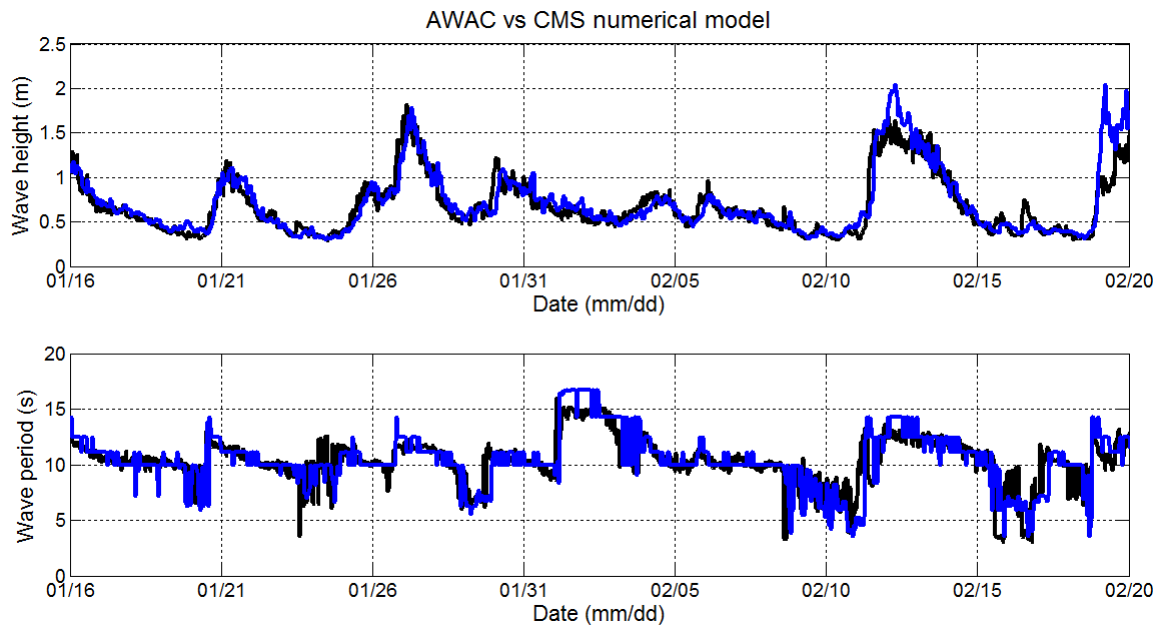


**Figure 4.12:** Comparison results between the simulated (blue) wave height and wave period vs observed data at the AWAC sensor (black). The model provided an excellent estimation of the wave height and wave period during the winter swells of January and February of 2013.

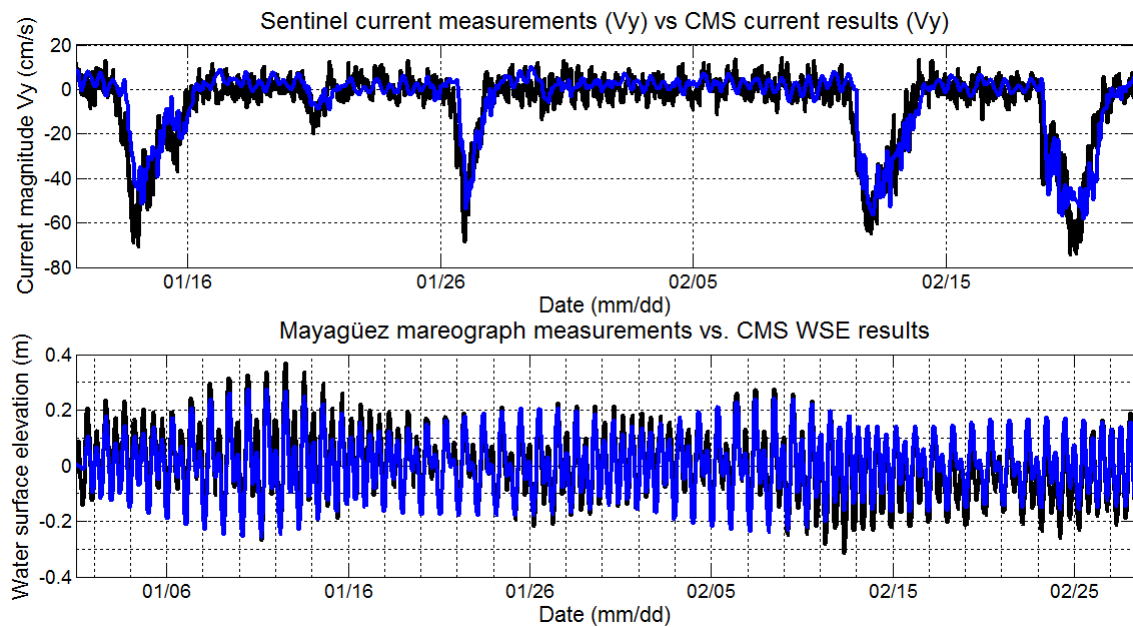


**Figure 4.13:** Comparison between the numerical simulation results (blue) and field observations (black) of the north-south velocity component ( $V_y$ ) and water surface elevation at the Sentinel ADCP and the Mayagüez mareograph, respectively.

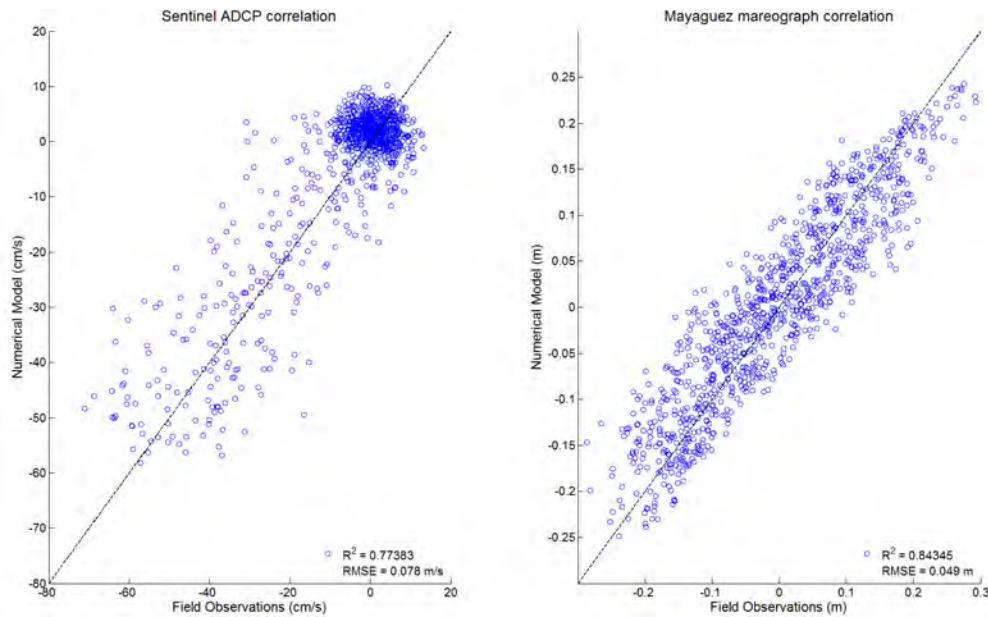


**Figure 4.14:** Illustration of the linear correlation results for the north-south current magnitude and the water surface elevation extracted from the coupled CMS numerical model at the Sentinel ADCP and Mayagüez mareograph, respectively.

#### 4.5 Concluding remarks

This chapter discussed the application of the CMS numerical model and the adjustments made to improve the performance of the wave model by considering different descriptions of directional wave spectra. Chardón (2013) previously investigated the morphology change at a stretch of the coast of Rincón using the coupled CMS numerical model. The spectral wave input for the model used an empirical JONSWAP spectrum which resulted in a correlation of 84%, less accurate than the WFS (89%) results presented in this study. Using this validated numerical model, the next chapter discusses the response of the wave climate and nearshore hydrodynamics to mining of the Bajo Blanco sand shoal under the 2013 winter swell conditions.

## **Chapter 5**

# **EFFECT OF SAND MINING ON NEARSHORE WAVE CLIMATE**

The extraction of sand from a borrow site can affect the nearshore wave climate and wave-induced hydrodynamics of the nearshore region. The sudden change in depth caused by dredging can force waves to diverge over the dredge area towards shallower waters due to wave refraction, potentially redistributing the wave energy flux shoreward of the borrow site. Wave energy fluxes drive nearshore currents, which are associated with sediment transport (Kelley et al., 2001). These wave-induced currents can have a strong effect on alongshore and cross-shore sediment transport processes that determine erosion or accretion patterns (Hammer et al., 2004).

The coast of Rincón is highly active during the winter season, with breaking waves of up to 7 m at Marías and Tres Palmas beaches, among others. The shallow depths of the Bajo Blanco sand shoal lead to moderate wave breaking during large swells, dissipating a moderate fraction of the wave energy before it reaches eroded beaches such as Rincón's Public beach and Villa Cofresí. The sand shoal may also serve as a sediment source to replenish beaches that have been eroded by incoming high energy wave events from the southwest (Chardón, 2013). Using the coupled CMS numerical model, this study aims to evaluate the wave climate response, in the form of the wave energy flux, produced by two dredging scenarios at the Bajo Blanco sand shoal. Wave energy flux not only considers wave height, but takes into account wave period, wavelength, and wave energy density to determine the wave power available to generate currents and transport sediment in the nearshore environment.

In this chapter, the CMS numerical model results for wave energy flux, wave-induced currents and morphology change under existing and post-dredging scenarios are compared. Similar evaluation methods have been performed by the US Army Corps of Engineers using different modules from the Surface Modeling System (Kelley et al. (2001), Hammer et al. (2004)). The aim of the current study is to improve our understanding of the potential consequences that dredging the Bajo Blanco sand shoal could have on coastal processes along the coast of Rincón and its eroding beaches.

## 5.1 Case studies

Two dredging configurations were considered as possible options for mining Bajo Blanco: a single excavation area, and multiple excavation areas. Salas (2014) calculated an equilibrium beach profile for a stretch of beach along the coast of Rincón. If Salas (2014)'s equilibrium profile calculations are extended from the Rincón Marina to Córcega beach, and assuming an overfill factor of 1.60 (average value at Bajo Blanco), a total excavation volume of approximately  $1,081,177 \text{ m}^3$  would be needed to nourish the coast with a berm length of 35 m.

Again, there is considerable variability of the overfill factor depending on which sand shoal samples are considered (between 50-70 percent of additional volume sand). Using this preliminary volume estimate on the order of  $1 \times 10^6 \text{ m}^3$ , two dredging configurations were designed. Figure 5.1 and 5.2 show a three-dimensional view for Case 1 (single excavation) and Case 2 (two excavations areas), respectively. The shape of both configurations were designed taking into account the compatibility results from the alternative computation method of Dean's overfill ratio. As previously mentioned, the shoreward side of Bajo Blanco presented coarser and more suitable sediment grain sizes in comparison with the rest of the sand shoal, since coarser sand requires more energy for suspension and is therefore more resistant against wave impacts (Dean and Dalrymple, 2004).

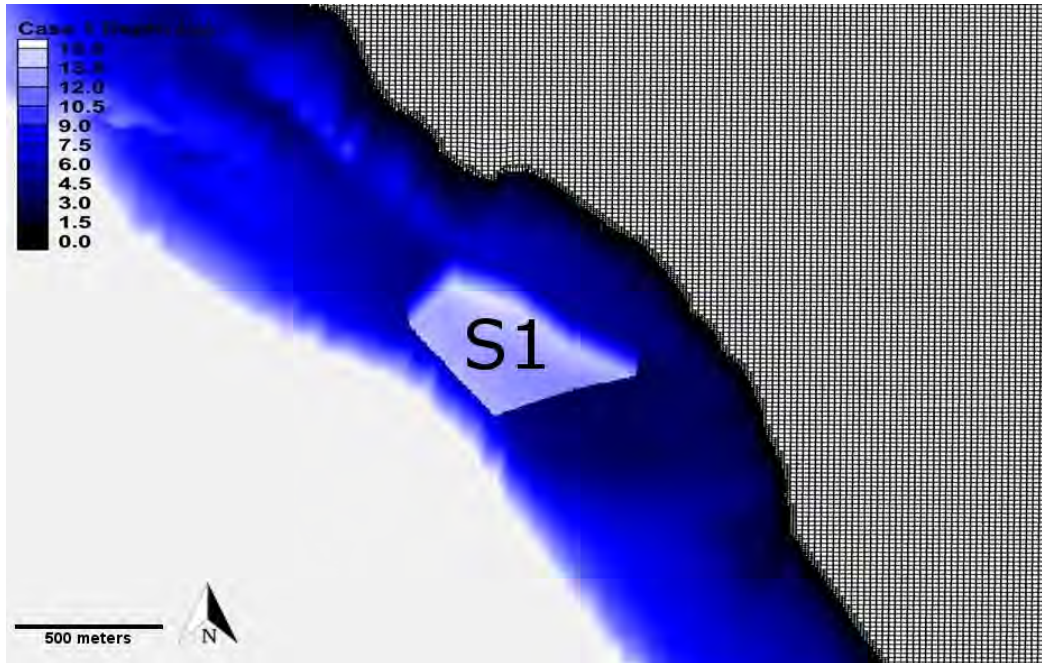


**Figure 5.1:** The single dredge area (S1) scenario has an extraction area of  $144,000 \text{ m}^2$  with a dredge depth of 7 m. The total volume extracted for this case is  $1,010,000 \text{ m}^3$ .

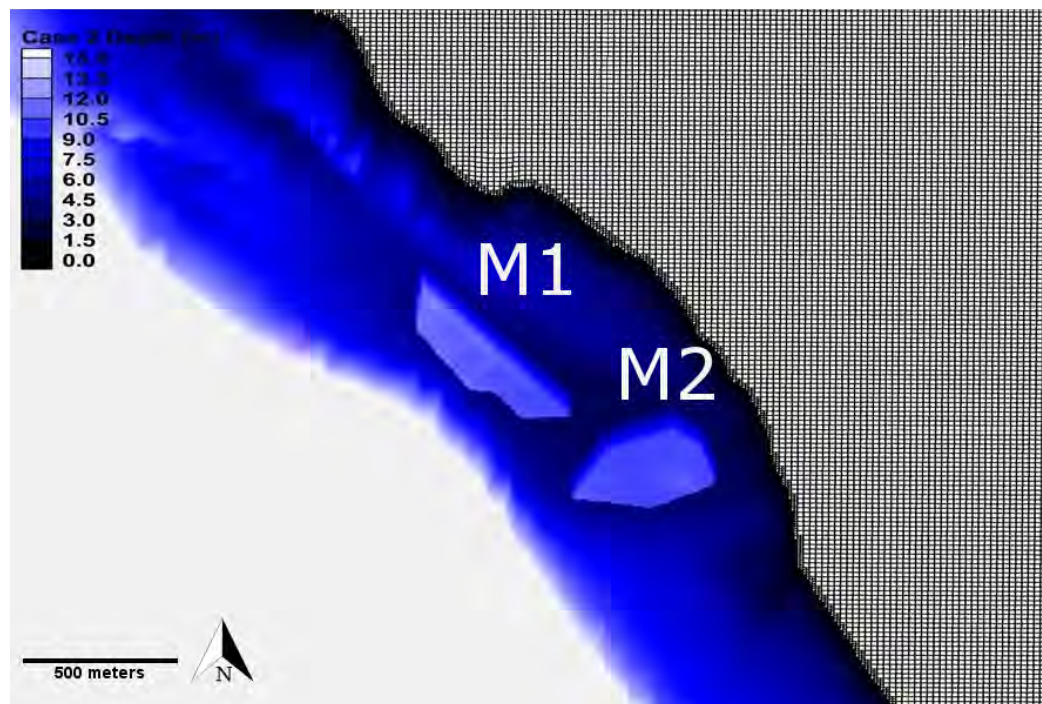


**Figure 5.2:** Multiple dredge areas scenario, M1 and M2, with a total area of  $121,000 \text{ m}^2$  and dredge depth of 9 m each. The total volume extracted for this case is  $1,080,000 \text{ m}^3$ .

**Table 5.1:** Geometric characteristics of potential borrow site areas.

Resource Area	Borrow Site Surface Area ( $\times 10^5 m^2$ )	Maximum Excavation Depth (m)	Borrow Site Sand Volume ( $\times 10^5 m^3$ )
S1	1.44	7	10.1
M1	0.56	9	5.0
M2	0.65	9	5.8

The sediment properties of the native beach and borrow sites were discussed in section 3.2.1. The total excavation volume, surface area, and mean depths for each case are shown in Table 5.1. It is important to mention that the bathymetry for each case was not modified to include the new beach profile as a result of the beach nourishment. This approximation should not significantly affect the results since the large-scale wave climate response patterns cause by sand mining will not be affected by the added volume. However, the magnitude of these changes may increase or decrease slightly very close to shore depending on the extent of the beach nourishment design.

Both cases are located approximately 300 m from the shoreline, at an average depth of 5 m. The dredging areas were designed with a side slope of 3H:1V, although these slopes are expected to evolve naturally into a stable slope shortly after excavation.

## 5.2 Grid development

To accurately predict the wave climate response of sand mining the Bajo Blanco sand shoal, the coupled CMS numerical model (CMS-Wave spectral model and CMS-Flow circulation model) was used with the high resolution grids developed for the validation of the model discussed in the previous chapter (see Figure 4.2 and 4.10). Runs using the existing and post-dredging bathymetry features were modeled for the winter wave climate conditions during the validation period between January and February 2013. The CMS-Wave model grid consists of variable rectangular cells ranging from larger cells of 16 m x 16 m in the offshore to smaller cells of 4 m x 4 m in the

nearshore and sand shoal area. The CMS-Flow model grid uses a telescoping grid with a minimum and maximum spatial resolution of 32 m offshore and 4 m very nearshore, respectively.

As discussed in the previous chapter, a two-way coupling process is used by the CMS in order to exchange information between both models. The spatial extent of the grids was chosen based on the location of the CariCOOS Waverider buoy. Tidal boundary conditions were obtained from nesting the child grid within a coarser CMS-Flow model with tidal forcing boundary conditions from the TMD (see Figure 4.8). Wind surface boundary conditions were assumed to be spatially constant but temporally variable, using time series of wind velocity collected by the CariCOOS anemometer located in Rincón.

### 5.3 Model results

This section evaluates the wave climate response after dredging the Bajo Blanco sand shoal. A redistribution of wave energy and alteration of wave directions as a result of the sand extraction is expected. For both dredging scenarios, results for wave energy flux response and its effect on ocean currents and morphological change are presented in the upcoming sections. The wave energy flux,  $P$ , is given by

$$P = EC_g. \quad (5.1)$$

The parameter  $E$  is the energy density per unit area ( $J/m^2$ ), and can be calculated as follows:

$$E = \frac{1}{16}\rho g H^2 \quad (5.2)$$

where  $H$  is the significant wave height,  $\rho$  is the seawater density and  $g$  is the gravitational acceleration (Dean and Dalrymple, 2004). This energy is transported at the group velocity,  $C_g$ , which is a function of the wavenumber  $k = 2\pi/L$ , where  $L$  is the wavelength, and the water depth is  $d$ . This group velocity can be estimated using the linear wave dispersion relation:

$$\omega^2 = gk \tanh(kd) \quad (5.3)$$

where  $\omega = 2\pi/T$  and  $T$  is the wave period. Rearranging equation 5.3, the wave celerity  $C = \omega/k$  (phase speed) can be obtained as follows:

$$C = \frac{g}{\omega} \tanh(kd). \quad (5.4)$$

The group speed is related to the phase speed using the following formula:

$$C_g = \frac{1}{2} C \left( 1 + \frac{kd}{\sinh(kd)} \right). \quad (5.5)$$

Knowing the wave energy density and group speed of the wave field, the wave energy flux can be obtained for the existing bathymetric conditions at Rincón. Results for the average and cumulative wave energy flux were calculated for the months of January and February 2013 using the hourly (instantaneous) output results of the CMS numerical model. The cumulative wave energy flux was obtained by integrating the wave energy flux results over the simulation period. With these values, the present study discusses the wave energy flux response caused by mining the Bajo Blanco sand shoal and how these changes may affect the nearshore morphology and current patterns at the study site.

### 5.3.1 Effects on wave climate

Model results for the existing bathymetry are shown from Figures 5.3 to 5.6. The instantaneous results correspond to the peak hour (4:00 am) of the January 2<sup>nd</sup>, 2013 winter swell event, when the CariCOOS Rincón Waverider buoy registered an event with significant wave height of 3 meters coming from the northwest, with a peak period of 12.5 seconds.

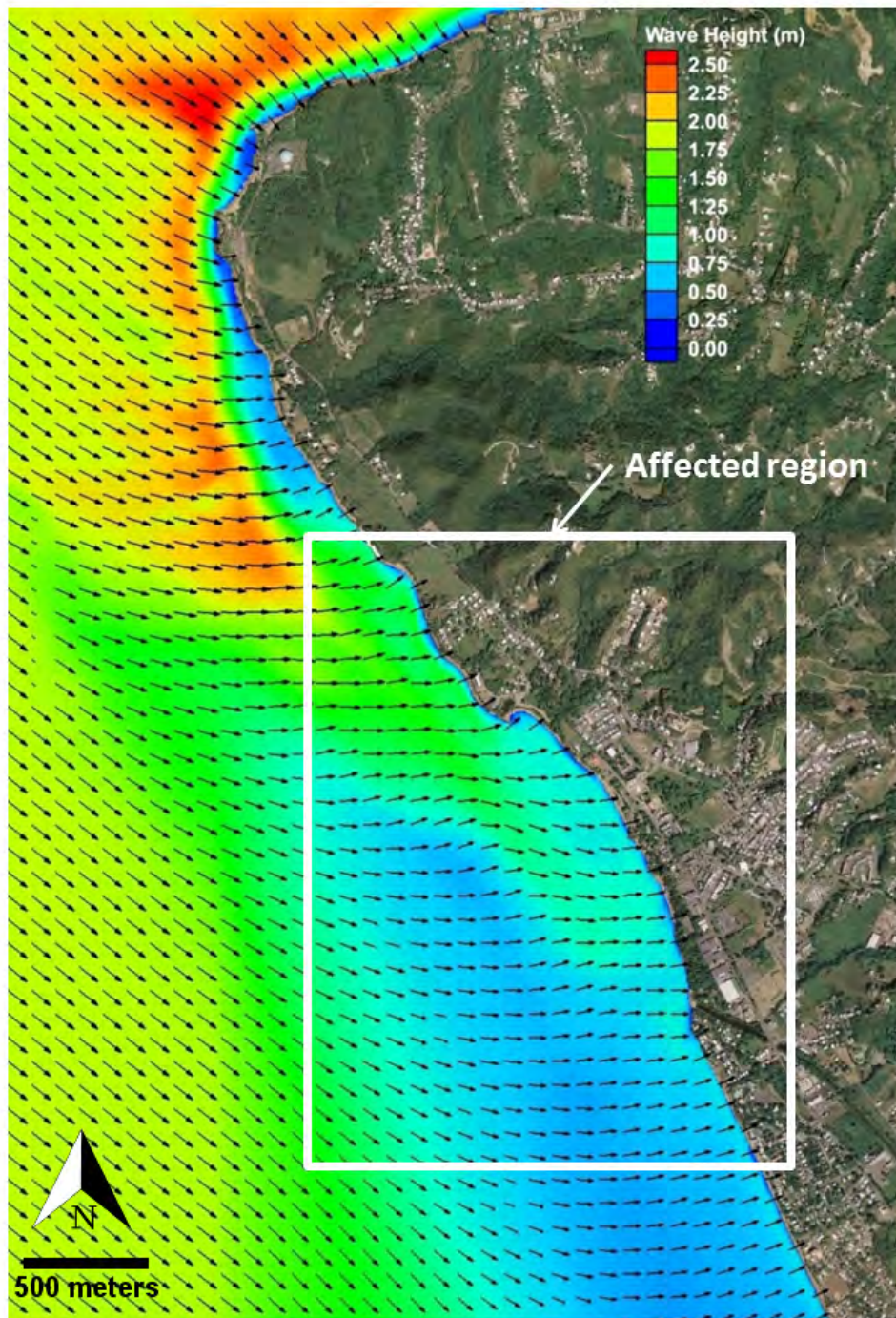


**Figure 5.3:** Pre-dredging CMS numerical model results for significant wave height during the peak hour of January 2<sup>nd</sup>, 2013. The instantaneous significant wave height (colored contours) is presented for the entire model domain, and vectors represent mean wave direction.

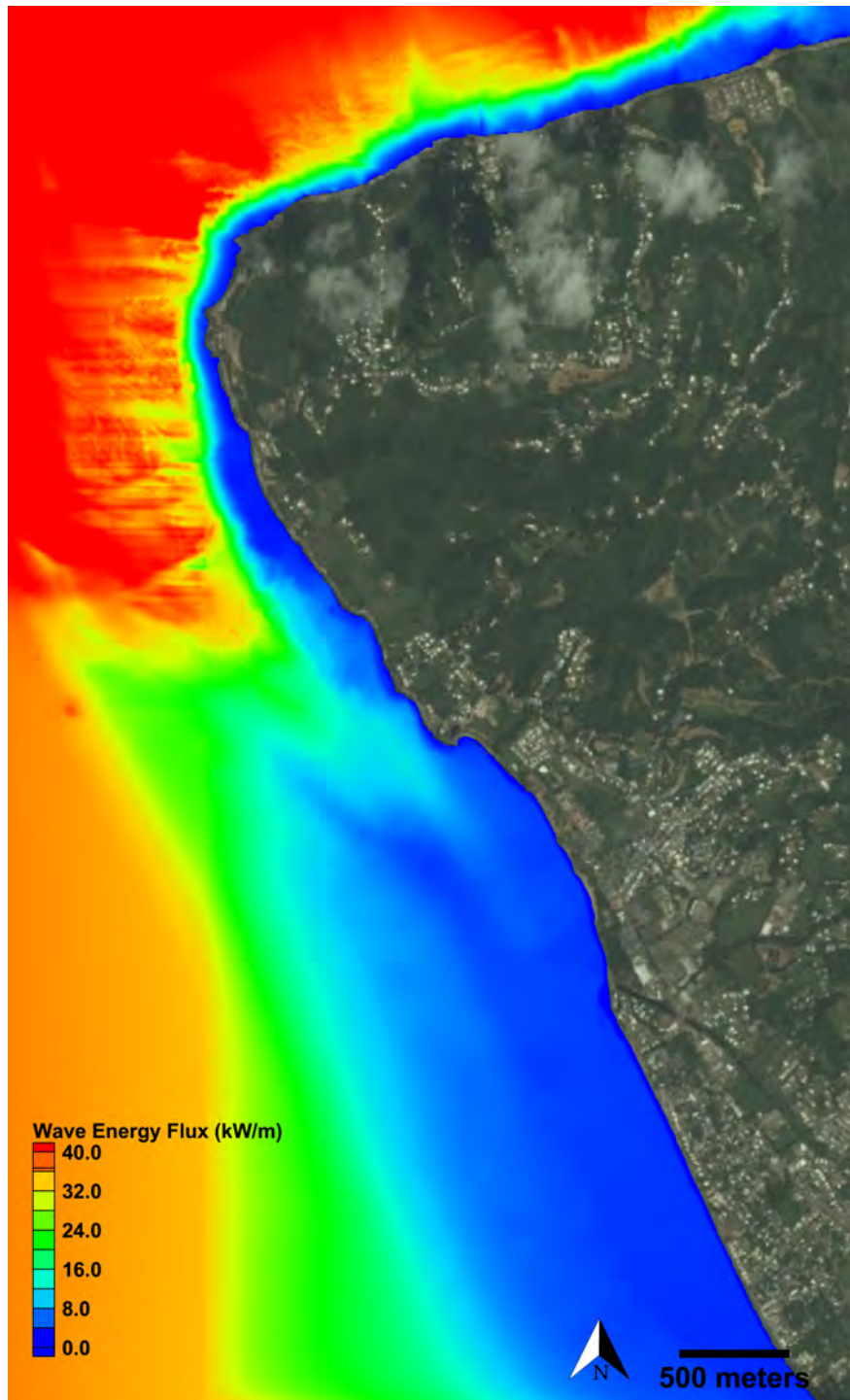


**Figure 5.4:** Pre-dredging CMS numerical model results for wave energy flux during the peak hour of January 2<sup>nd</sup>, 2013.

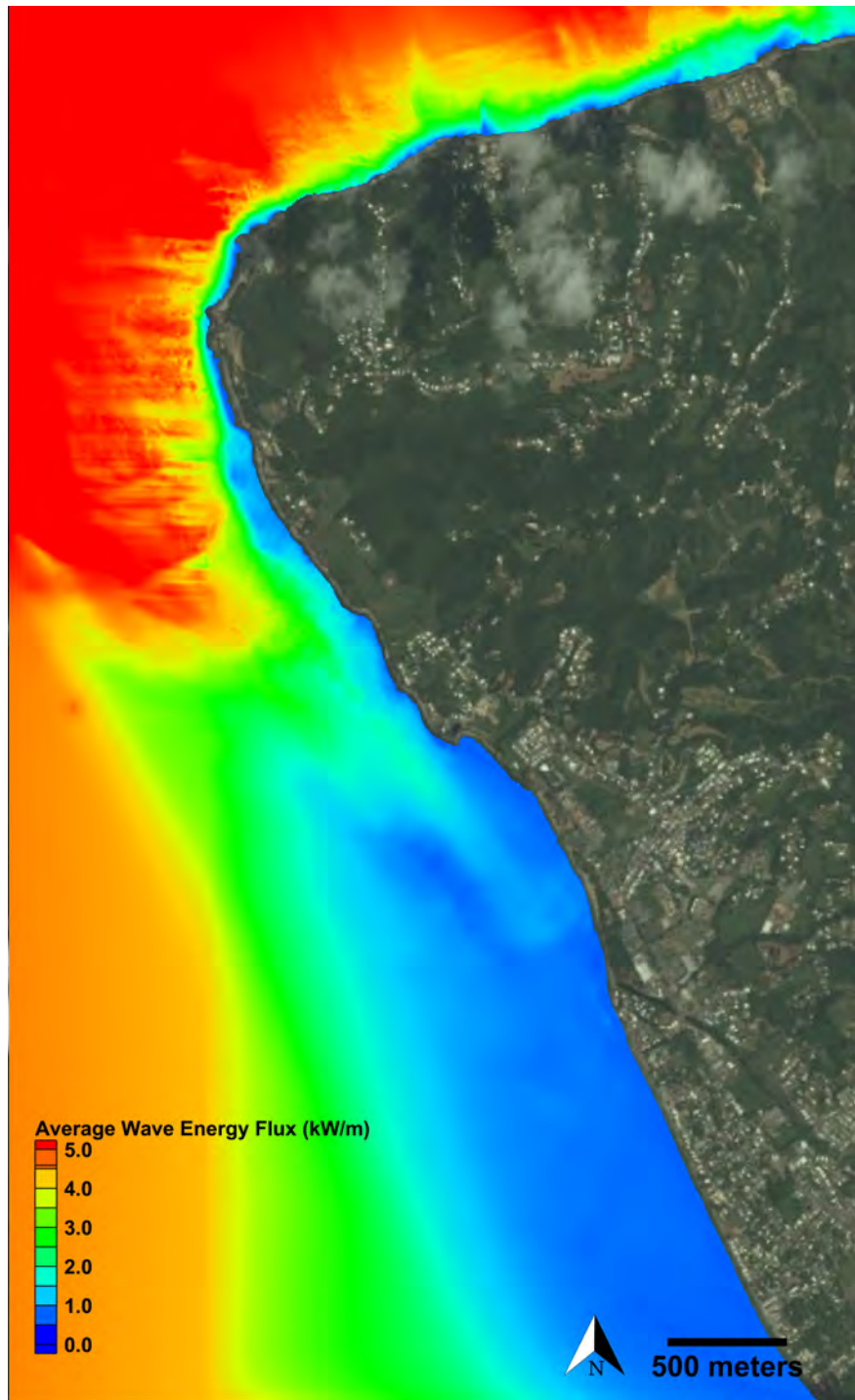


**Figure 5.5:** Pre-dredging CMS numerical model results for average wave energy flux during the two months simulation period (January - February 2013).

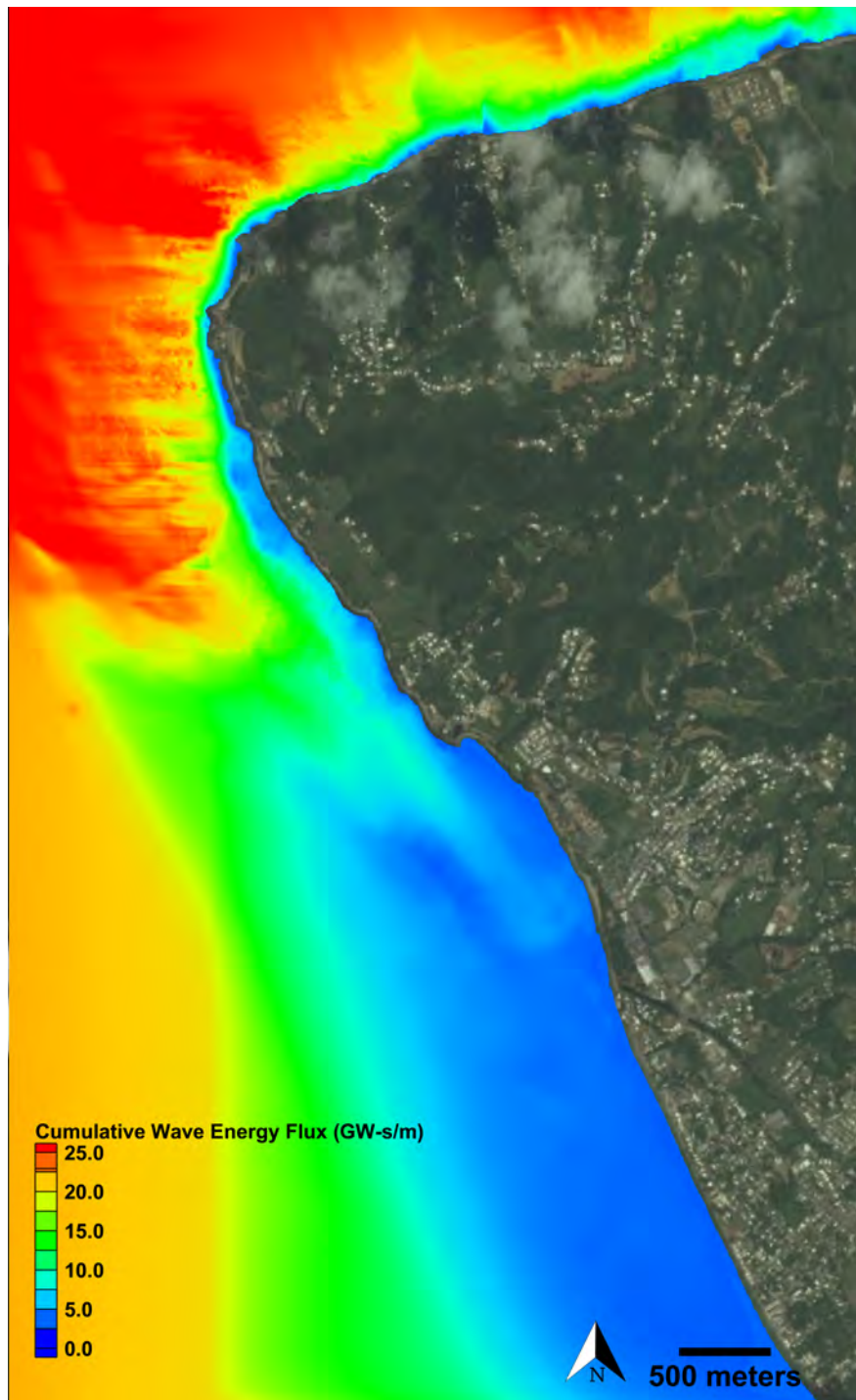


**Figure 5.6:** Pre-dredging CMS numerical model results for cumulative wave energy flux during the two months simulation period (January - February 2013)

From Figure 5.3, it can be observed how the bathymetry significantly affects the wave field as it propagates towards shore. As ocean waves approach Bajo Blanco (approximately 700 m offshore), the sudden decrease in depth due to the presence of the sand shoal causes significant shoaling, generating maximum wave height values of 1.70 m at the sand shoal, and less than a meter near the shore. Wave direction is also strongly affected by the sand shoal due to wave refraction.

Figures 5.4 to 5.6 present the instantaneous, average and cumulative wave energy flux results, respectively, for the existing bathymetric conditions. Figure 5.4 displays the wave energy flux during an instant of the simulation, with maximum values of over 40.0 kW per meter crest offshore. At the Bajo Blanco sand shoal, the average wave energy flux for the two month simulation period varies between 1.0-2.0 kW/m, with a maximum cumulative energy flux of approximately 6 GW-s/m for that time period.

### **5.3.2 Wave energy flux response**

Post-dredging CMS model results for Case 1 and Case 2 are shown from Figure 5.7 to 5.14. The wave climate response behaved similarly in both cases with an evident decrease in wave energy flux at the dredge area due to a divergence in the wave field caused by wave refraction. Incoming waves reacted to the sudden increase in depth by refracting towards the edges, or shallower areas. Consequently, a maximum decrease in cumulative wave energy flux of 3.35 GW-s/m and 3.2 GW-s/m was seen in Case 1 and Case 2, respectively. Shoreward of the extraction site, the effect was less pronounced with wave energy flux gradually decreasing towards the shore. From the results it can be seen how in both cases there is a hot spot of increase in wave energy flux of approximately 0.33 GW-s/m close to the Rincón Marina.

At the edges of the extraction site, waves converge due to refraction, leading to a maximum increase in cumulative wave energy flux of 1.02 GW-s/m and 0.64 GW-s/m for Case 1 and Case 2, respectively. However, the increase in wave energy flux caused by dredging Bajo Blanco extends as far as 2 km south of the dredge area, producing wave height increments in the magnitude of

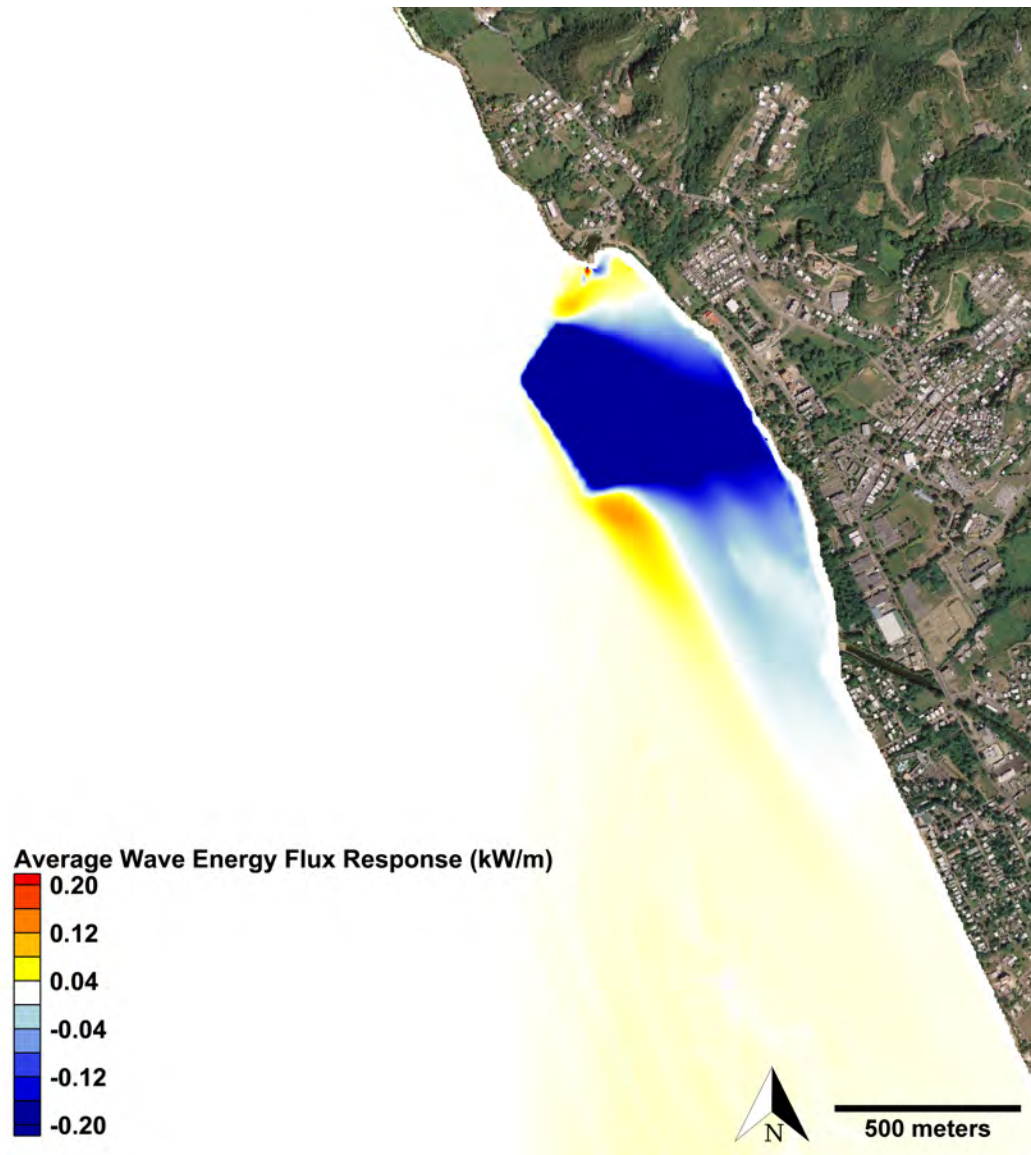


**Figure 5.7:** Post-dredging CMS numerical model average wave energy flux results for Case 1 during the two month simulation period (January - February 2013). The reddish and blueish colors represent an increase and decrease in wave energy flux, respectively.

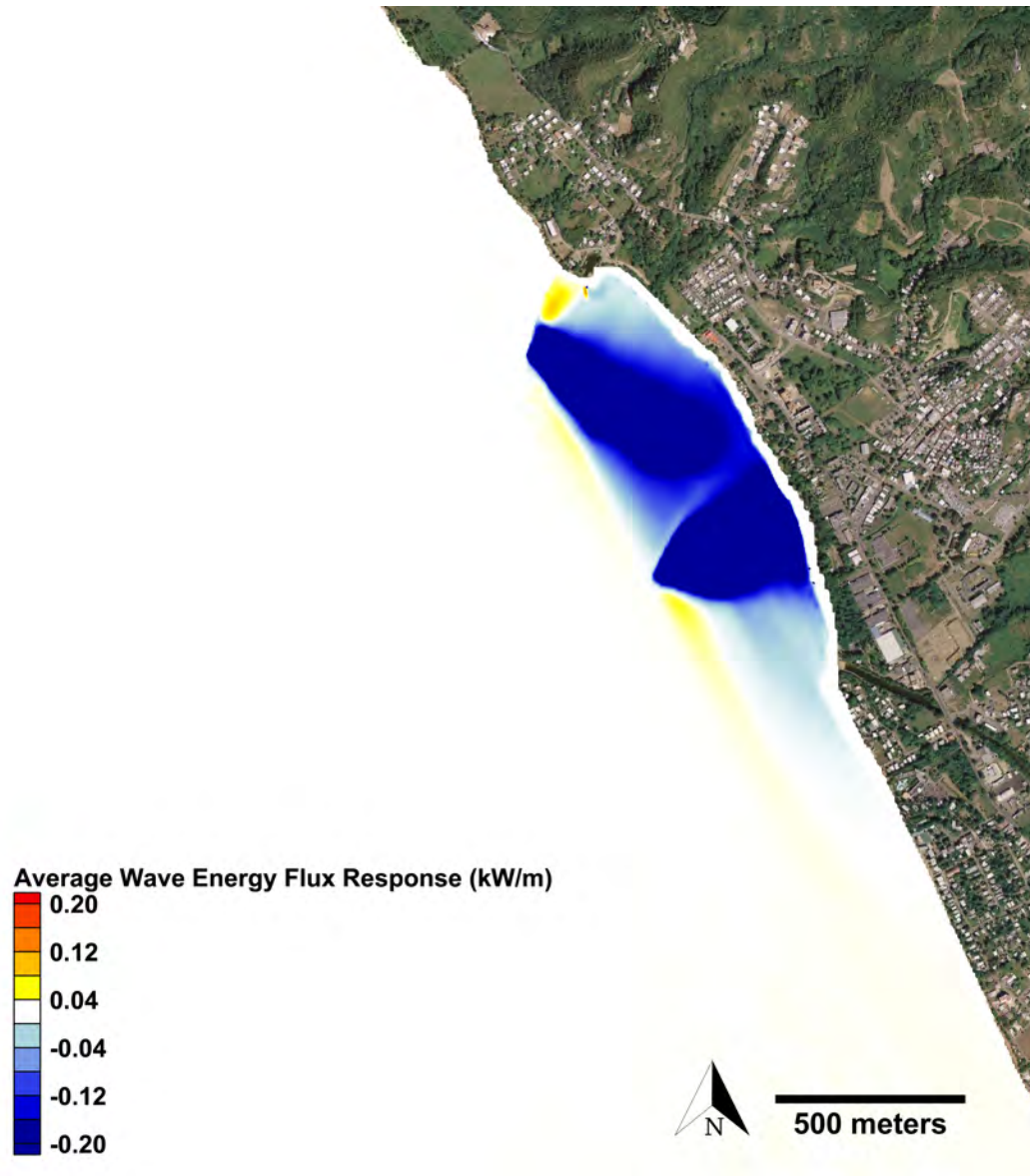


**Figure 5.8:** Post-dredging CMS numerical model average wave energy flux results for Case 2 during the two month simulation period (January - February 2013). The reddish and blueish colors represent an increase and decrease in wave energy flux, respectively.

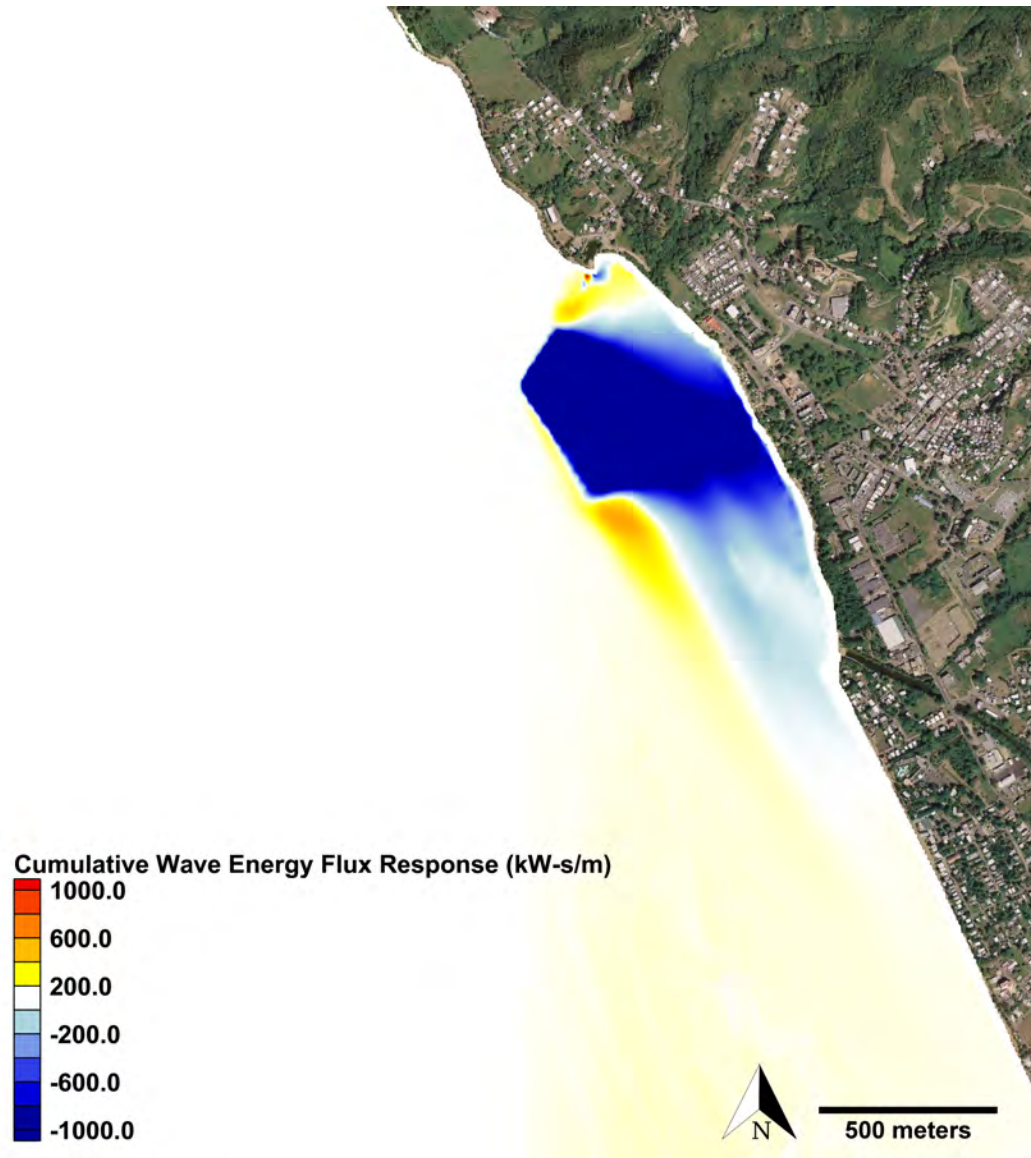


**Figure 5.9:** Post-dredging CMS numerical model cumulative wave energy flux results for Case 1 during the two month simulation period (January - February 2013). The reddish and blueish colors represent an increase and decrease in wave energy flux, respectively.

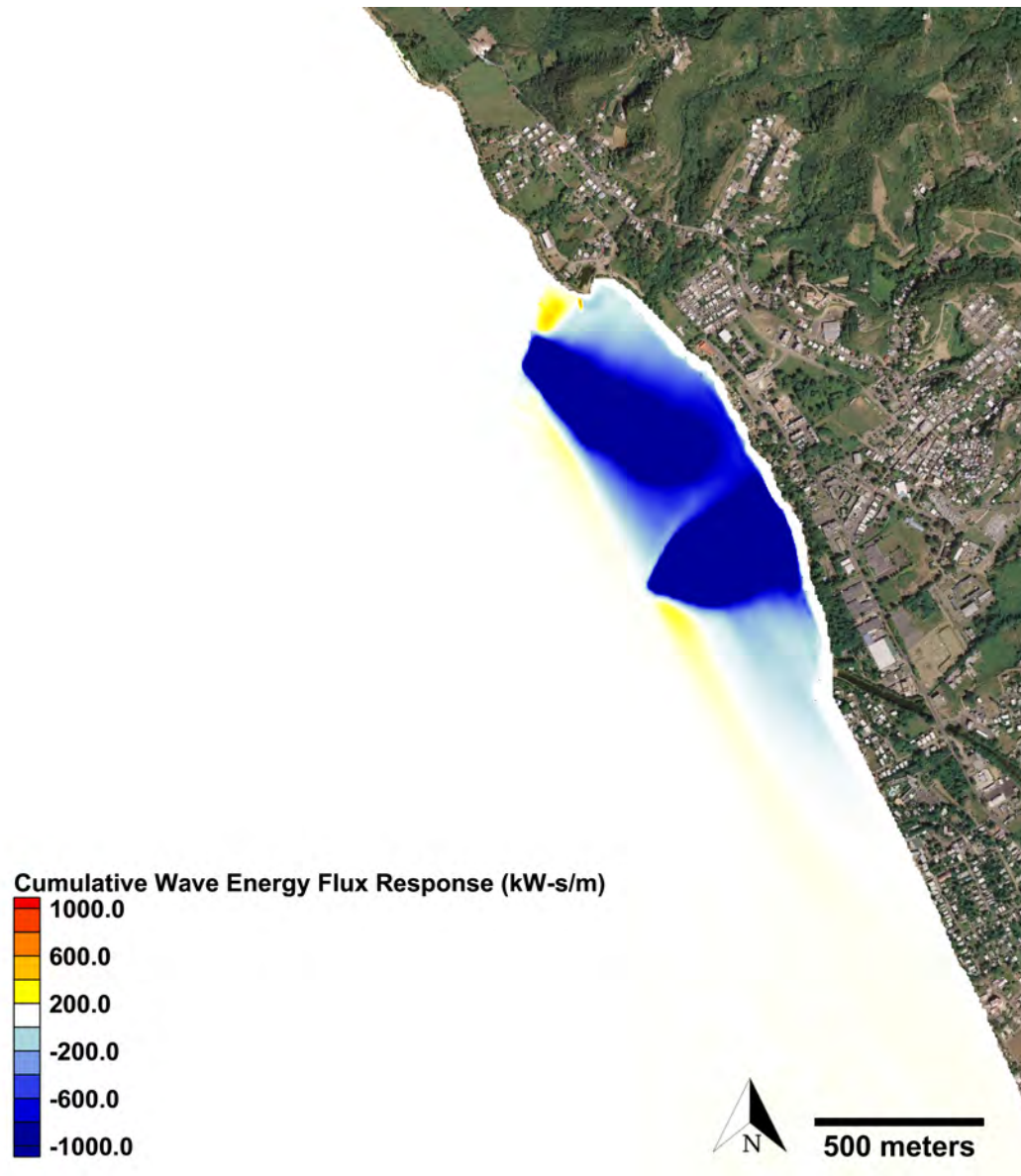


**Figure 5.10:** Post-dredging CMS numerical model cumulative wave energy flux results for Case 2 during the two month simulation period (January - February 2013). The reddish and blueish colors represent an increase and decrease in wave energy flux, respectively.

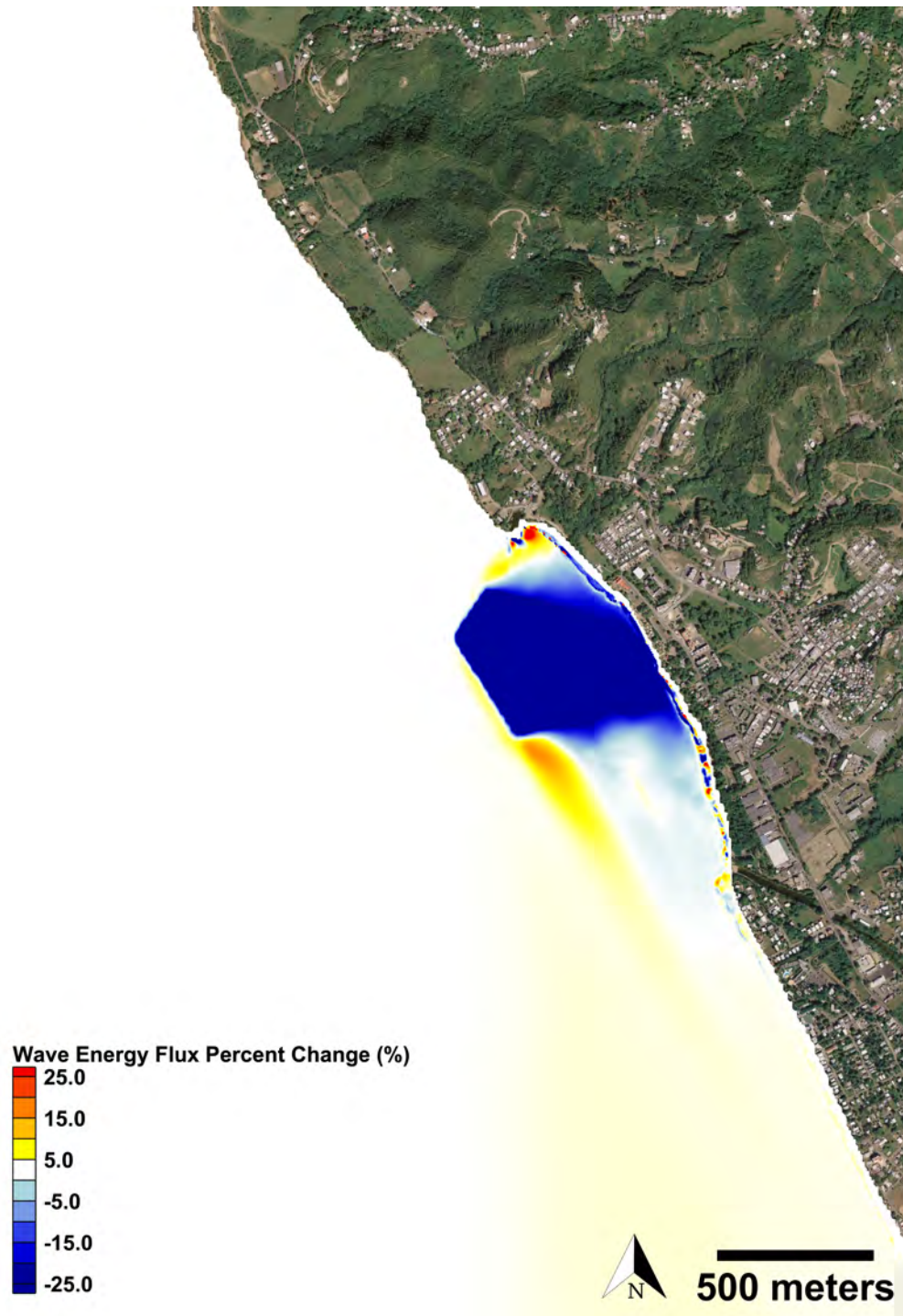


**Figure 5.11:** Wave energy flux response (percentage wise) for the peak hour of January 2<sup>nd</sup>, 2013 for Case 1. The reddish and blueish colors represent an increase and decrease in wave energy flux, respectively.

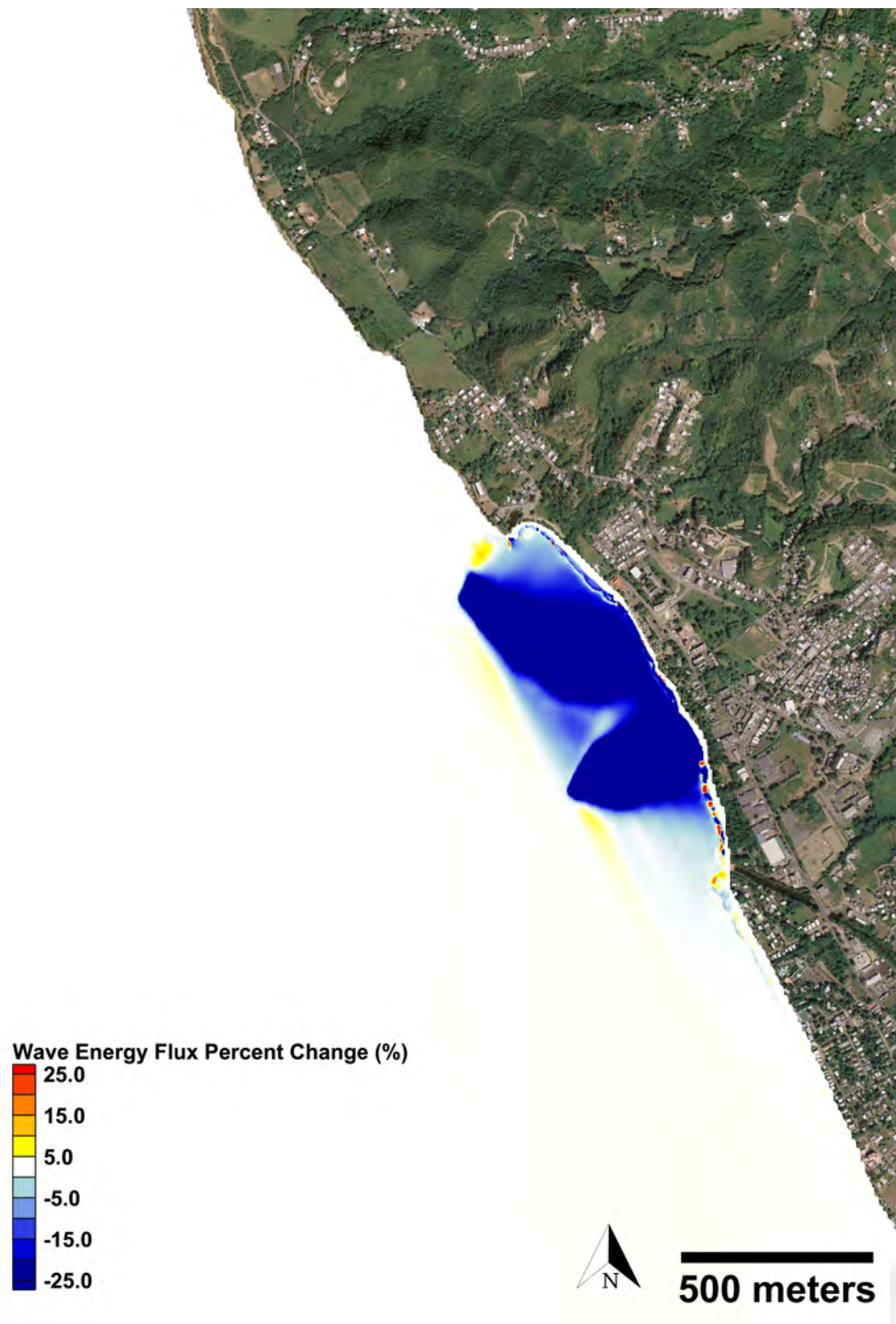


**Figure 5.12:** Wave energy flux response (percentage wise) for the peak hour of January 2<sup>nd</sup>, 2013 for Case 2. The reddish and blueish colors represent an increase and decrease in wave energy flux, respectively.

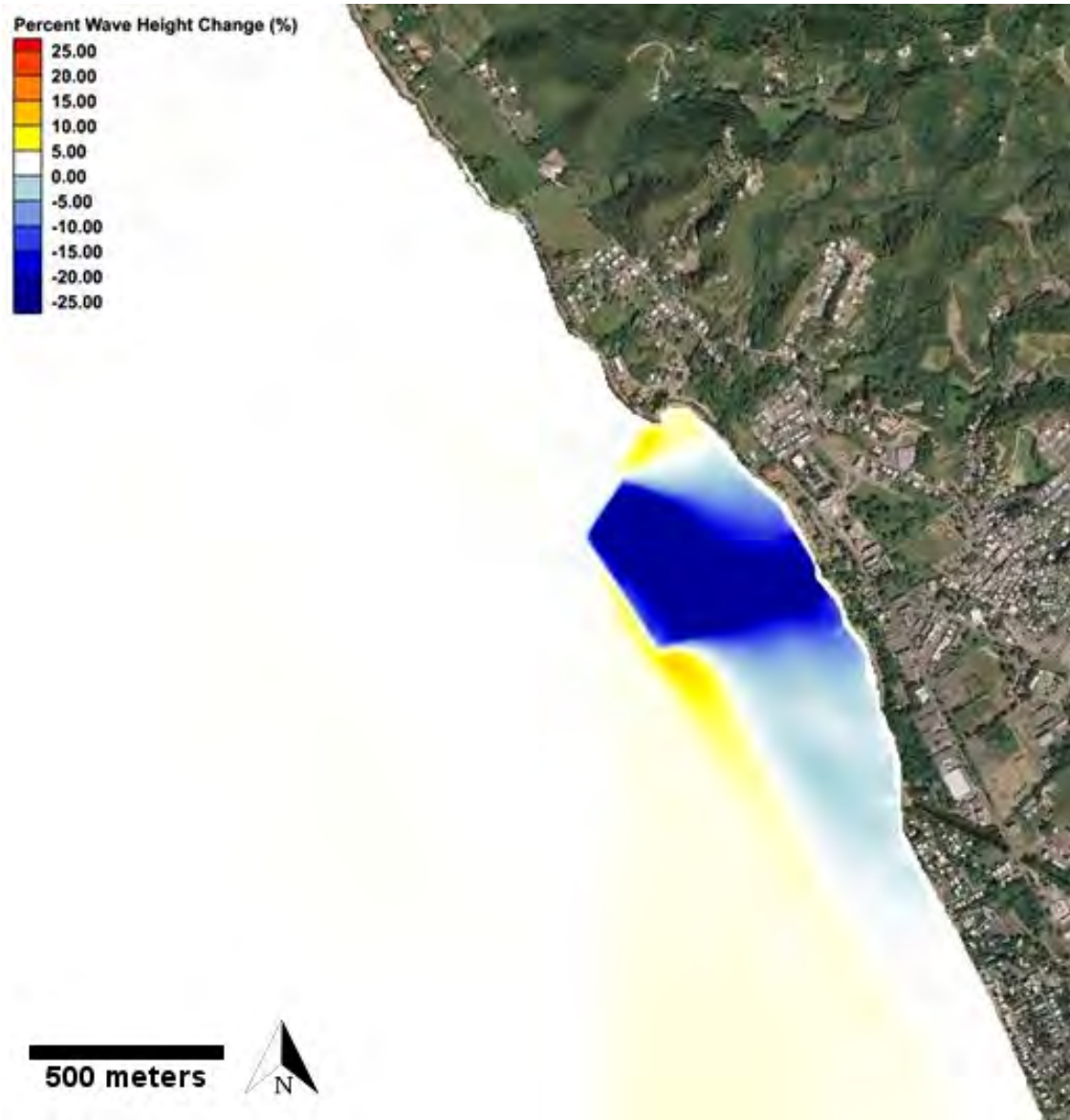


**Figure 5.13:** Wave height response (percentage wise) for the peak hour of January 2<sup>nd</sup>, 2013 for Case 1. The reddish and blueish colors represent an increase and decrease in wave height, respectively.

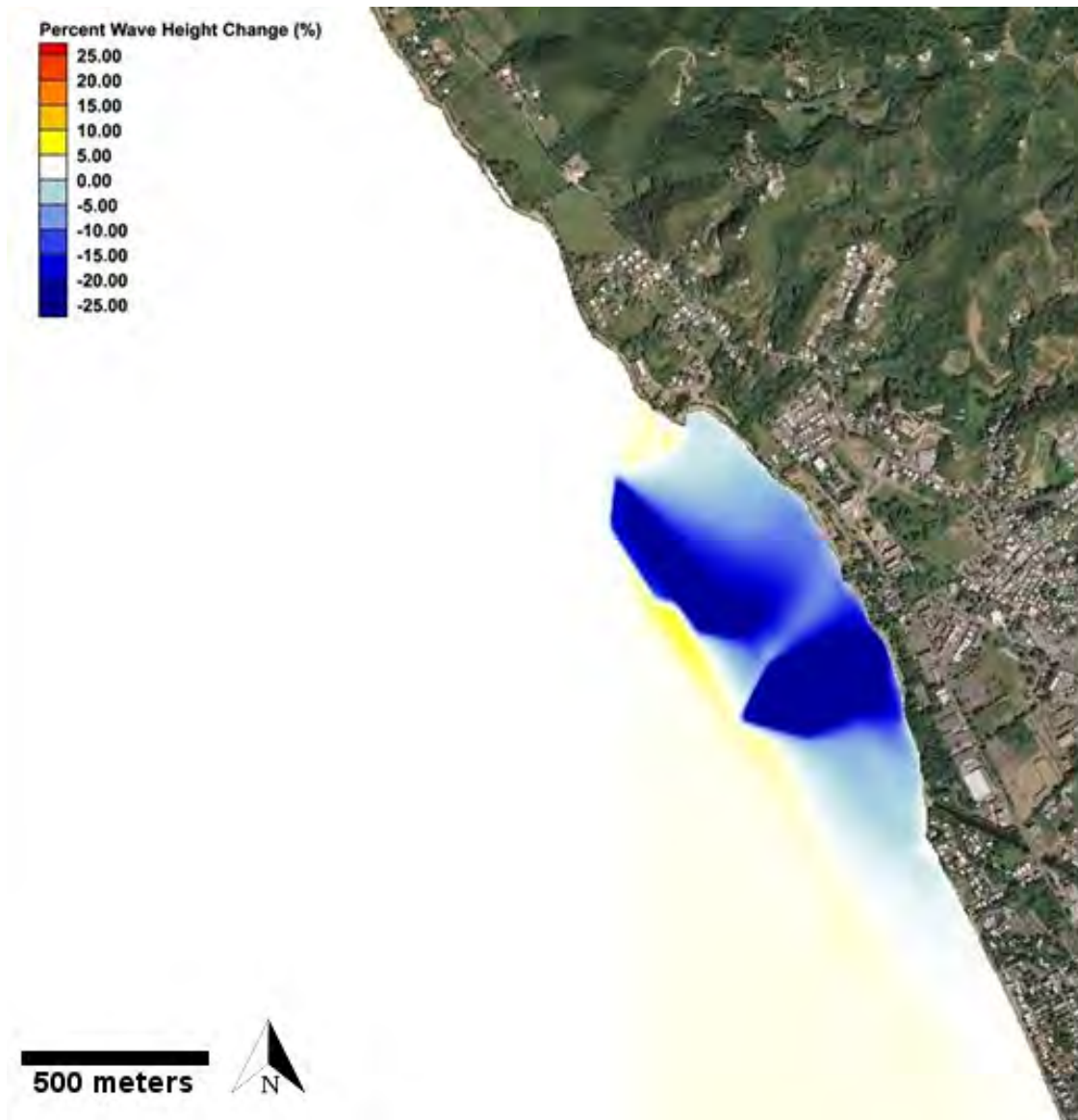


**Figure 5.14:** Wave height response (percentage wise) for the peak hour of January 2<sup>nd</sup>, 2013 for Case 2. The reddish and blueish colors represent an increase and decrease in wave height, respectively.

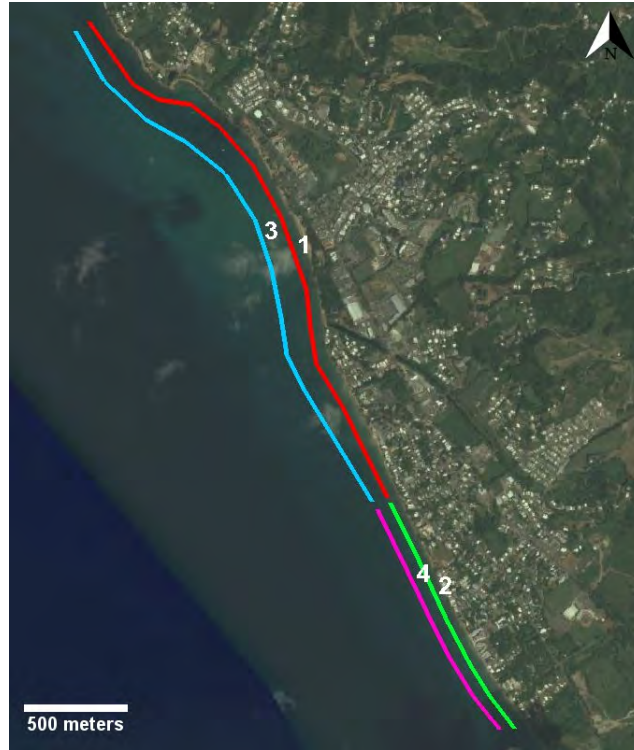


**Figure 5.15:** Map depicting the alongshore observation profiles for the 2 m depth contour (a and b) and the 5 m depth contour (c and d).

millimeters. As expected, there was no response to dredging northward of the sand shoal since the wave climate from January and February 2013 was mostly composed by northerly winter swells, with wave direction between 0 and 30 degrees.

The changes of wave energy flux over the existing wave climate conditions can be visualized percentage wise in Figure 5.11 and 5.12 for Case 1 and Case 2, respectively. Figures 5.13 and 5.14 display the percent change in significant wave height caused by mining Bajo Blanco during an instant of the simulation. Case 1 induced a maximum decrease in wave height of approximately 25% at the sand shoal, followed by a shadow zone of decreased wave height in the direction of wave propagation. The energy focused at the edges of the sand shoal, producing a 15-20% increase in wave height. Case 2 generated similar results as the single dredging scenario with a wider shadow zone and approximately 25% decrease in wave height. Downstream, waves increased height by less than 10% producing wave height increments in the magnitude of millimeters for that instance.

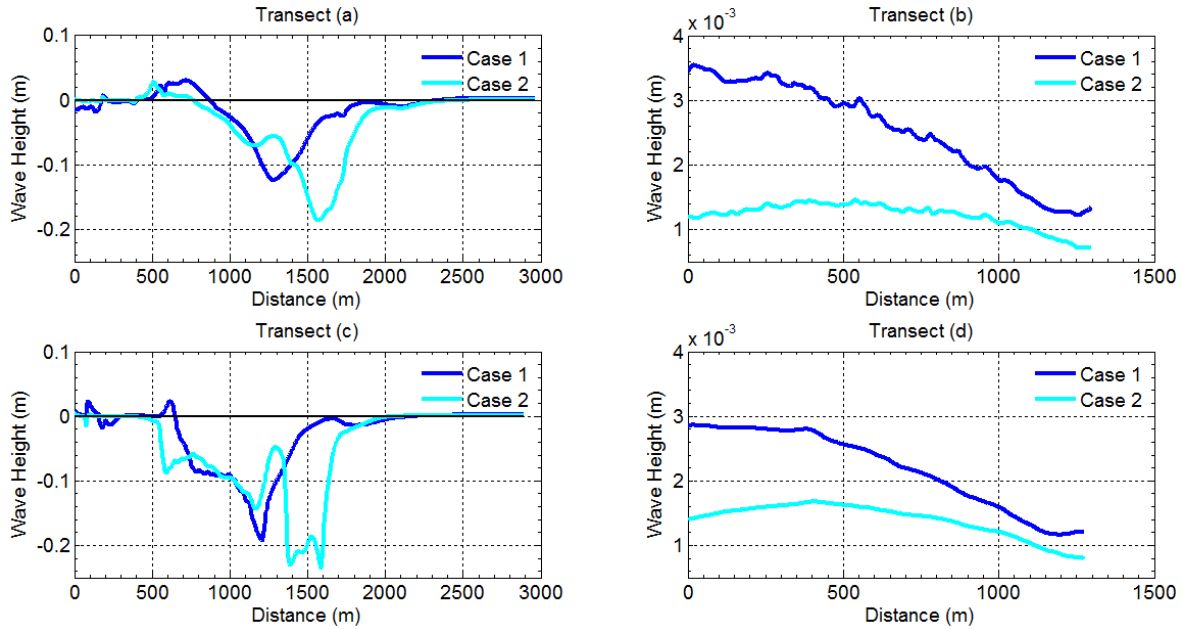


**Figure 5.16:** Wave height response observation profile for Case 1 (blue) and Case 2 (cyan) dredging scenarios during the peak hour of January 2<sup>nd</sup>, 2013. Transects (a)-(b) and (c)-(d) are the observation profiles along the 2 m and 5 m depth contour, respectively.

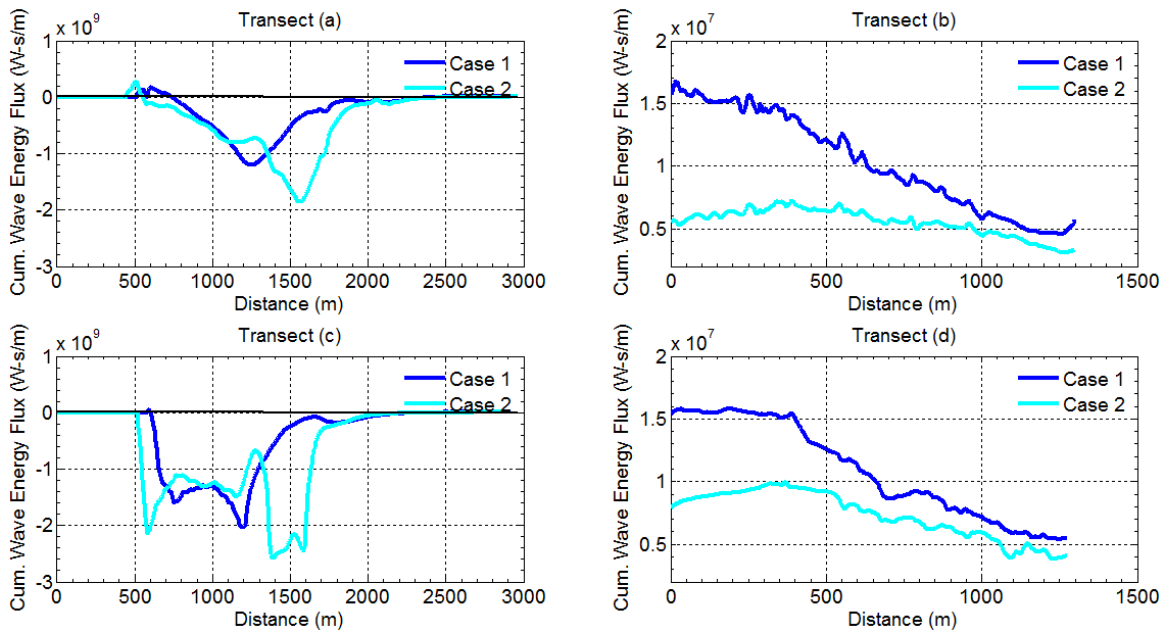


**Figure 5.17:** Cumulative wave energy flux response observation profile for single (blue) and multiple (cyan) dredging scenarios during the peak hour of January 2<sup>nd</sup>, 2013. Transects (a)-(b) and (c)-(d) are the observation profiles along the 2 m and 5 m depth contour, respectively.

To quantitatively compare the wave height and wave energy flux for both cases, the results are now analyzed along transects in the nearshore region at the 2 m and 5 m depth contours, as seen in Figure 5.15. Figure 5.16 shows the wave height response for Case 1 (blue) and Case 2 (cyan), where transects (a) - (b) and (c) - (d) represent the 2 m and 5 m depth contour line from TPMR all the way down to Córcega beach, respectively. Figure 5.17 presents the wave energy flux response for the same region. Transects (a) and (c) clearly illustrate a shadow zone of decreased wave height and wave energy flux as a consequence of dredging Bajo Blanco. Conservation of energy produced an area of increased wave height and wave energy flux that extended approximately 2 km south, as seen in transect (b) and (d). How the decrease in wave energy flux impacts wave-induced currents and morphology change in the nearshore region is discussed in the next sections.

### 5.3.3 Current response

Given the relatively weak tidal currents in Rincón, sediment transport in the region is dominated by wave-induced currents. During large winter swells, alongshore currents have a southeast direction in the form of an alongshore jet flowing from the TPMR towards the Bajo Blanco sand shoal, as shown in Figure 5.18. This figure shows a snapshot of the wave-induced currents on January 2<sup>nd</sup>, 2013 at 4 AM. As this alongshore jet flows closer to Bajo Blanco it decreases in magnitude due to a reduction in wave-induced pressure gradients. It is very likely that this alongshore jet dominates sediment transport dynamics in this region of Rincón. As a result, it is important to understand what are the potential effects of sand mining the Bajo Blanco sand shoal on the structure of this current.

The post-dredging instantaneous current and current response for both cases are presented from Figure 5.19 to 5.22, respectively. In general, the current magnitudes increased at the edges of the dredge areas in both cases, and decreased at the dredge areas. Case 1 appears to significantly impact the spatial structure of the alongshore jet, leading to a much narrower jet above the dredge area (deeper water). A very significant change is evident in Case 2 leading to a large increment in

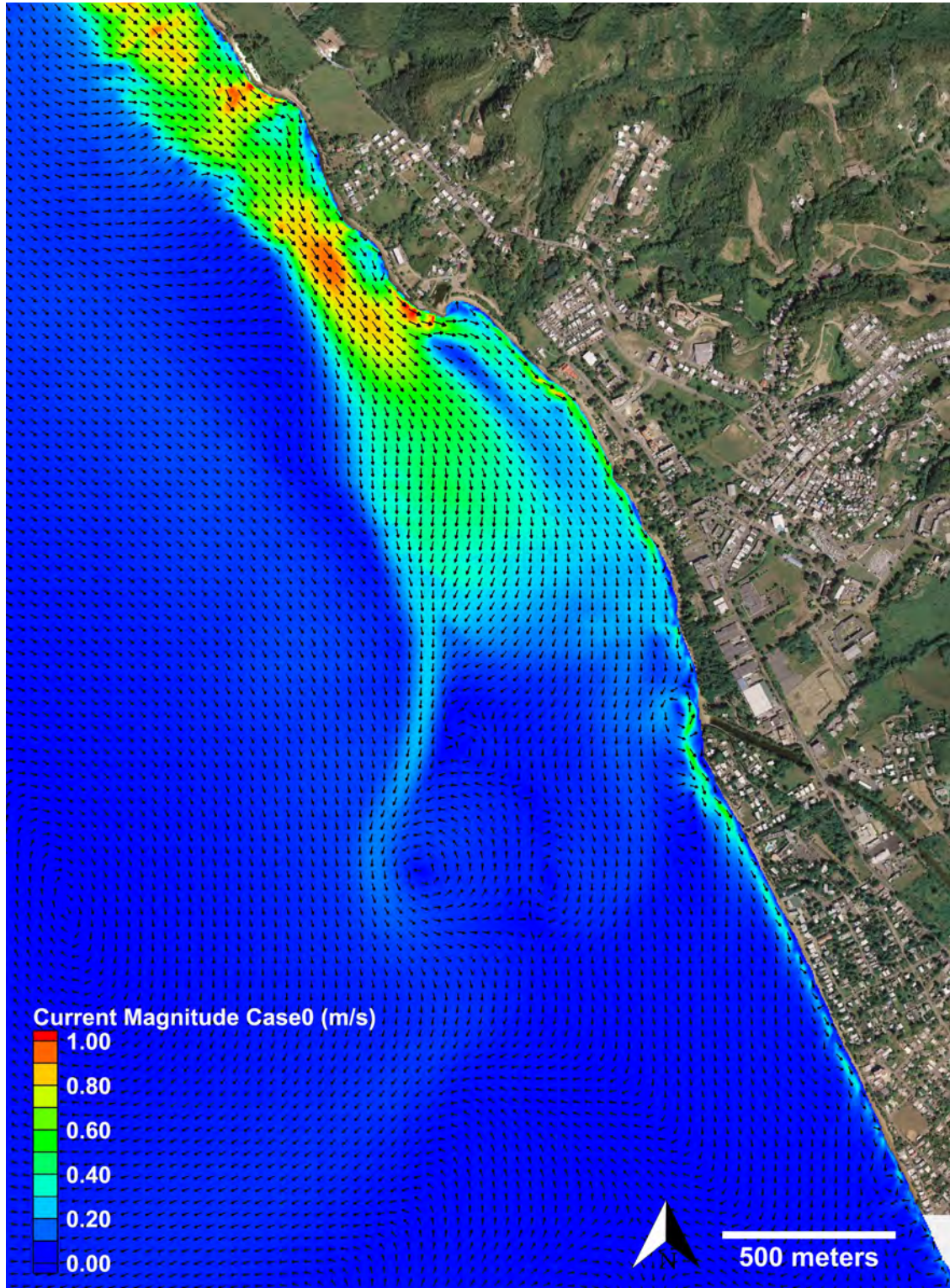


**Figure 5.18:** Pre-dredging CMS numerical model current magnitude and direction results for existing conditions on January 2<sup>nd</sup>, 2013 at 4 AM.

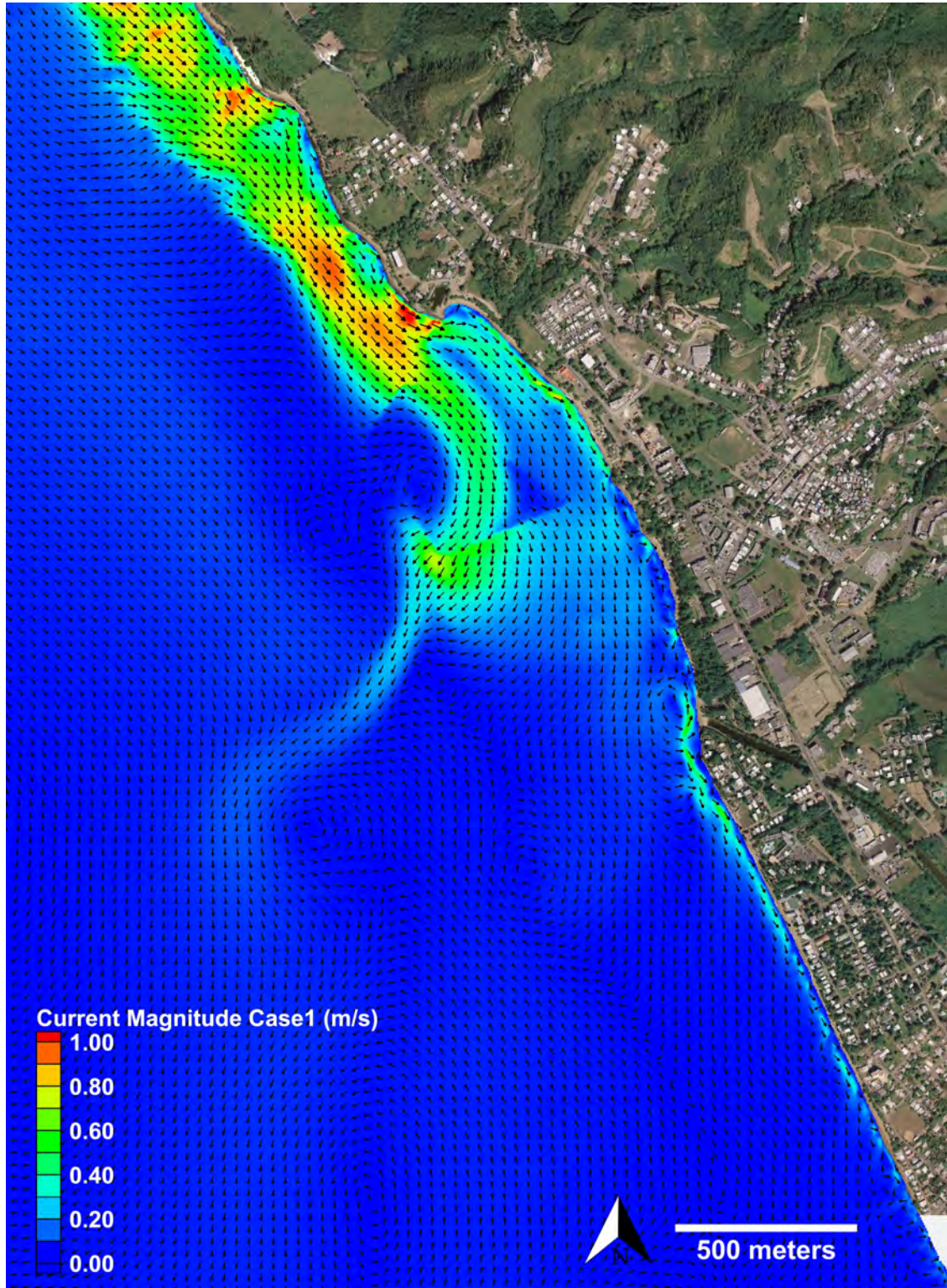


**Figure 5.19:** Post-dredging CMS numerical model current magnitude and direction results for Case 1 on January 2<sup>nd</sup>, 2013 at 4 AM.

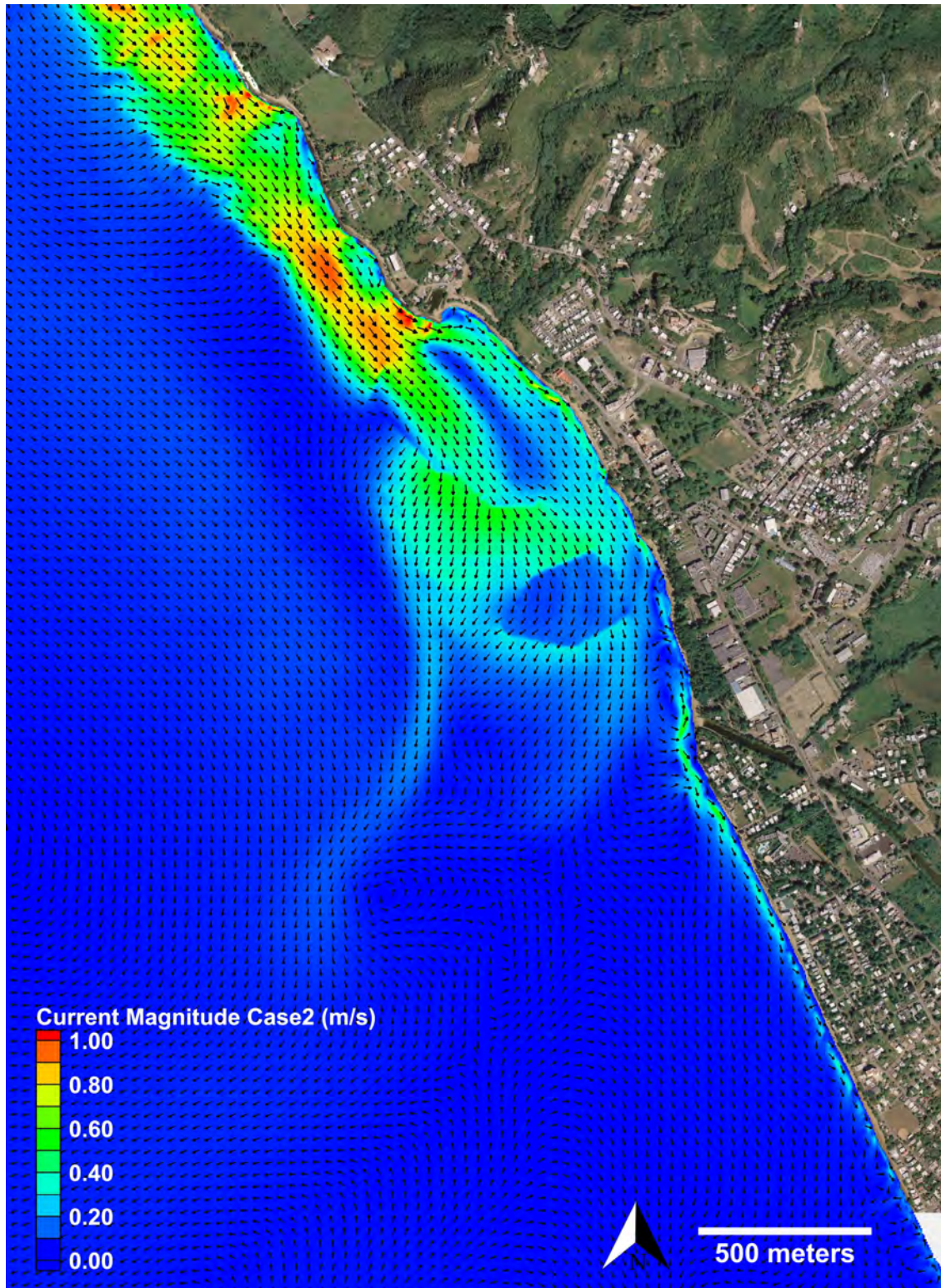


**Figure 5.20:** Post-dredging CMS numerical model current magnitude and direction results for Case 2 on January 2<sup>nd</sup>, 2013 at 4 AM.

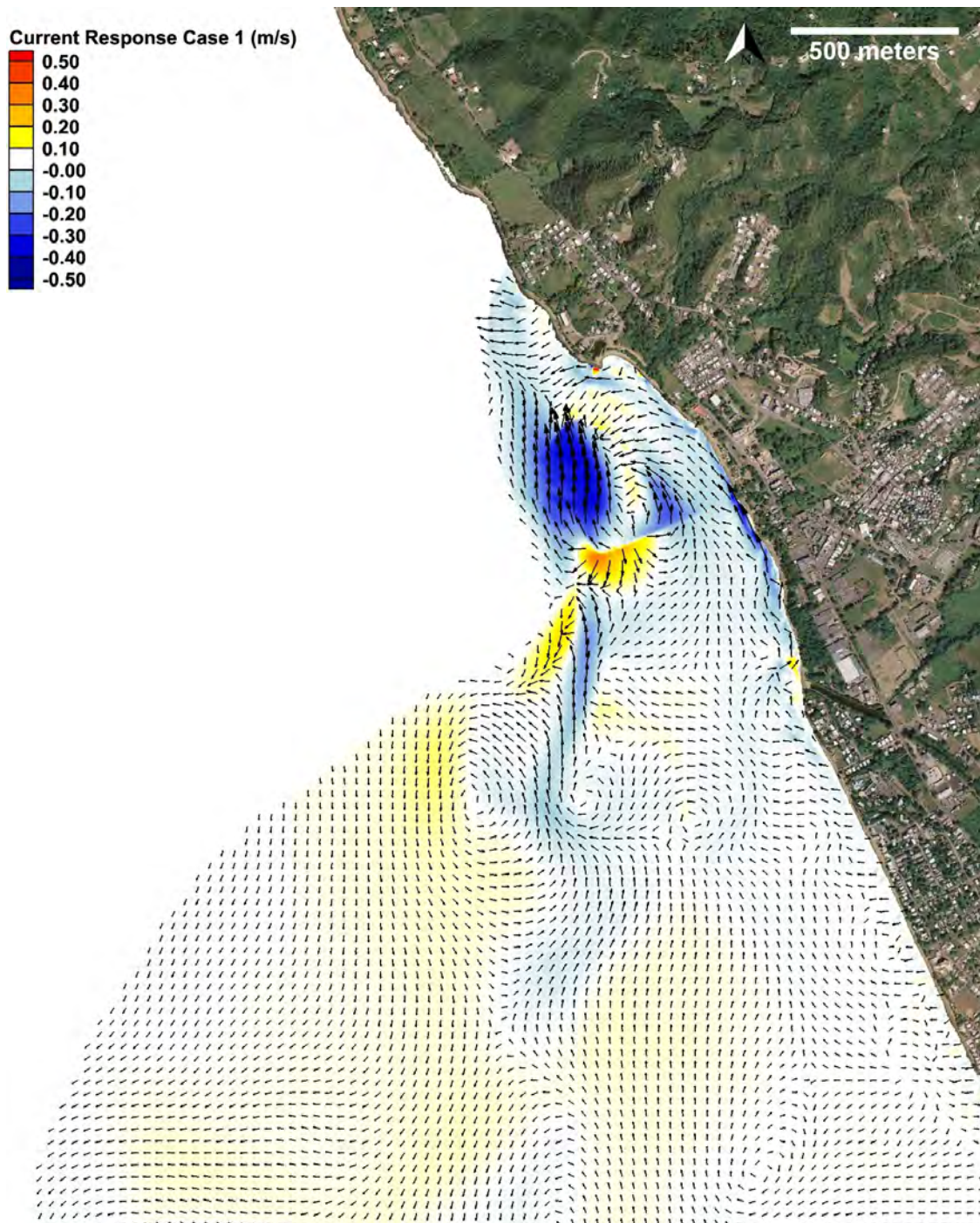


**Figure 5.21:** Post-dredging CMS numerical model current magnitude response for Case 1 during an instant of the simulation on January 2<sup>nd</sup>, 2013 at 4 AM. The reddish and blueish colors represent an increase and decrease in current magnitude, respectively, while the vectors represent the direction of the current response vector.

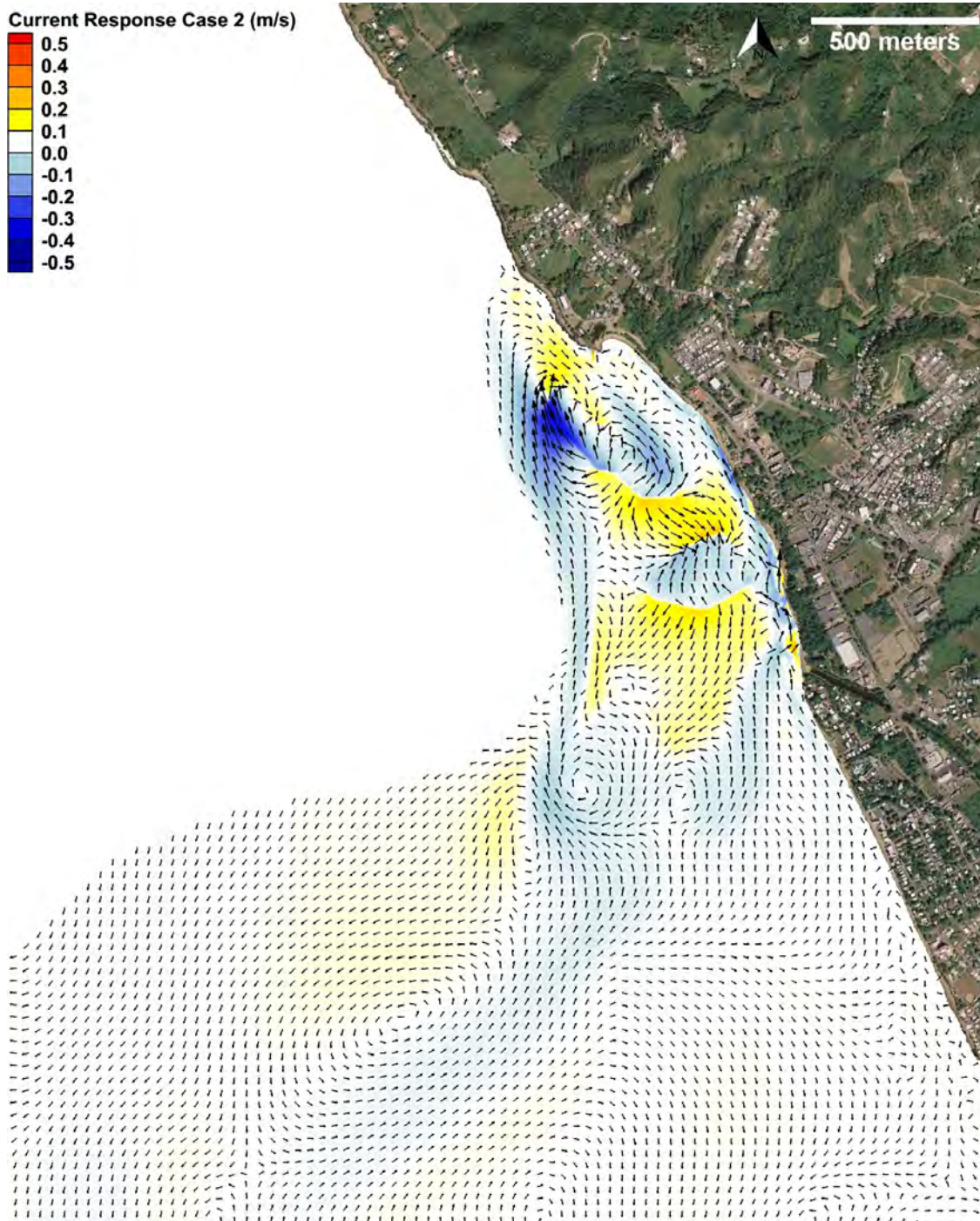


**Figure 5.22:** Post-dredging CMS numerical model current magnitude response for Case 2 during an instant of the simulation on January 2<sup>nd</sup>, 2013 at 4 AM. The reddish and blueish colors represent an increase and decrease in current magnitude, respectively, while the vectors represent the direction of the current response vector.

current magnitude in-between the dredge areas. The next section analyzes the potential effects of the changes in wave climate and current velocity distributions (discussed in this and the previous section) on the morphology change associated with these two dredge scenarios.

#### **5.3.4 Morphology response**

Chardón (2013) evaluated morphology change using a coupled CMS numerical model along a stretch of coast in Rincón, Puerto Rico. The CMS model provided acceptable results of morphology change response when compared with field measurements collected before and after extreme events (Hurricane Sandy and Tropical Storm Isaac). For the present study, morphology change is computed using the CMS model for a two month period (January/February 2013) for each of the borrow site scenarios.

Figures 5.23 to 5.27 display the simulated morphology change for existing conditions, post-dredging conditions, and the dredging-induced morphology response, respectively. White areas represent hard bottom as well as areas with no morphology change. Regions of accretion and erosion are depicted with reddish and blueish colors, respectively. Results for the existing bathymetry (Figure 5.23) show sand accretion seaward of Bajo Blanco. Patterns of accretion near the shore are visible, with an average depth reduction of approximately 0.5 m in some locations. After dredging the Bajo Blanco sand shoal (Figures 5.26 and 5.27), sediment particles were deposited at the borrow sites, as would be expected, given the reduced turbulent kinetic energy in these areas.

There is a pattern of increased sediment deposition in the shadow zone (reduction in wave height) in both cases caused by the dredge areas, as seen in Figures 5.26 and 5.27, with slight erosion south of each dredge area. Model results also suggest an accumulation of sediment southwest of the dredge areas, being much more noticeable in Case 1. Far downstream of the borrow site, there was little to no response in morphology change as a consequence of dredging Bajo Blanco. This is also expected since the effects of dredging on the spatial distribution of the wave energy flux are also mostly constrained to areas close to and seaward of the dredge areas.

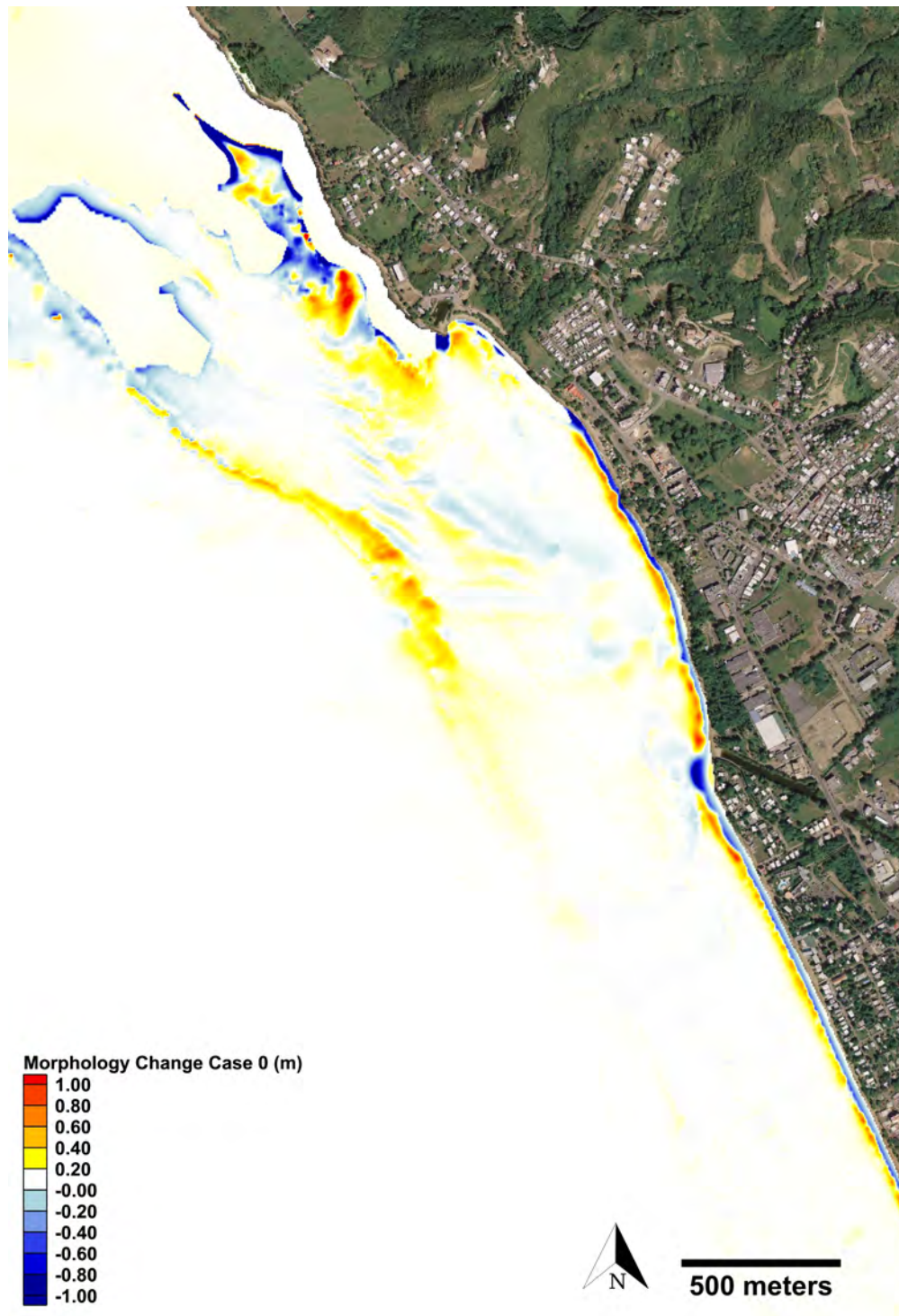


**Figure 5.23:** Simulated cumulative morphological change at Bajo Blanco for existing bathymetry during the months of January and February 2013. The reddish and blueish colors represent sand deposition and erosion, respectively.

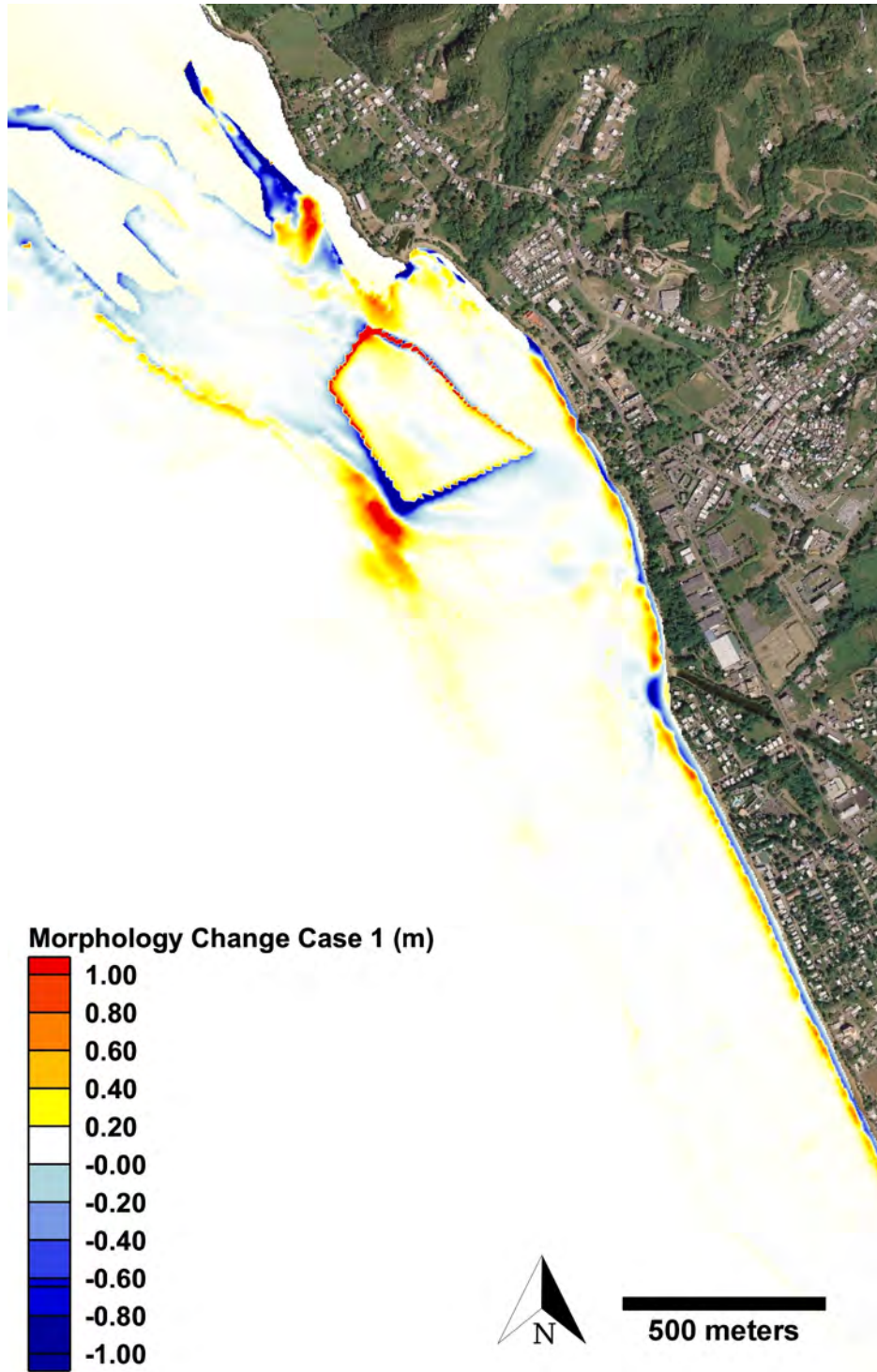


**Figure 5.24:** Simulated cumulative morphological change at Bajo Blanco for Case 1 during the months of January and February 2013. The reddish and blueish colors represent sand deposition and erosion, respectively.

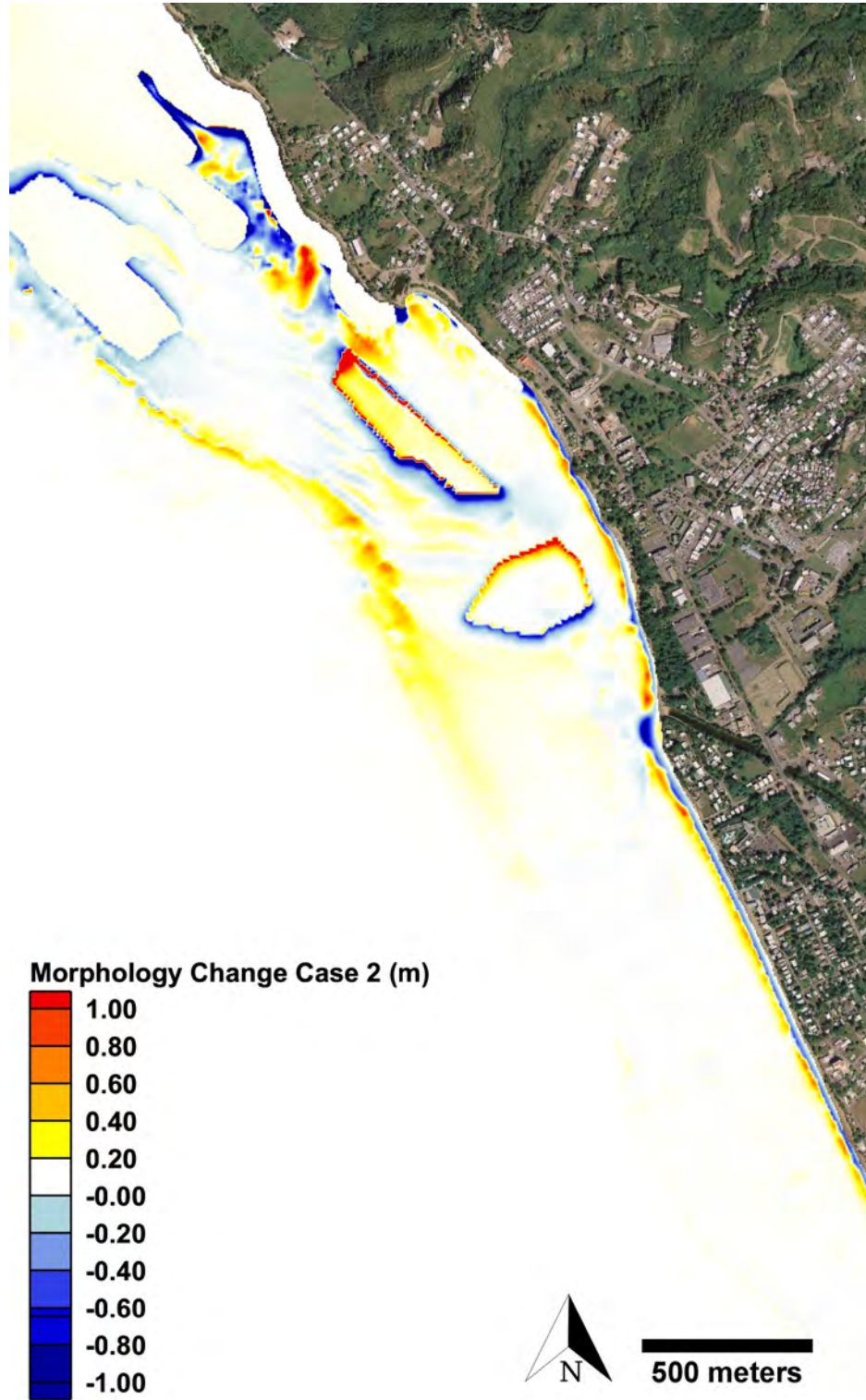


**Figure 5.25:** Simulated cumulative morphological change at Bajo Blanco for Case 2 during the months of January and February 2013. The reddish and blueish colors represent sand deposition and erosion, respectively.

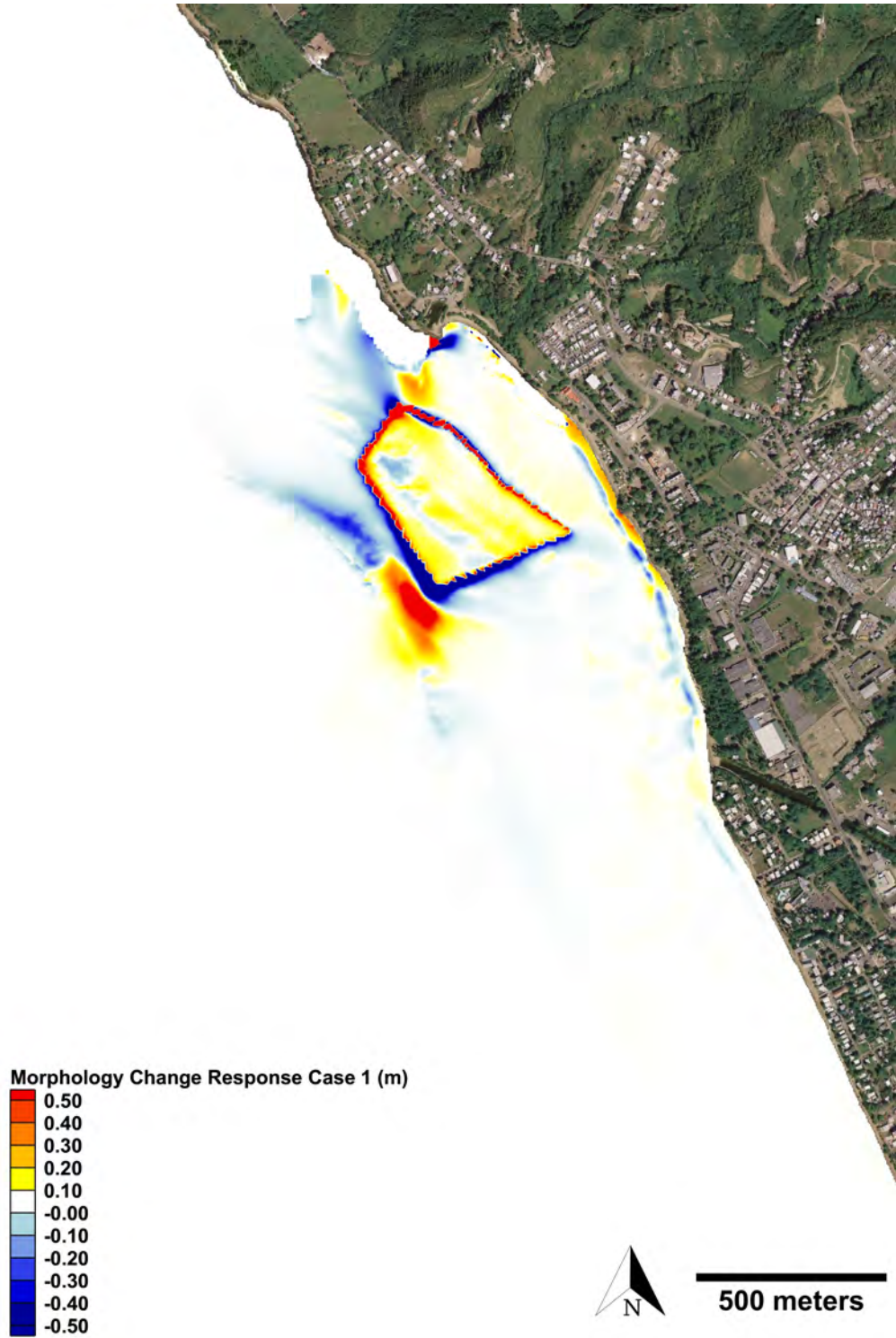


**Figure 5.26:** Post-dredging CMS numerical model morphology change response for Case 1 during the two month simulation period (January - February 2013). The reddish and blueish colors represent an increase and decrease in sediment deposition, respectively.

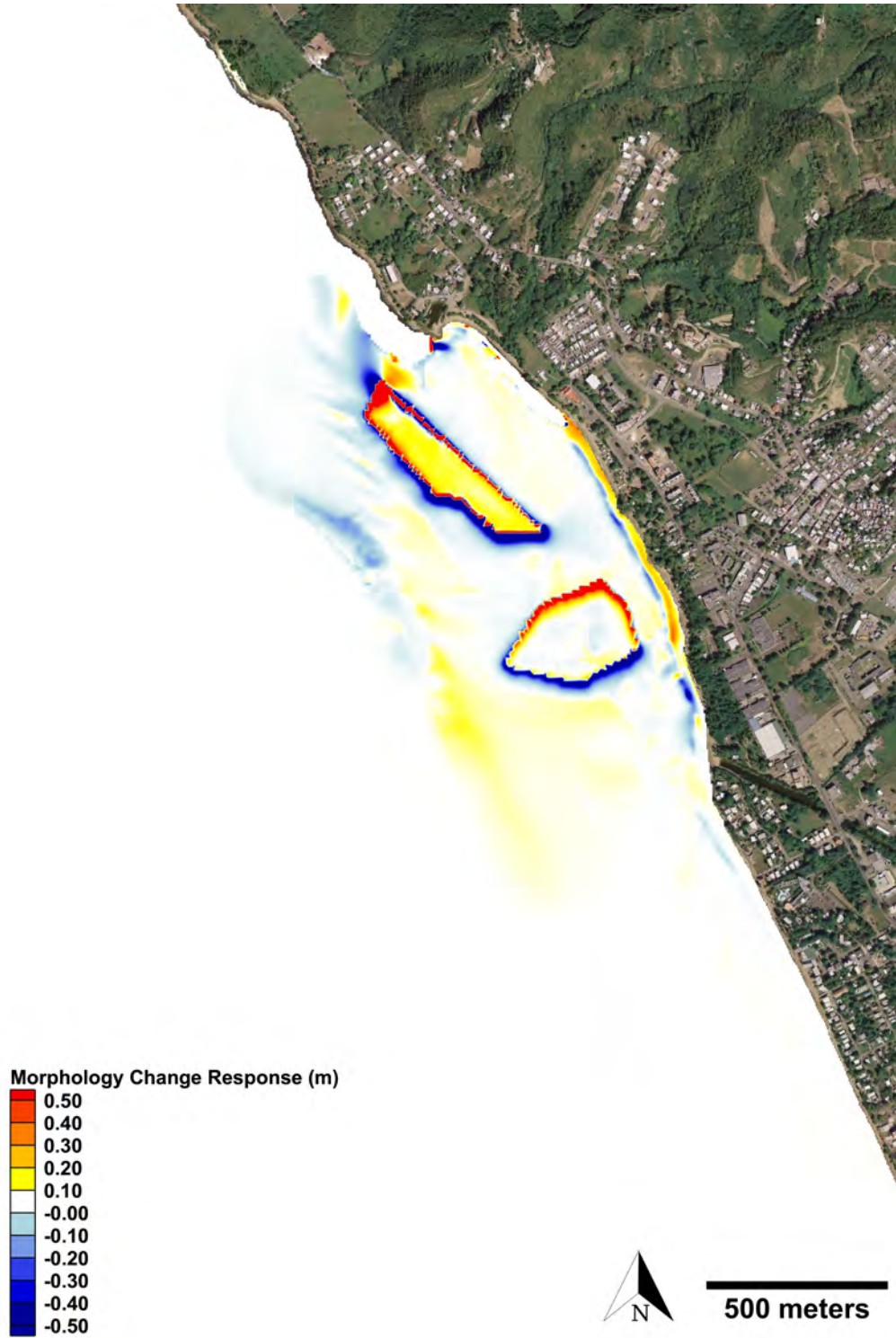


**Figure 5.27:** Post-dredging CMS numerical model morphology change response for Case 2 during the two month simulation period (January - February 2013). The reddish and blueish colors represent an increase and decrease in sediment deposition, respectively.

## 5.4 Particle Tracking Model (PTM)

Understanding the dispersal of sediment particles during dredging operations is important to prevent possible damage on marine ecosystems, which may be negatively affected by an increase in sediment concentration. Computational methods such as the USACE Particle Tracking Model (PTM) have been developed to estimate the fate of sediment particles using output results from previous numerical models.

The TPMR, located just north of Bajo Blanco, has been a marine protected reserve since 2004 and home to some of the healthiest Elkhorn corals specimens in the Caribbean. The deposition of fine sediments on coral reefs can block the sunlight and harm the photosynthesis process (Storlazzi et al., 2015). These effects can significantly impact the health of corals and the entire marine ecosystem. The next section involves the application of the PTM module to determine the appropriate conditions that would minimize the plume of fine sediments migrating towards TPMR during the dredging of the Bajo Blanco sand shoal.

### 5.4.1 Model overview

The PTM is a two-dimensional model that uses wave and current velocity datasets as forcing parameters to accurately predict the fate of sediments in coastal waters, estuaries, rivers, and waterways (Davis et al., 2005). The model has the ability to recreate sediment movement caused by the flow field as well as its deposition and re-suspension. Sediment movement is a function of the velocity of the flow field, particle grain size and settling velocity, bottom friction, among other factors. The PTM module solves the transport of particles by applying interpolation and integration at the particle's location as a result of the Eulerian force surrounding the particle at a certain time (Lackey, 2007). The new particle's position can be determined with equation 5.6, where the velocity vector ( $\vec{U}_{HV}$ ) is composed of the horizontal ( $U_H$ ) and vertical component ( $U_V$ ), and  $X$  is the location of the particle. As shown in equation 5.7, the horizontal velocity is a function of

the advective forcing ( $U_{HA}$ ) and diffusion ( $U_{HD}$ ) in the horizontal direction. The vertical velocity component is a function of similar terms ( $U_{VA}$  and  $U_{VD}$  for advective and diffusion, respectively) with the addition of the settling velocity ( $U_{VS}$ ), as shown in equation 5.8 (MacDonald, 2006).

$$\frac{d\vec{X}}{dt} = \vec{U}_{HV} \quad (5.6)$$

$$U_H = U_{HA} + U_{HD} \quad (5.7)$$

$$U_V = U_{VA} + U_{VD} - U_{VS} \quad (5.8)$$

The suspension of sediment particles is influenced by the bottom shear stress, which is a function of the flow velocity, wave conditions, seabed roughness and sediment properties. The higher the shear stress, the more susceptible particles are for being re-suspended. For more information regarding the governing equations of the PTM module, please refer to the "*PTM: Particle Tracking Model, Model Theory, Implementation and Example Applications report*" (MacDonald, 2006). For the current study, existing hydrodynamic and wave results generated with the coupled CMS numerical model were used as forcing conditions for the PTM module to simulate the movement of suspended sediment plumes during the wave climate conditions of January 2013.

#### 5.4.2 Model set-up

The PTM model requires detailed bathymetry, hydrodynamic model output and sediment characteristics in order to properly simulate sediment dispersal throughout the domain. To evaluate sediment transport and dispersal at Bajo Blanco during dredging activities, the existing (pre-dredging) bathymetric conditions were used. As previously mentioned in section 4.3, the cell resolution varied from 4 m in the nearshore to 32 m in the offshore (see Figure 4.10). A spatially uniform

**Table 5.2:** PTM model set-up and sediment characteristics used for the simulation period.

<b>Sand particle properties</b>		
<b>Parameter</b>	<b>Value</b>	<b>Units</b>
<b>Parcel mass</b>	10	<i>kg</i>
<b>Vertical radius</b>	1	<i>m</i>
<b>Horizontal radius</b>	1	<i>m</i>
<b>Rate</b>	0.1	<i>kg/s</i>
<b>Median grain size</b>	0.06	<i>mm</i>
<b>Standard deviation</b>	8	<i>Phi – units</i>
<b>Density</b>	2650	<i>kg/m<sup>3</sup></i>

native bed sediment grain size was specified at each cell using the average  $D_{35}$ ,  $D_{50}$ ,  $D_{90}$  and standard deviation collected from the Bajo Blanco sand shoal sand samples. Sand properties and PTM model set-up parameters are presented in Table 5.2. The parcel mass at the source (borrow site) was set at 10 kg with a release rate of 0.1 kg/s of suspended fine sediments during dredging operations. According to the Udden-Wentworth scale (Wentworth, 1922), fine sand particle ranges from 0.0625 mm to 0.25 mm with a density of  $2,650 \text{ kg/m}^3$ . For the PTM simulation, a grain size value of 0.06 mm was used to simulate the behavior of the finest possible sediment particles that may be suspended during dredging at Bajo Blanco. However, the smallest sieve size available during the sieve analysis corresponds to a 0.074 mm spacing, meaning there is no evidence that such fine grain sizes are present at Bajo Blanco. However, the purpose of these simulations are to present a worst case scenario of sediment dispersal in case such small sediments are found in the dredged material.

As mentioned above, the existing wave and hydrodynamic conditions during January 2013 were used to force PTM module in order to predict plume dispersal during dredging operations and to better understand under which conditions dredging should be conducted to minimize the potential of suspended sediments reaching TPMR. Figure 5.28 shows the wave height and water surface elevation during the plume dispersal computations. Figure 5.29 shows the line source implemented for the PTM model, conducted during the conditions presented in Table 5.3. Each

**Table 5.3:** Release periods for each of the dredging scenarios, with their corresponding tide and wave forcing characteristics.

Scenario	Tidal forcing	Wave forcing	Particle release date & time		
			Release 1	Release 2	Release time
a	High to Low	Strong	Jan, 2nd	Jan, 4th	7:00 - 8:00 am
b	Low to High	Weak	Jan, 6th	Jan, 8th	7:00 - 8:00 am
c	High to Low	Weak	Jan, 12th	Jan, 14th	7:00 - 8:00 am
d	Low to High	Strong	Jan, 25th	Jan, 27th	7:00 - 8:00 am

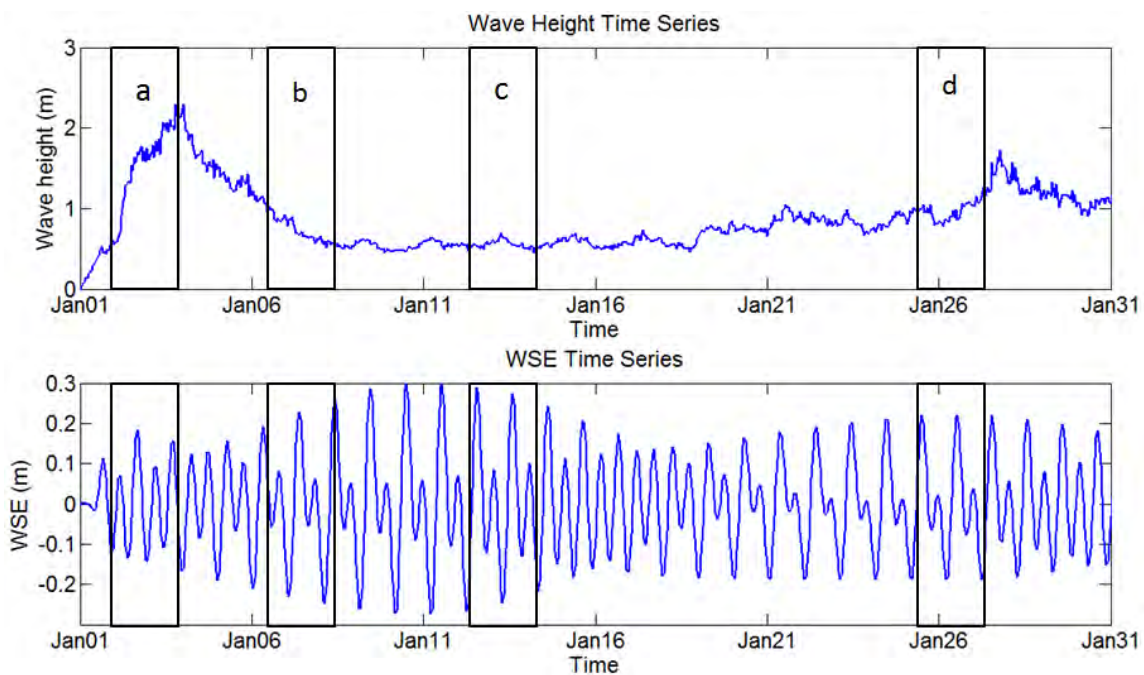


**Figure 5.28:** Plots of significant wave height (top) and water surface elevation (bottom) at the location of the Cari-COOS Rincón buoy during the month of January 2013. These results were used to determine the release period of sediment particles during specific sea state conditions.



**Figure 5.29:** PTM line source location with respect to the Tres Palmas Marine Reserve.

release lasted one hour in order to mimic the dredging activities. The purpose was to track the trajectories of suspended sediments during ebb/flood tides and low/moderate wave energy events. Sediments were released at a level of 1 m above the seabed. The simulation period extended for the entire month of January 2013 with output results every 5 minutes.

### 5.4.3 Model results

The simulation results for the different conditions are shown in Figure 5.30 to 5.33. The yellow area represents the extent of the TPMR. Current direction and magnitude are depicted with colored arrows, where the blue colors represent slow current velocities and red colors represent faster current velocities. White dots represent suspended particles and the brown dots represent particles that have settled in the seabed. Wave-induced sediment resuspension of particles already settled was resolved by the PTM model.

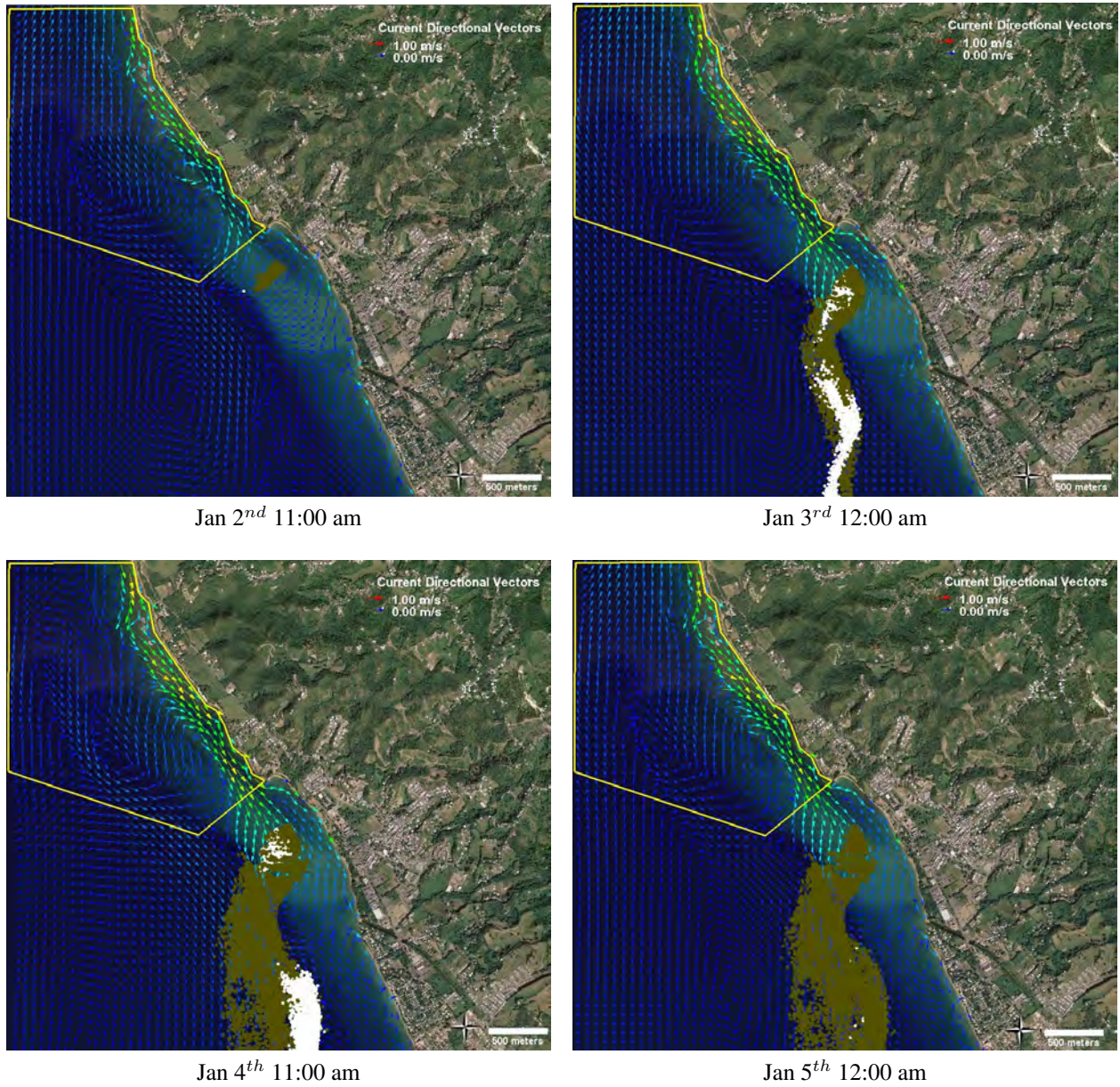


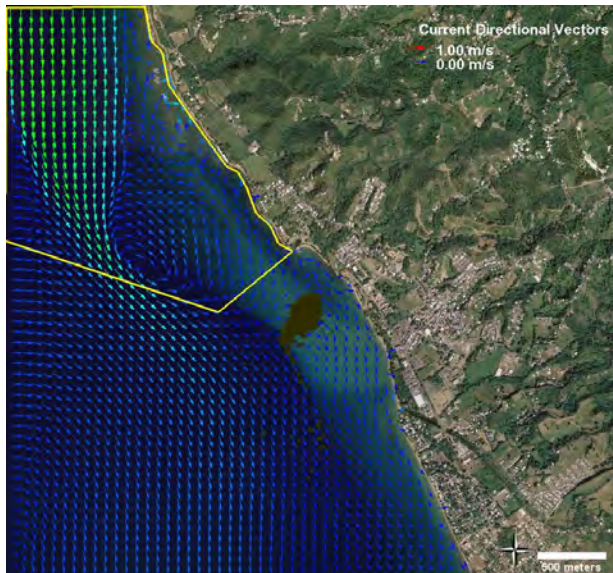
**Figure 5.30:** Release period corresponding to scenario (a), during ebb tide and moderate wave forcing. Wave-induced currents force suspended sediment particles to migrate south, away from TPMR.



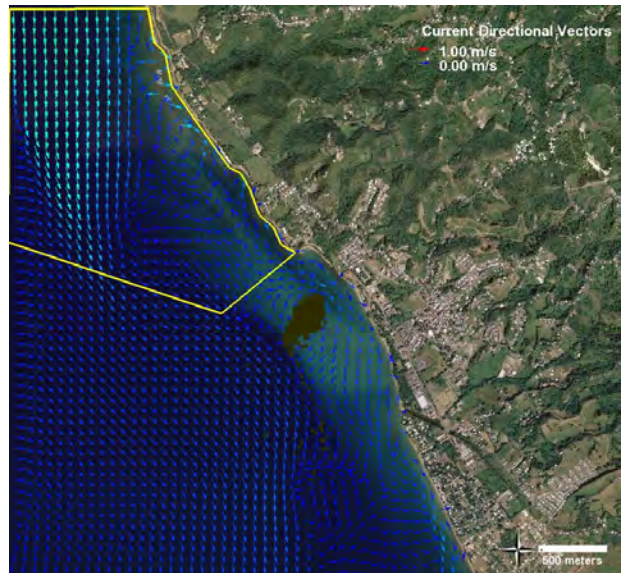
Jan 6<sup>th</sup> 11:00 am



Jan 7<sup>th</sup> 12:00 am



Jan 8<sup>th</sup> 11:00 am



Jan 9<sup>th</sup> 12:00 am

**Figure 5.31:** Release period corresponding to scenario (b), during flood tide and low wave forcing. The lack of strong alongshore currents allows settling of suspended sediment in the sand shoal.



Jan 12<sup>th</sup> 11:00 am



Jan 13<sup>th</sup> 12:00 am



Jan 14<sup>th</sup> 11:00 am



Jan 15<sup>th</sup> 12:00 am

**Figure 5.32:** Release period corresponding to scenario (c), during ebb tide and low wave forcing. The lack of strong longshore currents allow rapid settling of sediment particles on the sand shoal.



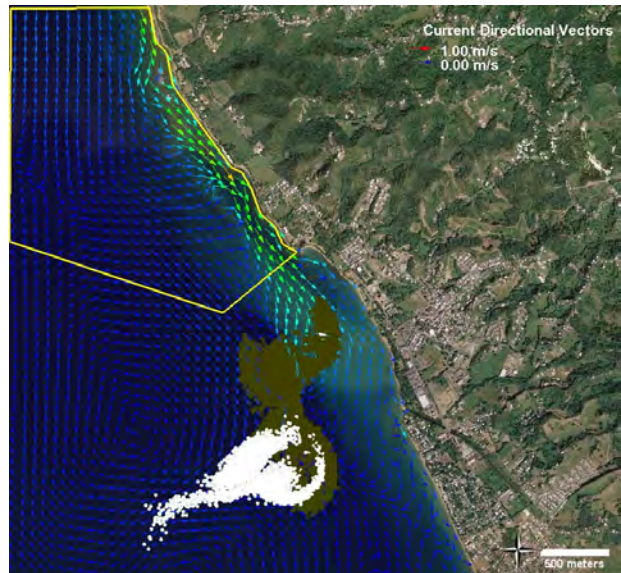
Jan 25<sup>th</sup> 11:00 am



Jan 26<sup>th</sup> 12:00 am



Jan 27<sup>th</sup> 11:00 am



Jan 28<sup>th</sup> 12:00 am

**Figure 5.33:** Release period corresponding to scenario (d), during flood tide and moderate wave forcing. Wave-induced currents force suspended sediment particles to migrate south, away from TPMR.

Overall, results suggest a southward transport of fine sediments during moderate wave forcing in response to moderate wave-induced currents flowing into Bajo Blanco. This transport is caused by an alongshore jet that forces suspended particles to migrate south of the sand shoal. The conditions from January 6<sup>th</sup> to January 8<sup>th</sup>, shown in Figure 5.31, exhibited very low wave activity. Sediment particles barely moved from the extraction site, quickly settling to the seabed after release. Similarly, as shown in Figure 5.32, for the ebb tide - low wave conditions of January 12<sup>th</sup> to January 15<sup>th</sup>, the particles showed no migration with almost instant deposition in the area of extraction. During the conditions between January 2<sup>nd</sup> and January 4<sup>th</sup> 2013, a strong jet of wave-induced currents can be seen in Figure 5.30 through a channel between the coral reefs and the shoreline. Those currents forced suspended particles to travel south and slightly offshore until they were totally deposited in deeper waters days after their release. The same behavior is observed in Figure 5.33, where wave-induced currents produced by moderate northerly waves caused a southward migration of suspended sediments as far as approximately 2 km from Bajo Blanco.

## **5.5 Concluding remarks**

In this chapter, two dredging configurations were evaluated using the coupled CMS numerical model that was validated in Chapter 4. The volume extracted for each case was 1,010,000  $m^3$  and 1,080,000  $m^3$  for Case 1 and Case 2, respectively. For both cases, the CMS numerical model results for wave height, morphological change and coastal currents were used to evaluate the effects of sand mining at Bajo Blanco along the coast of Rincón.

Results suggest that the larger depths created by the borrow areas cause a decrease in wave energy at the dredge areas due to wave refraction, and an increase in wave energy flux in adjacent areas. This shadow zone of decreased wave energy flux at the Bajo Blanco sand shoal could lead to sediment deposition in the shoreward areas of the borrow sites, which could in turn affect the natural alongshore drift of sediments if a significant perturbation to the coastline is created due to sediment deposition.

Sediment transport results for both cases suggest that the larger depths at the borrow areas could function as a partial sediment trap of sediments coming from the north during strong wave events. If the health of Rincón beaches depends on a steady supply of sediment from locations north of the TPMR, this partial interruption of sediment transport could have an effect on beach behavior.

Finally, results from PTM simulations suggest that, under low wave conditions, sand particles would quickly settle near the sand shoal during dredging activities. Waves are able to maintain sediments suspended for a much longer time, increasing the reach of the dredged sediment plume, but causing southward wave-induced currents which advect the sediment plume away from the TPMR. It should be noted that these PTM simulations were conducted for tide, wind and wave-driven flow only. It is well known that large-scale flows affect the circulation in the Mona Passage, and that these flows can sometimes cause a net northward flow near Rincón. In case dredging operations are conducted at Bajo Blanco, the presence of large-scale flows near Rincón should be monitored using the HF Radar Network operated by CariCOOS.

## Chapter 6

### CONCLUSION AND RECOMMENDATIONS

The present study has analyzed the potential for the Bajo Blanco sand shoal to serve as a beach nourishment borrow site for eroded beaches in Rincón. First, a high resolution bathymetric survey was performed at Bajo Blanco using a jestki-based bathymetric system (Chardón and Canals, 2012). This data was then compared with available bathymetric data from the 10-meter resolution 2007 NGDC-DEM. The comparison showed significant morphological changes between 2007 and 2014, indicating a possible shoreward propagation of the Bajo Blanco sand shoal. While it was difficult to draw conclusions regarding the mechanisms for the observed morphology changes, the results confirm the morphodynamic complexity of Bajo Blanco, as suggested by Thieler et al. (2007) and Chardón (2013).

Sand samples from eroded beaches in Rincón and from the Bajo Blanco sand shoal were collected as part of the compatibility analysis of the study. Sieve analysis results showed that median grain sizes found at the Bajo Blanco sand shoal are indeed finer than the median grain size of the sand samples collected at the eroded beaches. Using the sediment grain size results and an alternative computation of Dean's overfill factor, it was estimated that 50 - 70 percent of additional sand volume would be needed to account for the differences in grain sizes between the native and borrow area sand. Preliminary computations suggest an amount on the order of  $1 \times 10^6 \text{ m}^3$ . This volume is comparable to other beach nourishment projects with similar shoreline lengths. For example, a beach nourishment project in the state of Florida with a similar beach length resulted in a dredged volume of around 1 million cubic meters (Trembanis and Pilkey, 1998).

A major concern related to the potential use of Bajo Blanco as a sand source is whether dredg-

ing Bajo Blanco would cause major changes to the wave climate affecting Rincón beaches. To evaluate the local nearshore wave climate response, a coupled wave, circulation and sediment transport model, the USACE's Coastal Modeling System, was used to simulate winter swell conditions during January and February 2013. This model was validated using field data and different wave spectra representations, yielding satisfactory model performance.

After model validation, two dredging scenarios were considered: a single dredge area (Case 1) and multiple (Case 2) dredging areas. Numerical model results for both cases produced a shadow zone of decreased wave energy flux landward of the sand shoal and an increase at the northwest and southwest edges of the dredge areas. As expected, these changes in wave energy caused a significant difference in the spatial structure of the wave-induced currents, especially on the structure of the alongshore currents flowing from the TPMR towards the Bajo Blanco sand shoal.

Significant changes in the wave climate and the spatial structure of the current velocities resulted in sediment deposition in areas between the borrow site and the shoreline for both cases. Model results also indicate that the dredge areas may serve as a partial sediment trap of sediments coming from the north during strong wave events. If the health of Rincón beaches depends on a steady supply of sediment from locations north of the TPMR, this partial interruption of sediment transport could have a negative effect on beach behavior and recovery from erosion events. The accretion pattern between the borrow site and the shoreline could lead to significant shoreline change in the long term depending on how fast the borrow sites fill with sediment in response to wave action and wave-induced currents. These significant changes may be reduced if less volume is extracted. The beach nourishment design by Salas (2014) considered a berm width of 36 meters. Reducing the berm width would cut into the required design volume, allowing the possibility of other dredging scenarios with lesser impact.

Finally, preliminary sediment dispersal simulations were conducted in order to understand how fine suspended sediment may behave during dredging operations at Bajo Blanco. Results showed that under low wave conditions, sand particles would quickly settle near the sand shoal during

dredging activities. During moderate wave events, however, waves are able to maintain sediments suspended for a much longer time, increasing the reach of the dredged sediment plume, but causing southward wave-induced currents which advect the sediment plume away from the TPMR. However, it was noted that the CMS model does not take into account large-scale circulation patterns such as an occasionally strong northward current flowing from the Caribbean Sea through the Mona Passage and into the Atlantic Ocean. Such large scale circulation features should be closely monitored during dredging operations. The CARICOOS High Frequency Radar (HFR) network is able to capture these large scale flows and should be monitored closely.

To further improve the outcomes of the present study, the following recommendations are provided:

- The implementation of a multi-beam echosounder with a heave/pitch/roll sensor in the jetski-based bathymetric survey system could significantly improve the high-resolution bathymetry data at Bajo Blanco and allow for a better understanding of the seasonal variations if measured periodically.
- Bathymetric profiles should be performed before and after extreme wave events to determine the closure depth near Bajo Blanco in order to obtain better design criteria for the excavation areas.
- Deeper sediment core samples at Bajo Blanco (at least 3-4 meters deep) should be collected in order to analyze the vertical profile and median grain size distribution and examine whether or not coarser sand particles are present beneath the upper layer of sediments.
- Seismic profiling of Bajo Blanco should be conducted to obtain a realistic estimate of the amount of sand available for dredging at Bajo Blanco. In order to design the dredge areas, the present study assumed that sand was available up to 9 meters beyond the actual seabed, a major assumption which could very well be unrealistic.

- In order to better understand the potential long-term effects of the dredge areas on large-scale coastal processes, a shoreline change model could be used to predict whether the dredge areas would lead to major shoreline perturbations which could interrupt the natural littoral drift of the region.
- Numerical simulations of periods no less than a year should be conducted to evaluate the long-term seasonal response of the wave climate to sand mining the Bajo Blanco sand shoal.
- Finally, further dredging configurations should be evaluated in order to minimize the effects of the dredge area on the nearshore wave climate and sediment transport patterns. One alternative would be to consider a reduction in the berm width in the beach nourishment design, which would significantly reduce the necessary dredge volume. Optimization of the dredging configuration using further numerical simulations is also recommended, with an elongated dredge area seaward of the shoal crest and parallel to the shelf edge being a particularly attractive option.

Many beaches around Puerto Rico are suffering from coastal erosion due to many factors including poorly designed coastal structures, interruption in land-based sediment supply, and sea level rise. Among the coastal protection measures available today, the technique of beach nourishment is considered to be the preferred strategy for shore protection. The methodology applied in this study may be implemented at other eroded beaches in Puerto Rico to estimate the possible impacts that dredging a nearshore or offshore sediment source could cause to the coastal processes and morphodynamic features of an existing beach.

## REFERENCES

- ArcGIS (2016). "Arcgis TIN to Raster tool". Available on the web at <https://pro.arcgis.com/es/pro-app/tool-reference/3d-analyst/tin-to-raster.htm> (accessed 7 June 2016).
- Barber, D. (2015). "Beach nourishment basics". Available on the web at <http://www.brynmawr.edu/geology/geomorph/beachnourishmentinfo.html/> (accessed 5 May 2016).
- Bavaro, M. (2012). "Yuan10 One Talent GNSS". Available on the web at <http://www.onetalent-gnss.com/ideas/usb-hw-receivers/yuan10/> (accessed 5 May 2016).
- Benoit, M., Frigaard, P., and Schaffer, H. A. (1997). "Analysing multidirectional wave spectra: A tentative classification of available methods". In *Proceedings of the 27th IAHR Congress*, San Francisco, CA.
- Bodge, K. R. (2006). "Alternative computation of Dean's overfill factor". *Journal of Waterway, Port, Coastal and Ocean Engineering*, 132:133–138.
- Carmenen, B. and Larson, M. (2007). "A unified sediment transport formulation for coastal inlet application". Technical report, Coastal and Hydraulics Laboratory Technical report, Vicksburg, MS.
- CDIP (2016). "Coastal Data Information Program historical data". Available on the web at <http://cdip.ucsd.edu/> (accessed 5 May 2016).
- Chardón, P. (2013). "Field observations and numerical simulations of storm-induced nearshore morphology change in Rincón, Puerto Rico". Master's thesis, University of Puerto Rico at Mayaguez, Mayaguez, PR.
- Chardón, P. and Canals, M. F. (2012). "Jetski-based bathymetric surveying in Rincón, Puerto Rico". In *OCEANS Science Meeting*, Salt Lake City, UT.
- Conathan, M., Buchanan, J., and Polefka, S. (2014). "The economic case for restoring coastal ecosystem". Technical report, Center for America Progress, Washington DC. Available on the web at <https://www.americanprogress.org/wp-content/uploads/2014/04/CoastalRestoration-report.pdf> (accessed 5 May 2016).
- Davis, M., MacDonald, N. J., Demirbilek, Z., Smith, S., Zundel, Z., and Jones, R. (2005). "Particle Tracking Model (PTM) II: Overview of features and capabilities". Technical report, US Army Engineer Research and Development Center, Vicksburg, MS.
- Dean, R. (1991). "Equilibrium beach profiles: Characteristics and applications". *Journal of Coastal Research*, 7:53–84.

- Dean, R. G. (1974). "Compatibility of borrow material texture for beach fill". In *14th International Conference on Coastal Engineering, ASCE*, pages 1319–1333, Copenhagen, Denmark.
- Dean, R. G. and Dalrymple, R. A. (2004). "Coastal processes and engineering applications". *Press Syndicate of the University of Cambridge*, pages 88–120.
- Earle, M. D. (1996). "Nondirectional and directional wave data analysis procedure". Technical document, National Data Buoy Center, Slidell, LA. Available on the web at <http://www.ndbc.noaa.gov/wavemeas.pdf/> (accessed 5 May 2016).
- Hammer, R., Byrnes, M., Snyder, D., Thibaut, T., and Baker, J. (2004). "Environmental surveys of potential borrow site areas on the central east Florida shelf and the environmental implications of sand removal for coastal and beach restoration". Technical report, Continental Shelf Associates, Inc., Herndon, VA.
- Huyke, R. (2010). "Manual de Laboratorio de Materiales de Ingeniería Civil". *University of Puerto Rico at Mayaguez*.
- Hwang, P. (2012). "Wind sea and swell separation of 1D wave spectrum by spectrum integration method". *Journal of Atmospheric and Oceanic Technology*, 29:277–293.
- IHO (2009). "IHO standards for hydrographic surveys". *International Hydrographic Organization*.
- IHO (2015). "Depth determination". *International Hydrographic Organization*, pages 119–197.
- Inman, D. (1965). "The beach: A river of sand". *AGI-EBF Earth Science Series*.
- Jack, E. (2010). "North Carolina: A digital history". *LEARN North Carolina Website*. Available on the web at <http://www.learnnc.org/lp/editions/nchist-recent/6374> (accessed 5 May 2016).
- Kelley, S. W., Ramsey, J. S., and Byrnes, M. R. (2001). "Numerical modeling evaluation of the cumulative physical effects of the offshore sand dredging for beach nourishment". Technical report, Minerals Management Service and International Activities and Marine Minerals Division (INTERMAR), Herndon, VA.
- Lackey, T. C. (2007). "The Particle Tracking Model description and processes". In *World Dredging Congress*, Lake Buena Vista, FL.
- Lin, L. and Demirbilek, Z. (2012). "Modeling combined diffraction-refraction in a Coastal Spectral Wave Model". In *Proceedings of the Twenty-second International Offshore and Polar Engineering Conference*, Rhodes, Greece.
- Lin, P. (2008). "Numerical modeling of water waves". *Taylor and Francis*, pages 260–263.
- Longuet-Higgins, M. S., Cartwright, D., and Smith, N. (1963). "Observations of the directional spectrum of sea waves using the motions of a floating buoy". *Ocean Wave Spectra*, pages 111–132.

- Lowrance (2012). "HDS Gen2 Touch Operator manual". Available on the web at [http://www.lowrance.com/Root/Lowrance-Documents/US/HDS GEN2 TOUCH COMBO OM EN 988-10312-001 w.pdf](http://www.lowrance.com/Root/Lowrance-Documents/US/HDS_GEN2_TOUCH_COMBO_OM_EN_988-10312-001_w.pdf) (accessed 5 May 2016).
- MacDonald, N. J. (2006). "PTM: Particle Tracking Model, model theory, implementation and example applications report". Technical report, Coastal Inlets Research Program, Dredging Operations and Environmental Research Program, Vicksburg, MS.
- Mackenzie, K. (1981). "Nine-term equation for the sound speed in the oceans". *The Journal of the Acoustical Society of America*, 103:807–812.
- MacMahan, J. (2001). "Hydrographic surveying from personal watercraft". *Journal of Surveying Engineering*, 127:12–24.
- Mitsuyasu, H., Tasai, F., Suhara, T., Mizuno, S., Ohkusu, M., Honda, T., and Rikiishi, K. (1975). "Observations of the directional spectrum of ocean waves using a cloverleaf buoy". *Journal of Physical Oceanography*, 5:750–760.
- NAD (1983). "North American Datum". Available on the web at <https://confluence.qps.nl/pages/viewpage.action?pageId=29855153> (accessed 7 June 2016).
- NDBC (2016). "National Data Buoy Center". Available on the web at <http://www.ndbc.noaa.gov/> (accessed 5 May 2016).
- NGDC (2016). "National Geophysical Data Center". Available on the web at <https://www.ngdc.noaa.gov/> (accessed 7 June 2016).
- NGS (2016). "National Geodetic Survey". Available on the web at <https://www.ngs.noaa.gov/> (accessed 7 June 2016).
- NOAA (2009). "Coral reef habitat assessment for U.S. Marine protected areas: Commonwealth of Puerto Rico". Technical report, NOAA's National Ocean Service, Management and Budget Office, Silver Springs, MD. Available on the web at [http://www.coris.noaa.gov/activities/habitat assessment/puerto rico.pdf](http://www.coris.noaa.gov/activities/habitat_assessment/puerto_rico.pdf) (accessed 5 May 2016).
- Padman, L. (2005). "Tide Model Driver (TMD) Manual". *Earth and Space Research*.
- Salas, F. C. (2014). "Analysing equilibrium beach profile to determine sedimentary budget for the nourishment of a rapidly eroding beach at Rincón, Puerto Rico, u.s.". Master's thesis, Plymouth University.
- Sánchez, A., Beck, T., Lin, L., Demirbilek, Z., Brown, M., and Li, H. (2012). "Coastal Modeling System draft user manual". *U.S. Army Engineer Research and Development Center, Coastal and Hydraulics Laboratory*.
- SeaFloorSystems (2015). "Sonarmite/Sonarm8 user manual". *Seafloor Systems, Incorporated*.

- Smith, J. M. and Smith, J. (2002). "Grid nesting with STWAVE". Technical report, Coastal and Hydraulics Laboratory Technical report, Vicksburg, MS.
- Stanica, A. and Ungureanu, V. G. (2010). "Understanding coastal morphology and sedimentology". *NEAR Curriculum in Natural Environmental Science.*, 88:105–111.
- Storlazzi, C. D., Norris, B. K., and Rosenberger, K. J. (2015). "The influence of grain size, grain color, and suspended-sediment concentration on light attenuation: Why fine-grained terrestrial sediment is bad for coral reef ecosystems". *Coral Reefs*, 34:967–975.
- Takasu, T. (2015). "RTKLIB: An open source program package for GNSS positioning". Available on the web at <http://www.rtklib.com/> (accessed 5 May 2016).
- Thieler, R. E., Rodríguez, R. W., and Himmelstoss, E. A. (2007). "Historical shoreline changes at Rincón, Puerto Rico, 1936-2006". Technical report, U.S. Geological Survey and U.S. Department of the Interior., VA.
- Trembanis, A. C. and Pilkey, O. H. (1998). "Summary of beach nourishment along the U.S. Gulf of Mexico shoreline". *Journal of Coastal Research.*, 14:407–417.
- Wentworth, C. K. (1922). "A scale of grade and class terms for clastic sediments". *Journal of Geology*, 5:377–392.
- WGS (1984). "World Geodetic System". Available on the web at <https://www1.nga.mil/ProductsServices/GeodesyandGeophysics/WorldGeodeticSystem> (accessed 7 June 2016).
- Zheng, L., Weisberg, R. H., Huang, Y., Luettich, R. A., and Westerink, J. J. (2013). "Implications from the comparison between two- and -three dimensional model simulations of the Hurricane Ike storm surge". *Journal of Geophysical Research.*, 118:3350–3369.

# Appendices

## **Appendix A**

### **Sieve results**

This appendix includes the sieve analysis results from the 8 samples collected at the coast of Rincón and the 18 samples from the Bajo Blanco shoal. Samples from the coast of Rincón were captured at approximately 600 meter segments starting from Rincón Marina and extending to Córcega beach. Similarly, the samples collected along the Bajo Blanco shoal are spaced by approximately 300 meters starting from the northwest region of the shoal.

**Table A.1:** Latitude and longitude for each of the samples collected at the coast of Rincón.

<b>Coast of Rincón</b>		
<b>Samples</b>	<b>Latitude</b>	<b>Longitude</b>
1	18.344323	-67.259631
2	18.341564	-67.256366
3	18.337414	-67.254023
4	18.333177	-67.253063
5	18.330394	-67.252041
6	18.327897	-67.250751
7	18.322970	-67.248455
8	18.319358	-67.246637

**Table A.2:** Latitude and longitude for each of the samples collected at the Bajo Blanco sand shoal.

<b>Bajo Blanco sand shoal</b>		
<b>Samples</b>	<b>Latitude</b>	<b>Longitude</b>
1	18.344550	-67.263767
2	18.343300	-67.262850
3	18.342267	-67.262050
4	18.341567	-67.262767
5	18.338233	-67.256783
6	18.341100	-67.259933
7	18.340050	-67.260233
8	18.339167	-67.261017
9	18.339700	-67.258650
10	18.338680	-67.258860
11	18.337567	-67.260250
12	18.337283	-67.258833
13	18.338233	-67.256783
14	18.336933	-67.257317
15	18.335583	-67.258450
16	18.337150	-67.255317
17	18.334983	-67.256550
18	18.335300	-67.254670

**Table A.3:** Sieve analysis results for the 8 samples collected at the coast of Rincón, including standard deviation and mean grain size in millimeters and phi units.

Coast of Rincón sieve analysis results								
% Coarser than	Sample #1	Sample #2	Sample #3	Sample #4	Sample #5	Sample #6	Sample #7	Sample #8
5%	-0.12	-0.16	0.76	0.36	0.26	0.46	0.76	0.18
16%	0.32	0.10	1.09	0.93	0.85	1.02	0.98	1.01
50%	1.09	1.08	1.97	1.70	1.35	1.92	1.65	2.04
84%	1.58	2.31	2.58	2.47	2.12	2.57	2.42	2.57
95%	1.74	2.63	3.04	2.72	2.70	3.02	2.68	2.74
Mean Grain-size (phi)	0.99	1.16	1.88	1.70	1.44	1.84	1.68	1.88
Mean Grain-size (mm)	0.502	0.447	0.272	0.308	0.368	0.280	0.311	0.273
Standard Deviation	0.62	1.02	0.76	0.78	0.72	0.81	0.68	0.81

**Table A.4:** Sieve analysis results for the first 9 samples collected at the Bajo Blanco shoal, including standard deviation and mean grain size in millimeters and phi units.

Bajo Blanco shoal sieve analysis results									
% Coarser than	Sample#1	Sample#2	Sample#3	Sample#4	Sample#5	Sample#6	Sample#7	Sample#8	Sample#9
5%	1.06	0.77	0.96	0.97	0.93	-0.11	0.78	0.92	1.01
16%	1.76	1.42	1.56	1.76	1.46	0.22	1.56	1.37	1.61
50%	2.18	2.14	2.18	2.17	2.12	1.76	2.15	2.10	2.16
84%	2.61	2.60	2.65	2.57	2.57	2.49	2.59	2.58	2.59
95%	2.75	2.75	3.21	2.70	2.72	2.72	2.73	2.74	2.74
Mean Grain-size (phi)	2.18	2.05	2.13	2.17	2.05	1.49	2.10	2.02	2.12
Mean Grain-size (mm)	0.220	0.241	0.229	0.223	0.241	0.356	0.233	0.247	0.230
Std. Dev.	0.49	0.62	0.65	0.49	0.58	1.04	0.58	0.61	0.53

**Table A.5:** Sieve analysis results for the last 9 samples collected at the Bajo Blanco shoal, including standard deviation and mean grain size in millimeters and phi units.

Bajo Blanco shoal sieve analysis results									
% Coarser than	Sample#10	Sample#11	Sample#12	Sample#13	Sample#14	Sample#15	Sample#16	Sample#17	Sample#18
5%	0.95	1.11	1.06	1.02	0.97	0.91	1.01	0.93	1.07
16%	1.42	1.79	1.81	1.75	1.53	1.33	1.65	1.59	1.77
50%	2.14	2.20	2.17	2.16	2.14	2.08	2.16	2.16	2.22
84%	2.64	2.62	2.59	2.57	2.57	2.57	2.59	2.60	2.66
95%	3.18	2.91	2.72	2.71	2.72	2.73	2.72	2.74	3.22
Mean Grain-size (phi)	2.07	2.20	2.19	2.16	2.08	2.00	2.13	2.12	2.22
Mean Grain-size (mm)	0.239	0.217	0.219	0.223	0.236	0.251	0.228	0.231	0.215
Standard Deviation	0.68	0.51	0.47	0.49	0.55	0.62	0.52	0.55	0.58